Diagnostics and Modeling of Polymer Electrolyte Membrane Water Electrolysers

Ishanka Udeshini Dedigama

A thesis for the degree of Doctor of Philosophy of the University College London

Department of Chemical Engineering
University College London (UCL)
Torrington Place London, WC1E 7JE, United Kingdom

I, Ishanka Dedigama confirm that the work presented in this thesis is my own. Where information has been derived from other sources, I confirm that this has been indicated in the thesis.

_____

Signature

_____

Date

I. Acknowledgements

Firstly, I would like to thank Dr. Dan Brett for giving me the opportunity to work on this project. Thank you for your guidance and your unstinted support throughout the years. Your knowledge and enthusiasm of the subject motivated me immensely and your pleasant personality made working with you more enjoyable. You are the best supervisor anyone could ever ask for.

I would like to thank my second supervisor, Prof. Asterios Gavriilidis for his feedback and checking my progress on the student log. I would also like to thank Dr. Paul Shearing for his valuable input to this project and for his help in setting up the Electrochemical Innovation Lab (EIL). A thank you to Prof. Anthony Kucernak from Imperial College for his valuable guidance during the initial stage of this project.

I would like to thank Dr. Kathy Ayers from Proton Onsite, USA for providing me with the MEAs and cell components and most importantly for her valuable technical input. Thank you for having me at Proton Onsite and giving me the opportunity to see large scale electrolysers in operation and the commercial side of the technology. A big thank you to Dr. Nick Van Dijk form ITM power, UK for his input and constructive suggestions.

A big thank you to Adrian from the EPSRC loan pool for all the help he has given me with the high-speed cameras. Thank you Chris, from Amalyst, for helping me with catalyst synthesis work. I would also like to thank Simon, Mike, Brian, Martyn, Dave and James for helping me out with electrical and IT related problems. A big thank you to Anna Harrington and Patty for helping me with all the admin work. A thank you to Mae and Agatha for constantly helping me with orders and room bookings.

A massive thank you to everyone from the EIL for everything they have done. Thank you Mithila, Flora and Amal for being lovely friends and helping me get

through this. Thank you Tom, Toby and Jay for all the help you have given me with lab work and specially keeping me out of trouble during the first few years. Thank you Rhod, Phil, Quentin, Mayowa, Dave, Rashed, Aliya, Leon, Valentina, Dimitri, Rema, Krisztian and the newbies for their help during the project and making the office a nice place to work in.

A special thank you to my mom, dad and my brother. Thank you Ammi for your unconditional love and everything you have done for me. You are my strength and the voice in my head pushing me to do better. Thank you for always being there without fail and giving me strength and confidence to achieve my goals. You are the best mother ever and I couldn't have done it without you. Thank you Thathi for always putting a smile on my face and making me feel like a princess. Thank you Malli for being my 'big brother' (although you are younger to me) and taking care of me.

Finally I would like to thank my cousin B Aiya and my close friend outside work, Nilushi for keeping me sane. Thanks for being understanding during very busy times and for keeping me entertained with all the drama in your life.

II. Abstract

Proton exchange membrane water electrolyser (PEMWE) technology can be used to produce hydrogen from renewable energy sources; the technology is therefore a promising component in future national power and transportation fuel systems. The main challenges faced by the technology include prohibitive materials costs, maximising efficiency and ensuring suitable longevity. Therefore, research is needed to understand the internal operation of the systems so that cell design can be optimised to obtain maximum performance and longevity.

PEMWE is a low temperature electrolysis system that consists of cell components such as end plates, current collectors, bipolar plates, gas diffusion layers (GDLs) and membrane electrode assemblies (MEAs). Cell performance is strongly reliant on the materials and designs of each of the components.

Three cell designs were used to study different aspects of PEMWE operation: commercial cell, optically transparent cell and combined optical and current mapping cell. Polarisation measurements performed on a commercially available lab-scale test cell at ambient conditions illustrated an increase in mass transport limitations with increasing water flow rate which was confirmed using electrochemical impedance spectroscopy (EIS) measurements. A transparent cell was constructed to allow optical access to the flow channels. Measurements made on the cell showed a transition from bubbly to slug flow that affects mass transport limitations and consequently the electrochemical performance. Thermal imaging measurements supported a mass and energy balance of the system.

Finally, a combined transparent and current mapping cell was constructed using PCB technology that indicated higher current densities closer to the exit of the channel. Optical measurements showed that this increase in current was associated with larger bubbles and a transition to slug flow which led to enhanced mass transport of water to the electrode surface.

A model developed for the system showed that the cell potential is dominated by the anode activation overpotential. Experimental data obtained at similar conditions with the commercially available lab-scale test cell agreed well with the model and the fitted parameters were in close proximity with values published in literature.

III. Publications

Primary journal articles

I. Dedigama, P. Angeli, K. Ayers, J. B. Robinson, P. R. Shearing, D. Tsaoulidis, and D. J. L. Brett, In situ Diagnostic Techniques for Characterisation of Polymer Electrolyte Membrane Water Electrolysers – Flow Visualization and Electrochemical Impedance Spectroscopy, International Journal of Hydrogen Energy, 39 (2014) 4468-4482

I. Dediagama, T. J. Mason, J. Millichamp, K. Ayers, P. R. Shearing and D. J. L Brett, An electrochemical Impedance Spectroscopy study of a Polymer Electrolyte Membrane Water Electrolyser, Journal of The Electrochemical Society, (Submitted)

I. Dedigama, D. Tsaoulidis, J. Millichamp, N. V. Dijk, P. R. Shearing and D. J. L. Brett, Current Density Mapping and Optical Flow Visualisation of a Polymer Electrolyte Membrane Water Electrolyser, Journal of Power Sources, (Accepted)

I. Dedigama, K. Ayers, P.R. Shearing and D. J. L. Brett, An Experimentally Validated Steady State Polymer Electrolyte Membrane Water Electrolyser Model, International Journal of Electrochemical Science, 9 (2014) 2662-2681

IV. Contents

V. List of Figures

VI. List of Tables

1. Introduction

A range of renewable energy technologies are being developed that offer possible solutions for the global energy shortage and environmental problems caused by the use of fossil fuels. Renewable energy can be stored in the form of hydrogen, which can be converted into useful forms of energy more efficiently, sustainably and securely [1] than fossil fuels. In many ways, hydrogen is the ideal energy carrier as it is recyclable and perceived as a clean fuel since it produces almost no pollution when used in its pure form [2]. Most importantly, hydrogen together with fuel cells play an important role in delivering a 'hydrogen economy' [3] which promises to decrease the dependence on fossil fuels, reducing carbon emissions, and enabling clean, reliable power generation.

As shown in Figure 1, production of hydrogen can be achieved in many ways [4], but is dominated by reforming and gasification of fossil fuels; natural gas 50%, heavy oil 30% and coal 20% [5]. Thermal processes in hydrogen production convert hydrogen containing resources such as natural gas, coal or biomass into a hydrogen rich stream [6]. Electrolytic processes split water into hydrogen and oxygen using an electrical current, whereas photolytic processes use energy in sunlight to decompose water.

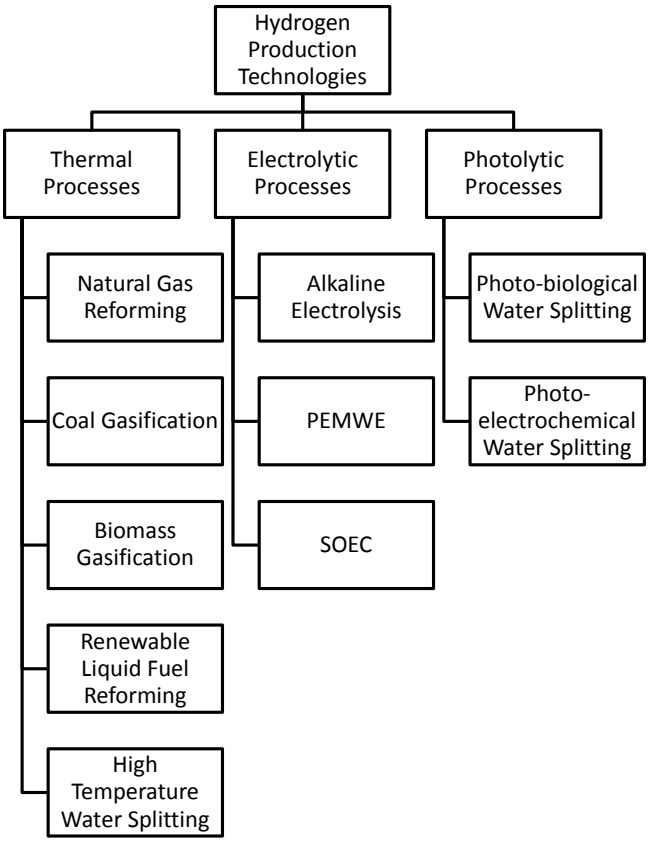

Figure 1: Hydrogen production methods currently being used.

The most abundant source of hydrogen is water, and water electrolysis is the simplest way of splitting water to obtain hydrogen [7]. Electrolysed hydrogen stands out from hydrogen produced from hydrocarbons, as it has the capability of providing excellent product purity and its possibility to produce hydrogen on site and on demand, avoiding the transportation and storage problems. Although electrolysis technology has been known for nearly 200 years it only represents 4% of the world hydrogen production, as its applications are limited to small scale and unique situations where access to large-scale hydrogen production plants is not possible or economical, such as: marine, rockets, spacecrafts, electronic and food industry, chromatographs, laboratories and medical applications [1, 8]. Commercial electrolysis cells are also used to provide hydrogen for cooling electricity generators.

Water electrolysis plays an important role in the transition to a hydrogen economy as it can be made more sustainable by using renewable electricity. A proposed road map of sustainable energy is illustrated in Figure 2 where excess electricity from renewable energy is converted to hydrogen by electrolysis that can be used in electric vehicles and for household applications [9].

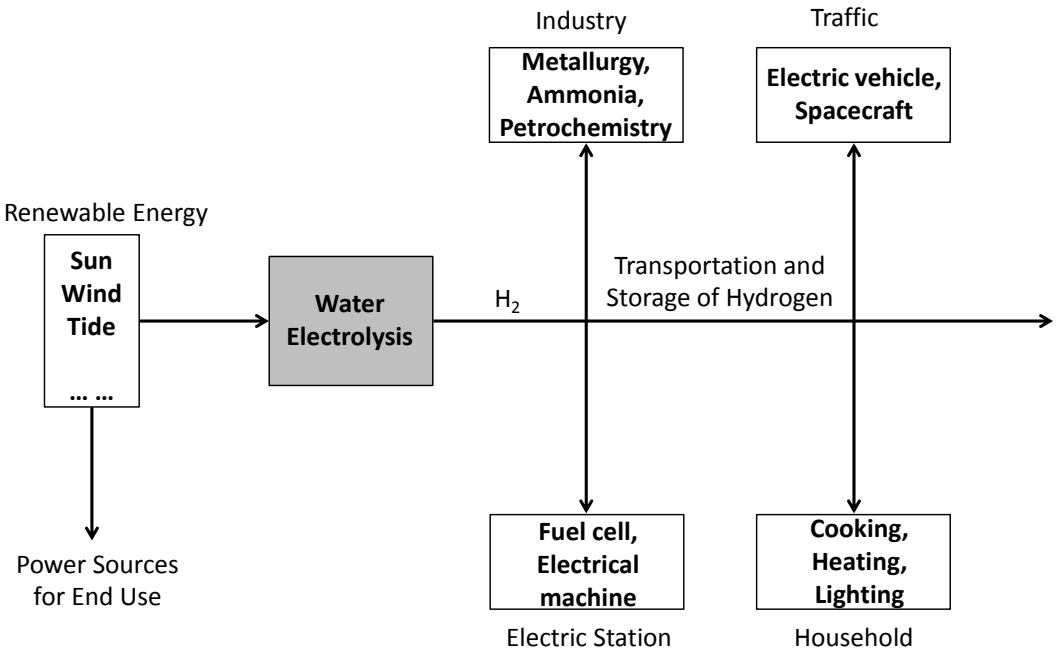

Figure 2: Sustainable production and application of energy [9].

Currently, there are three distinct types of water electrolysis systems. The most common technology is alkaline electrolysis, although proton exchange membrane / polymer electrolyte membrane (PEM) electrolyser and solid oxide electrolysis cells (SOEC) are fast developing.

SOECs consist of a dense ionic conducting electrolyte and two porous electrodes that typically operate at temperatures in the range of 800 °C – 1000 °C. They have relatively high efficiencies, between 70% - 90% [10], as they are capable of producing hydrogen at a higher chemical reaction rate with lower electrical energy requirement [11]. However, the main concerns associated with the SOEC

technology is the chemical and physically stability of the electrode materials in highly oxidising / reducing environments and high cost of electrolytes that are required to withstand high operating temperatures [12]. It also has challenges with corrosion, seals, thermal cycling, and chromium migration [13].

A simple alkaline electrolyser system consists of an anode, a cathode, a gas separator and an aqueous alkaline electrolyte and has efficiencies between 59% - 70% [6]. Typical electrolytes used in an alkaline system are KOH and NaOH of approximately 30 wt% and operate at temperatures around 80 °C - 90 °C. Although this technology has historically been one of the most popular routes for producing hydrogen, it requires further improvement in advanced anode materials to improve the overall electrical efficiency by reducing the electrode polarisation [14].

For several decades PEM electrolyser technology was mainly used to produce oxygen for space and underwater applications. Currently it has renewed interest for the production of hydrogen using renewable energy sources [15, 16]. PEM water electrolysis has been identified in the European Hydrogen and Fuel Cell programme as a key process for transforming zero-carbon electricity sources into the supply of zero-carbon hydrogen and oxygen for miscellaneous uses [17].

Proton exchange membrane water electrolysis (PEMWE) technology is a fast developing technology and has many areas that need to be improved in order to achieve better performance. The main drawback of PEMWEs is the cost of the corrosion resistant titanium components, membrane and the precious metal electrocatalysts, which adds up to about 90% of the total capital cost [8]. PEM electrolysis can be made more attractive if production costs can be reduced by improving the performance and the durability of the technology. The key to gaining a better understanding of the operation of the technology is the use of bespoke diagnostic techniques to examine the physical, chemical and electrochemical processes occurring during operation.

This thesis presents an insight to working principles and commonly used materials for the construction of PEMWEs and identifies current drawbacks of the technology. It presents diagnostic techniques that allow much needed *in situ* measurements of the system to gain a better understanding of its performance in order to address technological challenges. These diagnostic techniques include: electrochemical impedance spectroscopy (EIS), current density mapping, thermal imaging and direct optical visualisation. Three cell configurations are used in this study: a commercial lab-scale cell, transparent cell and a transparent segmented cell. The transparent cells are designed and developed to incorporate printed circuit board (PCB) technology. The main parameter of interest in this study is the feed water flow rate. Therefore, results obtained at different flow rates are analysed and compared with data present in literature to understand the effect of bubble formation and two-phase flow patterns on the performance of the electrolyser. Furthermore, a mathematical model is developed to describe the overpotentials associated with PEM electrolysis and to determine the most sensitive parameters to its performance.

2. Literature Review

2.1. PEMWE Technology

The first PEMWE was developed by General Electric in the 1960s based on the solid polymer electrolyte (SPE) concept and was mainly used to produce oxygen in anaerobic environments [15]. Recently, PEMWE technology is being considered as a promising alternative to alkaline electrolysis for the large scale production of hydrogen.

PEMWE technology has many advantages over the traditional alkaline electrolysis systems. They are capable of achieving high current densities (> 2 A cm^{-2}) due to higher active surface areas, reducing capital costs and potentially the overall cost of operation. The PEM has a low gas crossover rate, yielding hydrogen with high purity (up to 99.999%) [18]. PEMWE systems provide a low ohmic drop across the membrane due to the minimisation of inter-electrode spacing, greater safety as there is no caustic electrolyte circulated in the system, greater reliability as less difficulties are encountered due to corrosion and a simplified and more compact design [19-23]. Furthermore, they are able to operate under high pressures (typically 30 - 165 bar) [24] and the good load-following properties are advantageous in renewable energy applications. Table 1 summarises the difference in specifications of the alkaline and PEM electrolyser systems [25].

Table 1: state of the art for the specifications of alkaline and PEM electrolysers as reported in the NOW study [25].

Specifications	Alkaline electrolysis	PEM electrolysis
Cell Temperature (°C)	60-80	50-80
Cell pressure (bar)	<30	<30
Current density (A cm^{-2})	0.2-0.4	0.6-2.0
Cell voltage (V)	1.8-2.4	1.8-2.2
Power density (mW cm^{-2})	<1	<4.4
Voltage efficiency HHV (%)	62-82	67-82
Specific energy consumption: stack (kW h Nm^{-3})	4.2-5.9	4.2-5.6
Specific energy consumption: system (kW h Nm^{-3})	4.5-7.0	4.5-7.5
Lower partial load range (%)	20-40	0-10
Cell area (m^2)	>4	<0.03
H_2 production rate: stack-system (Nm^3 h^{-1})	<760	<10
Lifetime stack (h)	<90 000	<20 000
Lifetime system (y)	20-30	10-20
Degradation rate (μV h^{-1})	<3	<14

Giner, Inc. (USA) and Proton OnSite (USA) are the two major PEMWE commercial developers in the USA. They are capable of achieving system efficiencies close to 70% (LHV), which although impressive, is lower than the Department of Energy (DoE) target of 74% [26, 27]. The cost of hydrogen produced by commercially available PEMWE systems at present is estimated to be \$4.8/kg-H_2 and is considerably higher than the targets set by the DoE [28]. ITM Power (UK) is the largest commercial developer of hydrogen energy systems in the UK. They are currently involved in the UKH2Mobility program, which promotes hydrogen powered travel in the UK.

Small scale PEMWE systems include the HPac range that can produce hydrogen at a purity of 99.99 %. The HGas product brings together rapid response and self-pressuring PEM electrolysis to a fully integrated package, which is capable of addressing MW scale applications. HFuel is a self-contained module for refuelling hydrogen powered road vehicles and forklift trucks. However, the main drawback of this technology is its prohibitively high cost, of which about 90% is materials cost.

Table 2 shows the specifications for HOGEN® RE by Proton Onsite that has been developed for use in conjunction with renewable energy sources [7].

Table 2: Specifications of HOGEN® RE PEM electrolyser by Proton Onsite [7].

Parameter	Value
Hydrogen output	0.5 or 1.0 $Nm^3 h^{-1}$
Maximum delivery pressure	200 bar
Hydrogen purity	>99.9%
Water usage	0.5 or 1.0 $l h^{-1}$
Minimum water quality required	Deionised (ASTM Type II)
Power consumption	6.6 kWh $N^{-1}m^{-3}$
Electrical supply required	AC: 190-240 VAC, 1 phase, 50/60 Hz, 7.2 or 12 kVA DC: 60-200 VDC, 150 A (max)
Operating environment	Indoor
Dimensions	97 x 105 x 106 cm
Weight	220 kg

2.1.1. Principle of Operation

A PEMWE converts electrical energy to chemical energy. This is achieved by applying a direct current (DC) voltage across a PEM electrolysis cell made up of an anode, cathode, proton exchange membrane (typ. Nafion), bipolar plates and end

plates that hold the cell together. In such a system, water is introduced at the anode where it is oxidised to oxygen, with the production of hydrogen ions and electrons, as shown in Equation (1). Hydrated hydrogen ions ($H^+.xH_2O$) migrate to the cathode through the membrane where they recombine electrochemically with electrons to produce hydrogen (Equation (2)); the overall reaction corresponds to Equation (3) [6-8, 29]. Figure 3 shows the working principle and the schematic view of a PEMWE.

Anode: $2H_2O \rightarrow O_2 + 4H^+ + 4e^-$ (1)

Cathode: $4H^+ + 4e^- \rightarrow 2H_2$ (2)

Overall: $H_2O \rightarrow H_2 + {}^1/_2\, O_2$ (3)

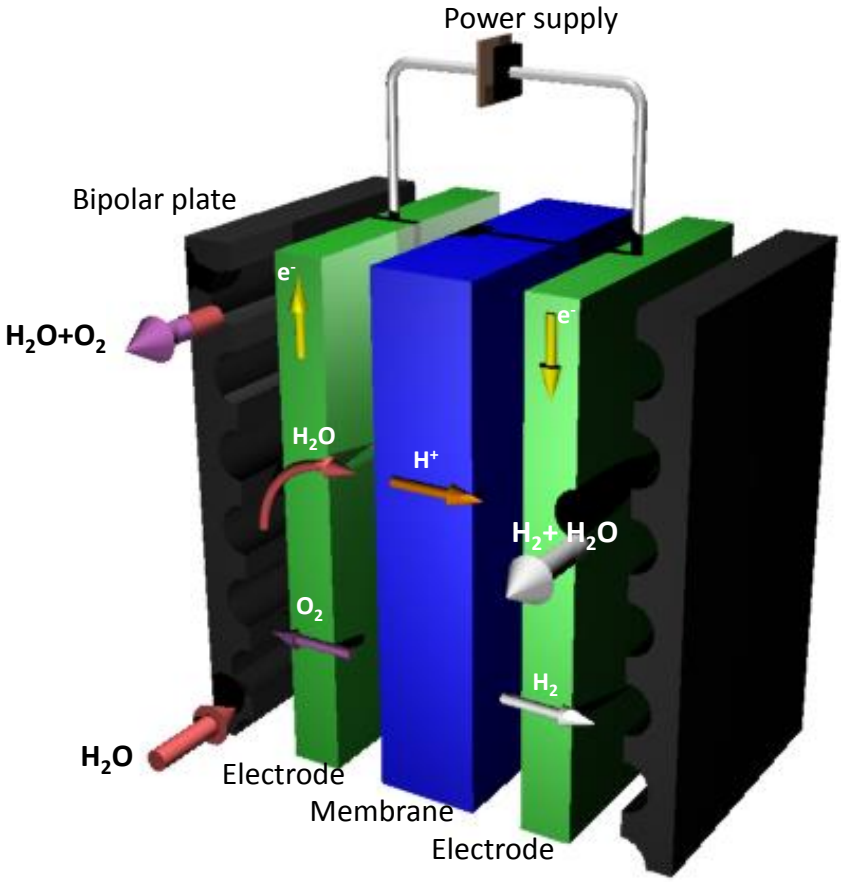

Figure 3: Working principle and the schematic of a PEMWE.

2.1.2. Materials of Construction

A PEM electrolyser cell is similar in construction to a PEM fuel cell (PEMFC). It consists of a membrane electrode assembly (MEA), which is composed of an anode, cathode and an electrolyte, electrode flow-field plates, electrode conductors and end plates that hold the cell together, as illustrated in Figure 3. However, the materials used are typically different from a PEMFC, as carbon materials cannot be used on the oxygen generation electrode due to corrosion caused by the high voltages.

2.1.2.1. Membrane Electrode Assembly (MEA)

Membrane

Membrane materials must exhibit high ionic conductivity while preventing electron transport and crossover of hydrogen and oxygen. They must also be chemically and thermally stable throughout the operating temperatures and mechanically robust [20, 30, 31].

Typically, a perfluorocarbon sulphonate cation exchange membrane is used, for example Nafion of 50 - 250 µm [8, 29, 32, 33]. However, other types of membranes have been used, including: sulfonated polyether ether ketone (SPEEK) with polyether sulfone (PES) [34], polysulfone (PSF) [35] and with heteropolyacids (HPAs) [36]. Furthermore, Hyflon membranes have been used in place of Nafion at higher operating temperatures (120 - 150 °C) [33].

Electrocatalysts

The electrocatalyst layer is where the hydrogen evolution reaction (HER) or oxygen evolution reaction (OER) takes place. The electrocatalyst is bonded to the electrolyte and should have an optimised structure and porosity to decrease the mass transfer resistance [37]. The hydrated membrane has an acidity equivalent to 10 wt% H_2SO_4; therefore, materials with high corrosion resistance should be used to form the electrocatalyst layers.

Much attention is given to the anode electrolcatalyst as the OER governs the efficiency of a PEMWE due to the greater amount of overpotential losses related to the anode electrochemical processes when compared to the cathode [38]. The acidic environment and the high anodic overpotential created during water electrolysis make it impractical to use non-noble metals like Ni and Co as the anode electrocatalyst layer due to corrosion [39]. Based on these requirements, iridium oxide (IrO_2), ruthenium oxide (RuO_2) or a mixture of the two oxides and platinum iridium (PtIr) are commonly used as the anode electrocatalyst [40-42]. Investigations on oxides of other transition metals such as Ti [43], Ta [44-47] and Nb [48] have been carried out. Typically, platinum / palladium black, carbon supported platinum or palladium nanoparticles are used on the cathode side because of their high catalytic activity for the HER [49, 50].

Efforts are being made to reduce the catalyst loading from 4 mg cm^{-2} to 0.18 mg cm^{-2} on the anode [8]. At the cathode, efforts are being made to reduce the platinum loadings down to 0.02 mg cm^{-2} [8]. In parallel, studies have been carried out to obtain platinum-free carbon supported catalysts and positive results have been obtained for cobalt clathrochelates [51, 52] and polyoxometalates [18] in place of platinum for the HER. Figure 4 illustrates a summary of the performance of variety of electrolcatalysts for the OER and the HER based on studies done by Miles and Thomason [53].

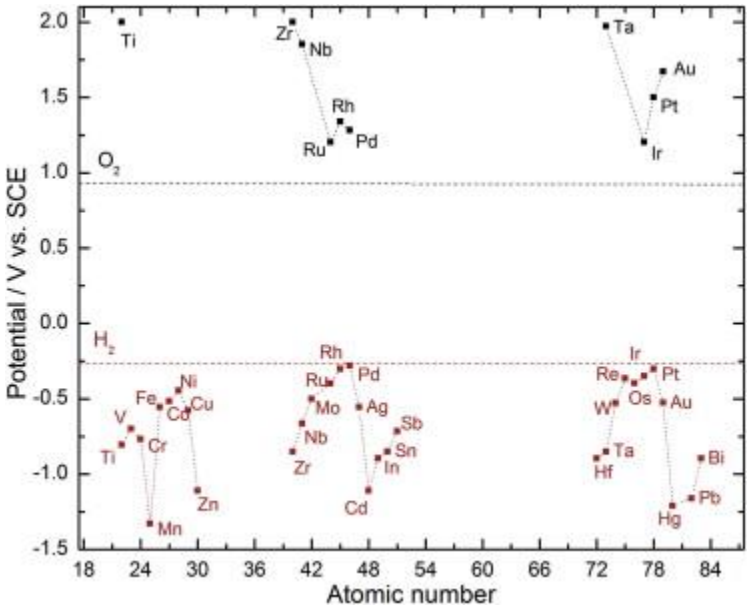

Figure 4: Summary of cyclic voltammetric results for a number of metallic elements in 0.1 mol L^{-1} H_2SO_4 at 80 °C. The potential vs. SCE is shown where the current density attains 2 mA cm^{-2} using a potential sweep rate of 50 mV s^{-1}[53].

2.1.2.2. Gas Diffusion Layer (GDL)

The catalyst coated membrane (CCM) is sandwiched between two diffusion layers. The diffusion layer, which is a combination of a gas diffusion layer (GDL) and a micro porous layer (MPL), plays multiple roles: (1) maintains an electronic connection between the bipolar plate with channel-land structure and the electrode; (2) acts as a passage for reactant transport and heat / water removal; (3) provides mechanical support to the MEA, and (4) protects the catalyst layer from corrosion or erosion by flows or other factors [30]. Therefore, GDL materials should have a good porosity, typically in a range of 30% - 50% [54], low electrical and contact resistance and resistant to corrosion. Commonly, Toray carbon fiber paper is used as the diffusion layer for the cathode side [37] and on the anode side, microporous metal sheets of titanium, zirconium, hafnium, niobium and tantalum have been used [55].

2.1.2.3. Bipolar Plates

Bipolar plates in PEM electrolysers contain flow channels within them and act as [8]:

- A conductor, transferring electrons from the oxygen electrode of one cell to the hydrogen electrode of the adjacent.
- A distributor of reactant water for reactions and remove products.
- A separator of hydrogen and oxygen gasses evolved in the cathode and anode chambers respectively.
- A mechanical supporting plate of the membrane for different operating pressures.

In addition, cooling channels can also be machined within the bipolar plates for waste heat removal [30]. Therefore, the criteria of a reliable and an economical current collector material include: high electric conductivity, low contact resistance with the diffusion layers on the anode and cathode sides, sufficient corrosion resistance under operating conditions, impermeable to hydrogen and oxygen, low fabrication costs and a prolonged lifetime.

Nb and Ti with Pd, coated with a thin layer of Pt exhibits contact resistances as low as that of gold and thus are used as anode current collectors. However, a small percentage of hydrogen produced at the cathode chamber may diffuse into the crystal lattice of the collector material and reduce its ductility. Hence, materials that have a higher resistance to hydrogen embrittlement should be used as the cathode current collector. According to Lu *et al.*[8], graphite has the highest resistance to embrittlement compared to Zr, Nb, Ti and Ta.

2.1.2.4. Printed Circuit Board (PCB) Technology

PCB technology has been shown to be an effective way to make PEMFCs [56, 57] and perform current mapping [58-61]. The approach has the advantages of fast prototype cycle times, low cost prototyping, high design flexibility, complex conductor / insulator patterning, low temperature processing capability, utilises low weight composite material and it is a mature, robust, reliable technology [62]. However, despite the great advantages, to date the technique has not been applied to PEMWEs.

2.1.3. Operating Conditions

2.1.3.1. Voltage

The most vital parameter of an electrolysis system is its operating voltage as it determines the electricity efficiency and therefore the energy consumption. A higher voltage, for a given current density, to produce equivalent hydrogen means lower efficiency. Its value is dependent on other operating conditions such as temperature and pressure and materials used for the construction of the cell. As shown in Table 1, the typical operating voltage of an electrolysis cell is 1.8 V - 2.2 V [25].

2.1.3.2. Current Density

Current density has an inverse relation to the energy efficiency of a system. However, higher operating current density results in greater electrochemical reaction rate giving a higher hydrogen production rate. Increased gas production

will cause rapid bubble formation resulting in increased mass transport limitations. Therefore, the operating current density should be maintained within a certain range with compromises between gas production rate and energy efficiencies [2, 18]. PEM electrolysers can operate at current densities close to 2 A cm^{-2} (Table 1).

2.1.3.3. Temperature

Operating temperature has a significant impact on the performance of the electrolysis cell. At higher temperatures the thermodynamic electrical energy requirement to drive the reaction is less which results in lower operating potential [63]. The general operating temperature of PEM electrolysis cell is 30 °C - 80 °C as the perfluorinated ionomers usually used in the MEA is thermally unstable at higher temperatures [64, 65].

Figure 5 shows polarisation measurements obtained at different temperatures by Ma *et al*. [65] which shows that higher operating temperatures reduce the operating voltage of the cell as reaction kinetics are favoured by the high temperatures.

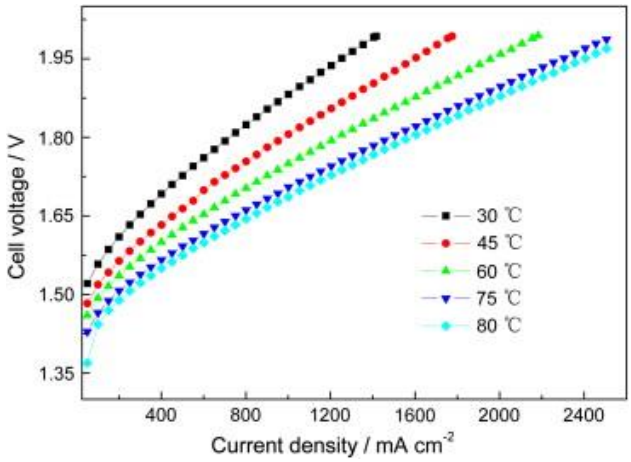

Figure 5: The effect of cell temperature on PEM electrolyser performance [65].

2.1.3.4. Pressure

The operating pressure of the system could be higher than the atmospheric pressure depending on the end use of hydrogen [2]. Increase in pressure reduces the volume of gas bubbles generated during electrolysis, which in return improves the water transport and the electrical contact between catalytic layer and the current collector, while reducing ohmic losses in the catalytic layer. Furthermore, it allows hydrogen to be delivered at a high pressure for the end users that provides the advantage of requiring less energy to further compress and store hydrogen [2, 21, 25]. On the other hand, problems associated with high operating pressures come from cross permeation phenomena that increase with pressure, leading to operating hazards [66]. Figure 6 shows the influence of operating pressure on the performance of an electrolysis cell and it can be seen that higher pressures increase the operating voltage of the cell [67].

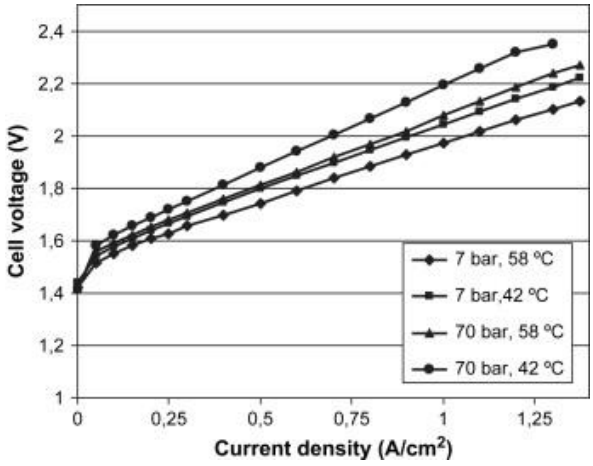

Figure 6: Electrolyser polarisation curve at different operating conditions [67].

2.1.3.5. Water Distribution

Water distribution on anodic and cathodic sides can be achieved by forced circulation of deionised (DI) water. Water is circulated through the channels for reaction feeding, heat removal and gas transport to the gas - water separation unit [22]. The purity of water is vital for decent operation of the water electrolyser as impurities could deposit on the electrode surface hindering the ion transfer and electrochemical reactions.

The Nafion membrane conducts protons from the anode to the cathode. This solid state conduction of the protons is accompanied by multiple water molecules $(H_2O)_nH^+$ [29]. Therefore, an extra amount of water is transferred to the cathodic side during electrolysis by electro-osmosis (approximately 3.5 water molecules per proton) and it can be balanced by applying a small differential pressure between the two compartments [22]. The membrane must be kept hydrated during electrolysis and at rest to sustain the conduction mechanism [22, 29]. Hence, water recycling is an important consideration since water is continuously removed from the anode and transported to the cathode [29]. Studies have shown that

increase in water flow rate reduces the PEMWE efficiency at low current densities [68] and has a significant effect on the operating voltage of the cell at higher current densities, as shown in Figure 7 [69].

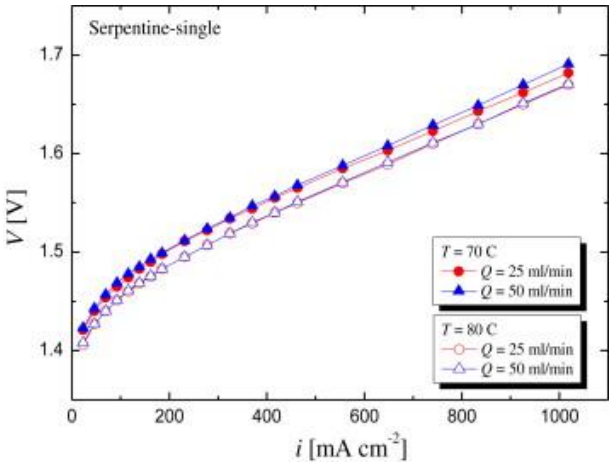

Figure 7: Characteristics of current density (i) and voltage (V) of a PEM electrolyser with serpentine-single flow field at a cell temperature (T) of 70 and 80 °C and a flow rate of circulating water (Q) at the anode of 25 and 50 ml min^{-1} [69].

2.1.3.6. Current Distribution

It is essential to use materials with high porosity on the anodic side of the cell where two opposite mass flows take place perpendicular to the membrane surface. A homogenous current distribution perpendicular to the MEA can be achieved by mounting porous platinised titanium sheets [70] on each side of the composite. Materials such as carbon foil or nickel foam could also be used on the cathode side of the cell [22].

2.1.3.7. Gas Collection and Treatment

Gaseous hydrogen is easily removed from liquid water at temperatures less than 100 °C, but the hydrogen may still contain water vapour that requires dehumidification [29]. Therefore, depending on the purity requirements, a drier (e.g. pressure swing adsorption dryer) can be used to remove residual water after a gas / liquid separation unit [6].

Hydrogen collected can either be stored in hydride tanks or pressurised bottles. The advantage of using hydride technology over the pressurised bottles is that it has a better management of hydrogen hazards, in particular those related with the operating pressure, since the same amount of hydrogen can be stored at a pressure of a few bars instead of a few hundred bars in a pressurised vessel [22].

2.1.4. Thermodynamics

Decomposition of water to hydrogen and oxygen gases by a direct current can be explained through the principles of thermodynamics. The first law of thermodynamics applied to an electrolysis system gives:

$$\Delta H = Q + W_{el} = T\Delta S + \Delta G \quad (4)$$

where ΔH is the enthalpy of the reaction, Q is the heat transferred, W_{el} is the electrical work, ΔS is the entropy change and ΔG is the Gibbs free energy. It is assumed that the system operates reversibly and isothermally [71].

Equilibrium voltage (at standard temperature and pressure) is obtained by subtracting the equilibrium potential of the anode from that of the cathode, as shown in Equation (5) [72]. It is the voltage at which the system is in equilibrium

and electrolysis occurs when there is a further increase in the voltage. Therefore, this voltage is also referred to as the open circuit voltage (OCV) [73].

$$E^{\circ} = E^{\circ}_{an} - E^{\circ}_{cat} \quad (5)$$

The equilibrium cell voltage at standard temperature and pressure, E° can be related to the Gibbs free energy, ΔG of the electrochemical reaction, as shown in Equation (6) [74].

$$\Delta G = -nFE^{\circ} \quad (6)$$

where n is the number of electrons transferred in the reaction and F is the Faraday constant (96486 C mol^{-1}).

The Gibbs free energy of a chemical reaction changes with temperature, reactant pressure and concentration. Therefore, the OCV at a given temperature and pressure can be found by the Nernst equation.

$$E = E^{\circ} + \frac{RT}{2F} ln \frac{P_{H_2} P_{O_2}^{1/2}}{a_{H_2O}} \quad (7)$$

where R is the universal gas constant (8.314 J mol^{-1}K^{-1}), T is the cell temperature, P_{H_2} and P_{O_2} are the partial pressures of hydrogen and oxygen and a_{H_2O} is the activity of water.

The Gibbs free energy for electrolysis is the minimum amount of electrical energy required to decompose water at a constant temperature and pressure. Thus electrolysis of water is thermodynamically unfavourable at room temperature and will only occur when sufficient electrical energy is supplied.

The Gibbs free energy, the electrochemical potential of the reaction, heat energy and therefore, the total energy requirement of the system can be calculated at

different temperatures and pressures. Figure 8 illustrates the variation of these parameters with temperature. It can be seen that the heat energy increases with increasing temperature due to the positive change in entropy. However, the Gibbs free energy of the system and the electrochemical potential decrease with increasing temperature. The variation of the total energy of the system with temperature is negligible. Electrolysis of water does not take place if operated under conditions below the 'electrical energy' line. The system is considered to be endothermic if operated under conditions below the total energy line, and exothermic if operated above.

Thermodynamics of the system is only a representation of the theoretical values. The equilibrium cell voltage required to drive the reaction forward is much greater than the theoretical value as there are various resistances (losses) involved in the system. The overvoltage caused by resistances is converted into heat, which can contribute to the endothermic water dissociation reaction. The voltage at which the system neither releases heat nor requires heat to proceed is called the 'thermoneutral voltage' and can be calculated using Equation (8) [75].

$$E_{TN} = \frac{\Delta H}{nF} \quad (8)$$

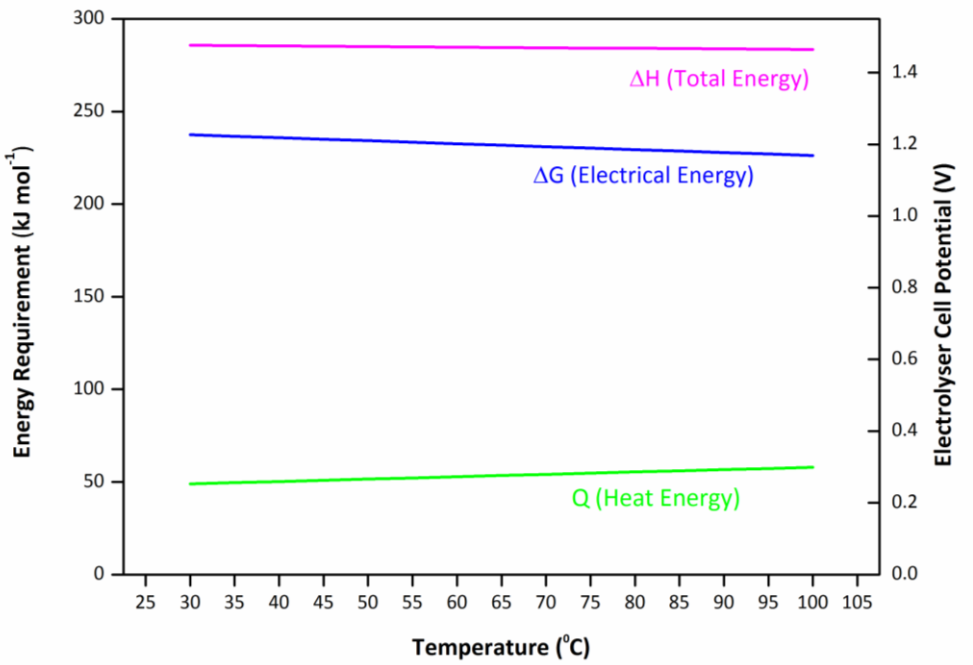

Figure 8: Cell potential and thermodynamic properties of a PEMWE cell as a function of temperature.

2.1.5. Efficiency

The efficiency of the electrolyser cell is greatly dependent on the respective operating conditions and can be expressed in many ways depending on the way the system is assessed and compared.

The efficiency of any energy system can be defined as [76]:

$$\eta = \frac{useful\ energy\ obtained}{energy\ available\ for\ conversion} \quad (9)$$

Electrical efficiency

The electrical efficiency can be expressed as shown in Equation (10) [68, 77].

$$\eta = \frac{W_{H_2}}{W_{el}} \tag{10}$$

where W_{H_2} is the chemical energy generated and W_{el} is the electrical energy required. These terms can be expressed as shown in Equations (11) and (12).

$$W_{H_2} = \dot{N}_{H_2} H \tag{11}$$

$$W_{el} = E_{cell} I t \tag{12}$$

where $\dot{N}_{H_2}$ is the molar rate of hydrogen produced, H is the heating value of hydrogen, E_{cell} is the cell voltage, I is the current and t is the time.

Voltage efficiency

This is the proportion of effective voltage required to split water to the total voltage applied to the entire electrolysis cell.

$$voltage\ efficiency = \frac{E_{an} - E_{cat}}{E_{cell}} \tag{13}$$

Faradaic efficiency

Faradaic efficiency describes the system in terms of charge transferred in a system facilitating the electrochemical reaction. It can be defined as the fraction of the Faradaic charge needed to force apart the water molecules in the real cell voltage.

$$\eta_{Faradaic} = \frac{I_{Faradaic}}{I_{Overall}} \quad (14)$$

where $I_{Faradaic}$ is the Faradaic charge and $I_{Overall}$ is the overall current [78].

Thermal efficiency

Thermal efficiency takes into account the thermal balance and can be defined as the percentage of the actual energy input in the real voltage when an additional voltage, above the reversible voltage, is required to maintain the thermal balance.

$$\eta_{Thermal} = \frac{\Delta H}{\Delta G + Losses} = \frac{E_{\mathrm{TN}}}{E_{cell}} \quad (15)$$

where E_{TN} is the thermoneutral voltage. Therefore, the equation can be simplified as shown below.

$$\eta_{Thermal}(25\ ^{\circ}\mathrm{C}) = \frac{1.48\ (V)}{E_{Cell}} \quad (16)$$

Therefore, it is possible for the efficiency of water electrolysis to exceed 100% as the system may absorb heat from the ambient if it operates in an endothermic mode.

Efficiency in terms of H_2 produced

This gives the hydrogen production rate per unit of electrical energy input. It can be used to compare different electrolysis systems by their hydrogen production capacity.

$$\eta_{H_2 production\ rate} = \frac{r_{H_2 production\ rate}}{\Delta G} = \frac{\dot{V}_{H_2}}{E_{cell} i t} \quad (17)$$

where $\dot{V}_{H_2}$ is the hydrogen production rate per unit volume of the electrolysis cell and i is the current density.

Efficiency in terms of energy loss

In this method, energy losses are subtracted from the total energy input and can be expressed as:

$$\eta_{net\ efficiency} = 1 - \frac{E_{loss}}{E_{cell}} \quad (18)$$

where E_{loss} is the voltage loss due to the resistances of the cell, which will be discussed in Section 2.1.7.

It can be concluded that energy efficiency could be improved either by increasing the operating temperature or pressure to thermodynamically reduce the energy needed to split water to obtain hydrogen, or by reducing the dominant components of the resistances to reduce the energy losses of the cell.

2.1.6. Electrochemical Kinetics

Anode and cathode chambers

Faraday's law states that the amount of chemical change on an electrode-electrolyte boundary is proportional to the quantity of electricity used. Quantity of electricity refers to the quantity of electrical charge. An ideal electrochemical process in which all species involved are governed by Faraday's law of electrolysis,

is considered in this report. Therefore the molar rate of the electrolysed species, $\dot{N}$, can be written as:

$$\dot{N} = \frac{iA}{nF} \tag{19}$$

where i is the current density, A is the surface area, n is the stoichiometric number of electrons transferred and F is the Faraday constant (96486 C mol^{-1}).

Assuming that the species are well mixed in the anodic and the cathodic chambers, thus taking into account that the surface concentrations does not differ significantly from the bulk phase, a mass balance of oxygen and water at the anode, and hydrogen at the cathode can be written as:

$$\dot{N}_{H_2O,in} - \dot{N}_{H_2O,out} = \frac{iA}{2F} \tag{20}$$

$$\dot{N}_{O_2,in} - \dot{N}_{O_2,out} = \frac{iA}{4F} \tag{21}$$

$$\dot{N}_{H_2,in} - \dot{N}_{H_2,out} = \frac{iA}{2F} \tag{22}$$

The rate of the electrolysis reaction can be expressed as given in Equation (23) [79] and the rate constant can be expressed using the Arrhenius equation as given in Equation (24).

$$Rate = kc^r \tag{23}$$

where k is the reaction rate coefficient and c is the concentration raised to the power r which is the reaction order.

$$k = Ae^{-\frac{E_A}{RT}} \tag{24}$$

where A is the pre-exponential factor, E_A is the activation energy and R is universal gas constant (8.314 J $mol^{-1}K^{-1}$). It should be noted that the concentration at the electrode surface should be considered for electrochemical reactions as they are surface processes.

The reaction rate coefficient remains a constant only for given reaction conditions. It changes with temperature, the electrode overpotential, catalyst surface, type of electrolyte and the concentration of the electrolyte solution. The following section describes the Butler-Volmer equation that relates these parameters to the reaction rate.

Anode and cathode layers

As explained in the previous section, the current exchanged in the system is related to the electrode kinetics. The Butler-Volmer equation for the process is shown in Equation (25) and can be used for the electrochemical reactions at the electrodes, assuming that there are no transport limitations [32, 79, 80].

$$i = i_0 \left[exp\left(\frac{\alpha_{an} nF\eta}{RT}\right) - exp\left(\frac{\alpha_{cat} nF\eta}{RT}\right) \right] \quad (25)$$

where i_0 represent the exchange current density, α_{an} and α_{cat} are the anodic and cathodic charge transfer coefficients and η is the overpotential. The exchange current densities of the anode and the cathode, being a function of the cell material (including the structure and physical parameters) and the local temperature, can be expressed in terms of reference exchange current densities as shown in Equations (26) and (27) [80-82].

$$i_{0,an} = i_{0,an}^{0} exp\left[-\frac{E_{A,an}}{R}\left(\frac{1}{T}-\frac{1}{T_0}\right)\right] \quad (26)$$

$$i_{0,cat} = i_{0,cat}^{0} exp\left[-\frac{E_{A,cat}}{R}\left(\frac{1}{T}-\frac{1}{T_0}\right)\right] \quad (27)$$

where $i_{0,an}^{0}$ and $i_{0,cat}^{0}$ are the reference exchange current densities of the anode and the cathode, $E_{A,an}$ and $E_{A,cat}$ are the activation energies of the anode and the cathode and T_0 is the reference temperature (298.15 K).

2.1.7. Electrochemical Potential of Electrolysis Cell

For the electrolysis process to proceed in a system, a number of barriers have to be overcome, requiring a sufficient electrical energy supply. The electrolyser cell can be considered as an electrical circuit with different resistances connected in series, as shown in Figure 9, and can be expressed as follows:

$$R_{Total} = R_{R,an} + R_{an} + R_{b,O_2} + R_m + R_{b,H_2} + R_{cat} + R_{R,cat} \quad (28)$$

where $R_{R,an}$ and $R_{R,cat}$ are the external electrical circuit resistances including the wiring and connections at the anode and cathode respectively, R_{an} and R_{cat} are the resistance due to overpotentials of the OER at the anode and the HER at the cathode respectively, R_{b,O_2} and R_{b,H_2} are the resistances due to partial coverage of the anode and the cathode by oxygen and hydrogen bubbles respectively and R_m is the resistance of the membrane.

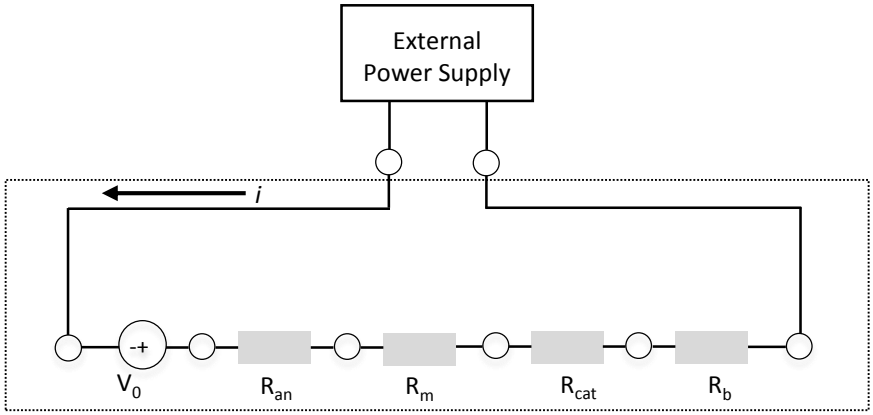

Figure 9: Equivalent circuit for the electrolysis process.

These losses can be categorised into three main sectors; activation overpotential, ohmic overpotential and diffusion overpotential, and are discussed in detail in Chapter 5.1.

Activation overpotential represents the charge transfer limitations of the system representing the electrochemical kinetic behaviour. Activation losses occur at low operating current densities and can be deduced from the Butler-Volmer equation.

Ohmic Overpotential occurs due to the resistances of the components of the electrolysis cell. The resistance of the membrane, which is a measure of the membrane conductivity, dominates the ohmic losses.

Diffusion Overpotential, also known as the concentration overpotential, is dictated by the access of reactant to the electrode surface. The formation of product bubbles has a significant effect here and becomes increasingly limiting at high current densities when a prominent amount of hydrogen and oxygen gasses are formed.

Therefore, the overall applied cell potential can be expressed by Equation (29) as a combination of the Nernst potential (E), activation overpotentials (η_{act}), ohmic overpotential (η_{ohm}), and diffusion overpotential (η_{dd}).

$$E_{cell} = E + \eta_{act} + \eta_{ohm} + \eta_{dd} \quad (29)$$

The Nernst potential, also known as the OCV, which is a function of both temperature and pressure, can be determined empirically by the Nernst equation given in Equation (7) [32, 74, 80, 83].

2.2. Diagnostic Techniques

The complex behaviour of mass transport, energy transfer and electrochemical processes in electrolysers lead to heterogeneity in their performance. Hence, the bulk measurements made on electrolysers will not accurately represent performance at all parts of the cell. This section of the thesis focuses on different diagnostic techniques that could be employed to distinguish the structure-property-performance relationship between an electrolyser and its components.

2.2.1. Electrical Techniques

2.2.1.1. Polarisation Measurements

A polarisation curve is a plot of cell potential against the current density under a set of constant operating conditions and is the standard electrochemical technique for the characterisation of electrolysis systems. It provides information about the overpotentials of the system under the operating conditions. Furthermore, these

curves allow characterisation of the effect of certain parameters such as material compositions, water flow rate, pressure and temperature on the performance of the electrolysis system.

Figure 10 shows an ideal polarisation curve for PEM electrolysers and it can be divided into three main regions: low current density, intermediate current density and high current density. The sharp increase in cell potential at low current densities represents the activation losses and the linear increase of the cell potential at intermediate current densities represent the ohmic losses in the system. Finally, the drastic increase of the cell potential at high current densities is due to mass transport effects in the system.

These curves provide information on the performance of an electrolysis cell as a whole but fail to produce comprehensive information about the performance of individual components within the cell. In addition, they are incapable of differentiating different mechanisms from each other and of resolving time dependent processes that occur within electrolysis cells.

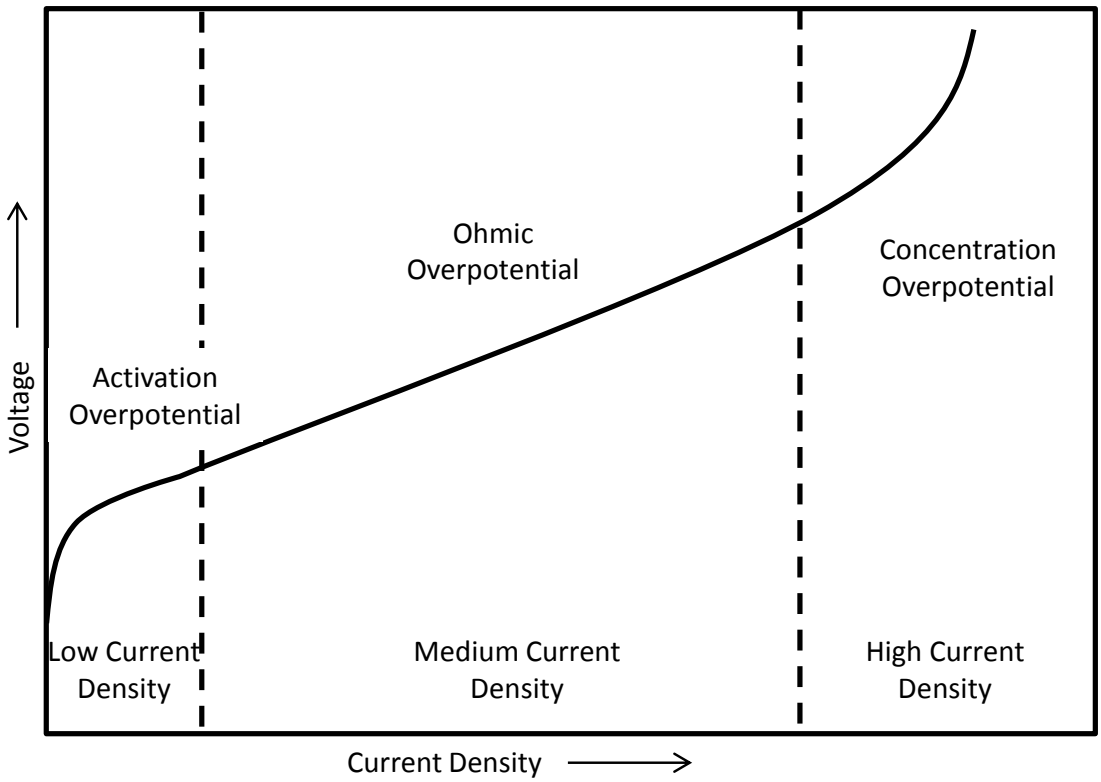

Figure 10: Ideal polarisation curve of a PEMWE showing activation, ohmic and concentration overpotential regions.

2.2.1.2. Electrochemical Impedance Spectroscopy (EIS)

It is necessary to make an in-depth study of the inner workings of the electrolysis process and analyse its steady-state and transient behaviour, in order to improve design and operation of components. EIS is a powerful technique that has been used extensively to characterise fuel cell performance. However, EIS application in the field of electrolysers is much less developed.

In this method, a small AC voltage or current perturbation of known amplitude is added to a constant DC signal with a changing frequency. The amplitude and phase of the resulting signal are measured as a function of frequency [84].

Impedance spectra can be plotted either in Bode or Nyquist form. In a Bode plot, the amplitude and the phase of the impedance is plotted as a function of frequency, while in a Nyquist plot the imaginary part of the impedance is plotted against the real part at each frequency. Figure 11 (a) shows a typical impedance spectra in Nyquist form with a single arc, where the frequency increases from right to the left, and Figure 11 (b) and (c) show two types of Bode plots [84, 85]. This single arc is equivalent to the Randles circuit, which is the most common model of an electrochemical interface and is shown as an insertion in Figure 11 (a). It includes electrolyte resistance (R_{el}), charge transfer resistance (R_{ct}) of the electrode process and double-layer capacitance (C_{dl}) [86].

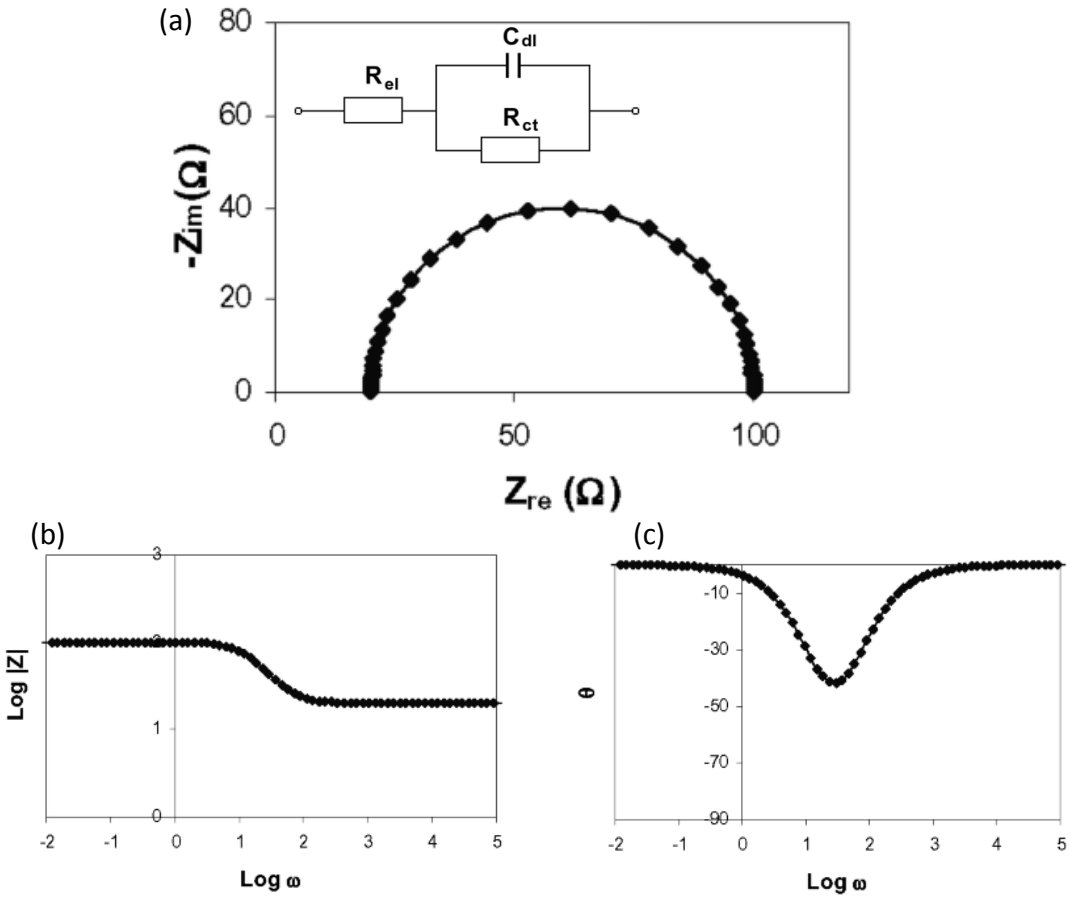

Figure 11: (a) Typical Nyquist plot simulated over the frequency range 100 kHz –0.01 Hz and the Randles equivalent circuit. (b) and (c) Bode plots simulated over the frequency range 100 kHz– 0.01 Hz [87].

Electrochemical reactions involved with PEMWEs mainly involve electrolyte resistance, charge transfer at the electrode surface and mass transfer from the bulk solution to the electrode surface. Each of these processes can be considered as an electric component and therefore, allowing the whole reaction process to be represented as an electric circuit composed of resistors, capacitors or constant phase elements (CPE) combined in series or parallel [87]. Values of each of these components can be determined by fitting EIS data to an appropriate equivalent circuit that will allow the performance of different components of the system to be deconvoluted.

EIS studies have been extensively performed on PEM fuel cells [88-91] and stacks [86, 92] in various operating conditions. However, there is only a scarce amount of work reported on the use of EIS on PEMWEs. The GenHyPEM program used EIS to evaluate the electrochemical performances of various MEAs of different composition, size and shape in both single and stack configurations of PEM electrolysers [43]. System operating parameters [93] and electrocatalyst performance [41] of PEM electrolysers have all benefitted from the application of EIS.

2.2.1.3. Current Density Mapping

The current density distribution (CDD) in PEMWE is mainly a function of the microstructure of the gas diffusion layers, electrodes and the flow fields. This non-uniformity of current density across the entire active area is critical for optimising the electrolyser performance. A non-uniform current could drastically effect catalyst utilisation, energy efficiencies and the lifetime of the cell. Therefore, the ability to accurately measure the current distribution in a PEMWE is important in order to improve the performance and contribute to a better understanding of

mass transport processes in the cell, which leads to an optimised design of electrolyser components.

To date, there are no studies present in literature on CDD measurements on PEMWE systems. However, a number of methods for measuring local CDD in PEMFCs have been reported [94]. Stumper *et al.* [95] has suggested three methods to determine the distribution of the current density in a PEM cell:

Partial MEA approach – This technique involves testing portions or segments of the MEA independently, either by masking different areas or selectively catalysing segments of the MEA.

Sub cell approach – This technique involves electrically isolating individual locations of the catalysed anode and opposing cathode from the main cell to measure the performance of the desired location [96].

Current distribution mapping – This is the most advanced method and involves an array of shunt resistors that are located normal to an unmodified MEA surface between the flow fields and a bus plate.

Resistors network method for CDD mapping used the same principle as the current density mapping technique suggested by Stumper *et al*. [95]. In this method the electrochemical characterisation could be done either passively (connecting the resistor network to shunt resistors) or actively (connecting the resistor network to the measurement unit) [94].

Sun *et al*. [97, 98] used a specially designed gasket material made of epoxy resin and glass cloth, which consists with a pattern of the flow field. In addition, segmented flow field approach in PEM [99-101] and direct methanol fuel cells (DMFC) [102] and Hall effect sensor method [103] have been investigated for CDD measurements. Currently, the PCB approach is the most commonly used method to map CDD [58-61, 104, 105]. In this method, the current collector plate is

replaced with a PCB board where electrically isolated paths for individual voltage / current collection are machined. This technique has become attractive as simpler cells with lesser components can be used for current density measurements. Figure 12 shows the geometry of a PCB current collector with a single flow channel and the exploded view of a PEMFC that was employed by Brett *et al*. [60] for CDD measurements.

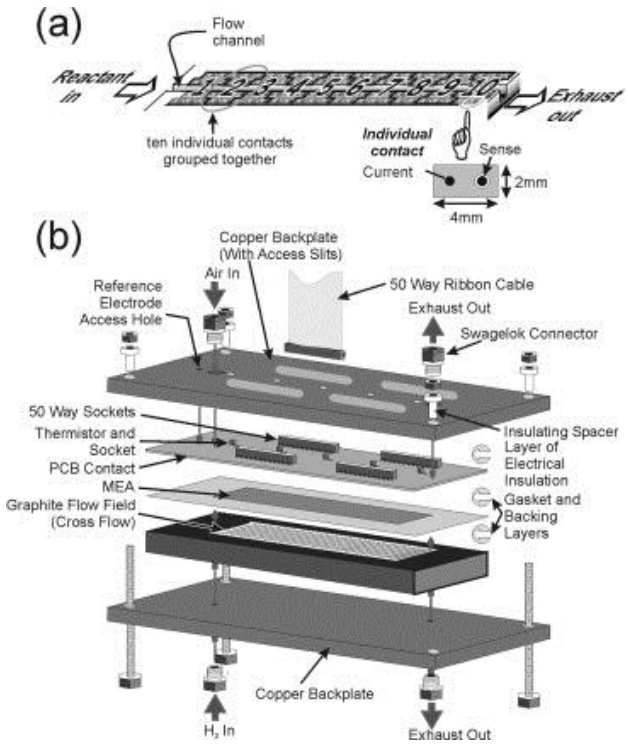

Figure 12: (a) Diagram of PCB contact electrode geometry for single channel flow field. (b) Exploded view of fuel cell [60].

2.2.2. Non-Electrical Techniques

2.2.2.1. Optical Visualisation

As electrolysis progresses, hydrogen and oxygen bubbles form on the cathode and the anode surfaces respectively and they detach from the electrode surfaces only when they grow up to a certain size [106]. These gas bubbles add an extra resistance to the electrolysis process as they cover the electrode surfaces by blocking the access of reactant water to the electrode.

Another concern governing this phenomenon is the water distribution in the channels, as coexistence of the gases produced and feed water creates a two-phase flow in the anode and cathode chambers of a PEM electrolyser. The flow characteristics in channels at different operating conditions influence performance, efficiency and degradation. Hence, understanding the formation of bubbles and their behaviour is vital in developing PEMWEs.

There are many scanning techniques present in the literature for PEMFCs: nuclear magnetic resonance (NMR), beam interrogation (e.g. neutron imaging, X-ray and electron microscopy) and direct visualisation [107, 108]. However, direct optical visualisation is the most commonly used method as it has the potential to provide high temporal and spatial resolution *in situ* information about fluid dynamics in the flow channels and upper layers of the GDL.

Various methods and transparent cell designs have been used to achieve direct visualisation into internal flow channels of PEMFCs. Ous and Arcoumanis [109-112], Zhan *et al.* [113], Spernjak *et al*. [114] and Dillet *et al*. [115] present transparent cell designs coupled with high speed cameras that allow optical access to the flow channels to study the effect of operating conditions on the accumulation of liquid water. Furthermore, cathode flooding [116-119] and two-phase flow mapping [120] have also been reported. Figure 13 illustrates a

structure of a typical transparent FC and the system set-up for visualisation measurements.

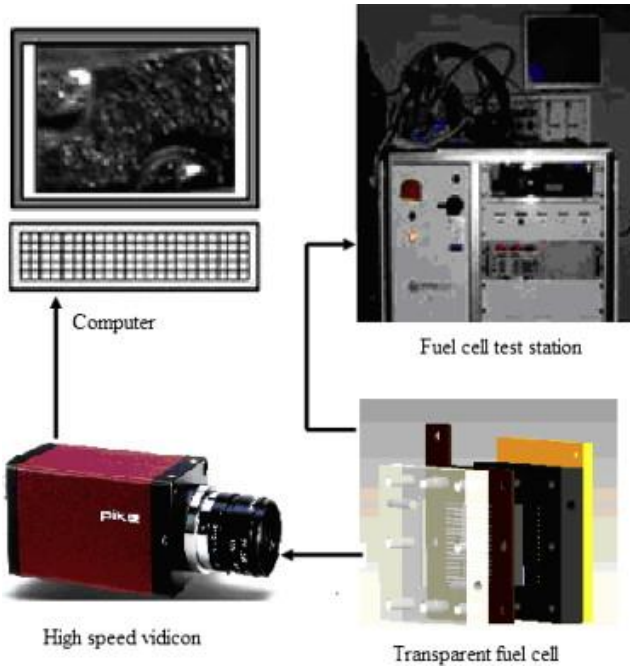

Figure 13: PEMFC with optical access and system set up for direct visualisation of the flow channels [113].

To date, relatively little has been done to understand how two-phase flow in PEMWEs influences its performance. Ito *et al*. [69] presents a theoretical evaluation of two-phase flow characteristics for different flow field designs. Nie and Chen [121] has developed a numerical three-dimensional model to examine the flow features of two-phase flow in the anode flow field plate. However, there are no studies at present that employ direct visualisation of PEMWEs.

2.2.2.2. Thermal Imaging

Although electrolysis is an endothermic process, there is an overall increase in the cell temperature mainly due to the electrical resistances when in operation (Joule heating). Therefore, the temperature distribution across the cell gives important information on the non-uniform distribution of reaction and different resistances between layers of the cell.

There are a number of methods present in literature that allow the examination of temperature distribution of operational PEMFC systems. The traditional method for temperature measurements is the use of thermocouples that gives the temperature at specific points [122]. Alternatively, infrared (IR) thermal imaging has attracted attention in the recent years as it requires no sensor placement on a surface and allows the entire surface to be characterised in a single measurement without disturbing the system. This method provides high spatial resolution (<1 mm) that generates detailed data sets and has fast acquisition time that enables dynamic phenomena to be studied [123].

There are several studies present in literature that employ the IR thermal imaging technology to examine temperature characteristics of GDLs [124], PEMFCs and stacks [125, 126] and high temperature FCs [123]. Different PEMFC designs and materials for thermal imaging using IR cameras have also been examined [127]. Figure 14 shows the positioning of the IR thermal imaging camera in the studies done by Matian *et al.* [125].

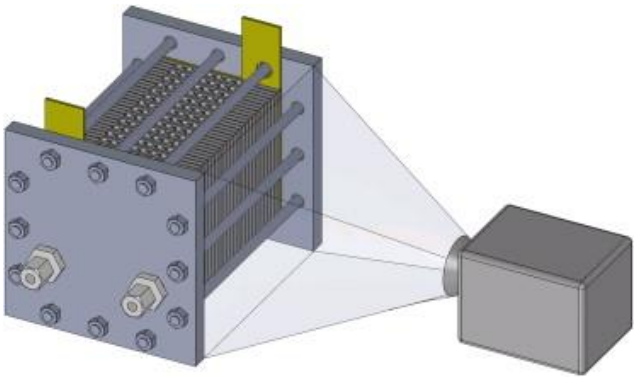

Figure 14: Fuel Cell stack and thermal imaging camera position [125].

3. Methodology

This chapter illustrates the engineering principles and theories that will be employed for calculations and discussion of observations made in the results chapter. The scientific theories of various experimental procedures employed are also discussed.

3.1. Engineering Measurements and Diagnostics

3.1.1. Heat Balance

A basic thermodynamic analysis can be carried out on the water electrolysis cell to determine the rate of heat loss as a function of operating current density and feed water flow rate. Furthermore, rate of heat loss can be related to efficiency of the cell to validate the performance of the cell at different current density ranges.

The heat flow diagram in Figure 15 illustrates that water enters the electrolyser on the anode side and hydrogen and oxygen gases exit with unreacted water. The first law of thermodynamics applied to the control system gives:

$$\dot{Q}_{H_2O,in} + \dot{Q}_E = \dot{Q}_{H_2O,out,an} + \dot{Q}_{H_2O,out,cat} + \dot{Q}_{O_2} + \dot{Q}_{H_2} + \dot{Q}_L \quad (30)$$

Where $\dot{Q}_{H_2O}$ is the heat flow rate of water, $\dot{Q}_{O_2}$ is the heat flow rate of oxygen generated, $\dot{Q}_{H_2}$ is the heat flow rate of hydrogen generated, $\dot{Q}_L$ is the rate of heat lost to the surrounding and $\dot{Q}_E$ is the rate of heat generated by electrolysis given by:

$$\dot{Q}_E = I\left[E_{cell} - \frac{\Delta H_{cell}}{nF}\right] \quad (31)$$

The heat transfer within the device is complicated by the transportation of water across the membrane by diffusion and electro-osmotic drag, as shown in Figure 15. The amount of water transported to the cathode side due to these effects are given by [128-130]:

$$\dot{N}_{H_2O,dd} = \frac{AD_w}{\delta_m}\left(C_{H_2O,cat} - C_{H_2O,an}\right) \quad (32)$$

$$\dot{N}_{H_2O,eo} = n_d \frac{I_{cell}}{F} \quad (33)$$

where $\dot{N}_{H_2O,dd}$ and $\dot{N}_{H_2O,eo}$ are the molar flow rates of water due to diffusion and electro-osmosis, A is the surface area of the membrane, D_w is the water diffusion coefficient in the membrane, δ_m the membrane thickness, C_{H_2O} is the water concentrations and n_d is the electro-osmotic drag coefficient $\left[mol_{H_2O}/mol_{H^+}\right]$.

The heat flow rate of water and gases can be calculated using the specific heat capacities of each component using the following equation:

$$\dot{Q}_i = \dot{m}_i C_{p,i} T \quad (34)$$

Where $\dot{m}_i$ is the mass flow rate and $C_{p,i}$ is the specific heat capacity of component i.

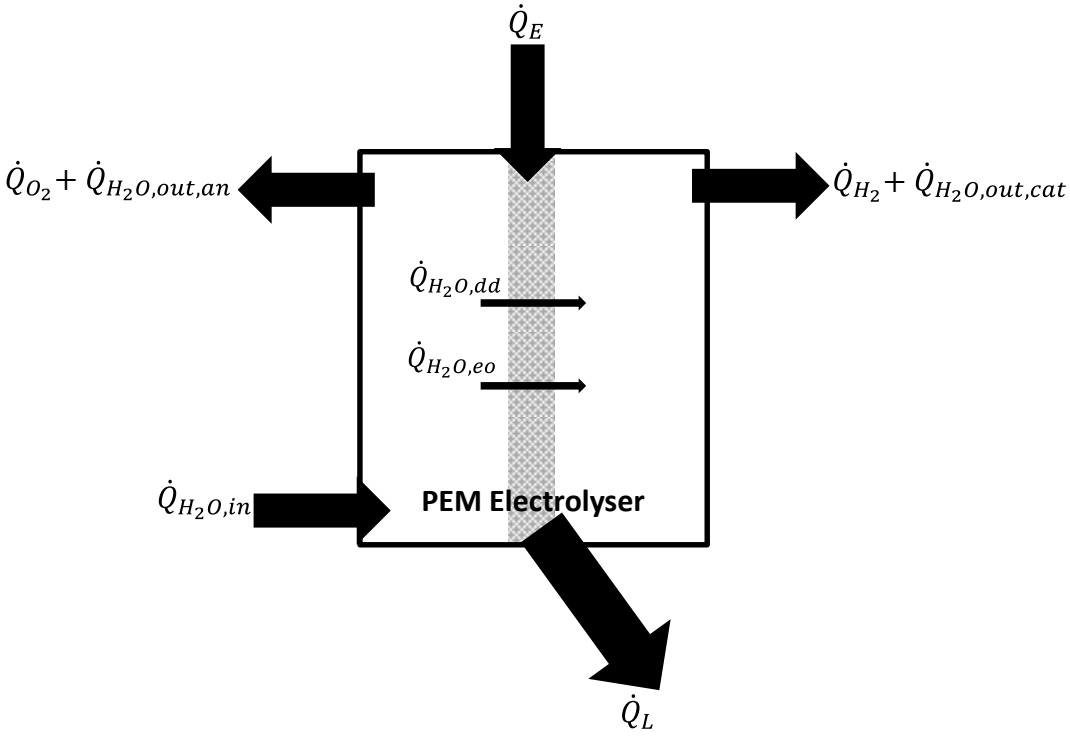

Figure 15: Heat flow diagram of a PEM water electrolyser.

3.1.2. Flow Rate of Feed Water

The ratio between the amount of circulating water to the amount of water required to service the process (ζ) is given by Equation (35):

$$\zeta = \left(\frac{G_{in}}{G_{con}+G_{eo}}\right) \tag{35}$$

where, G_{in} is the mass flux of the feed water flow rate, G_{con} is the mass flux of water consumed by the reaction and G_{eo} is the mass flux of water transported to the cathode side due to electro-osmotic drag.

A value of ζ=1 is sufficient to sustain water electrolysis [69]. However, a value of ~5 is usually chosen for the operation of practical large-scale electrolysers to

prevent the membrane from being exposed and drying out [63]. Figure 16 shows the variation of ζ for the current density range and feed water flow rates considered in this study for PEMWEs with active areas of (a) 28 cm^2 and (b) 25 cm^2. It can be seen that the ζ reaches a value close to 1 for 28 cm^2 and 25 cm^2 cells at 1 A cm^{-2} when operated at 1 ml min^{-1}. Therefore, it relates that the water flow rates considered in this study are sufficient to keep the MEA hydrated throughout the operation of electrolysis. This study spans the practical range of flow rates used in real electrolysers.

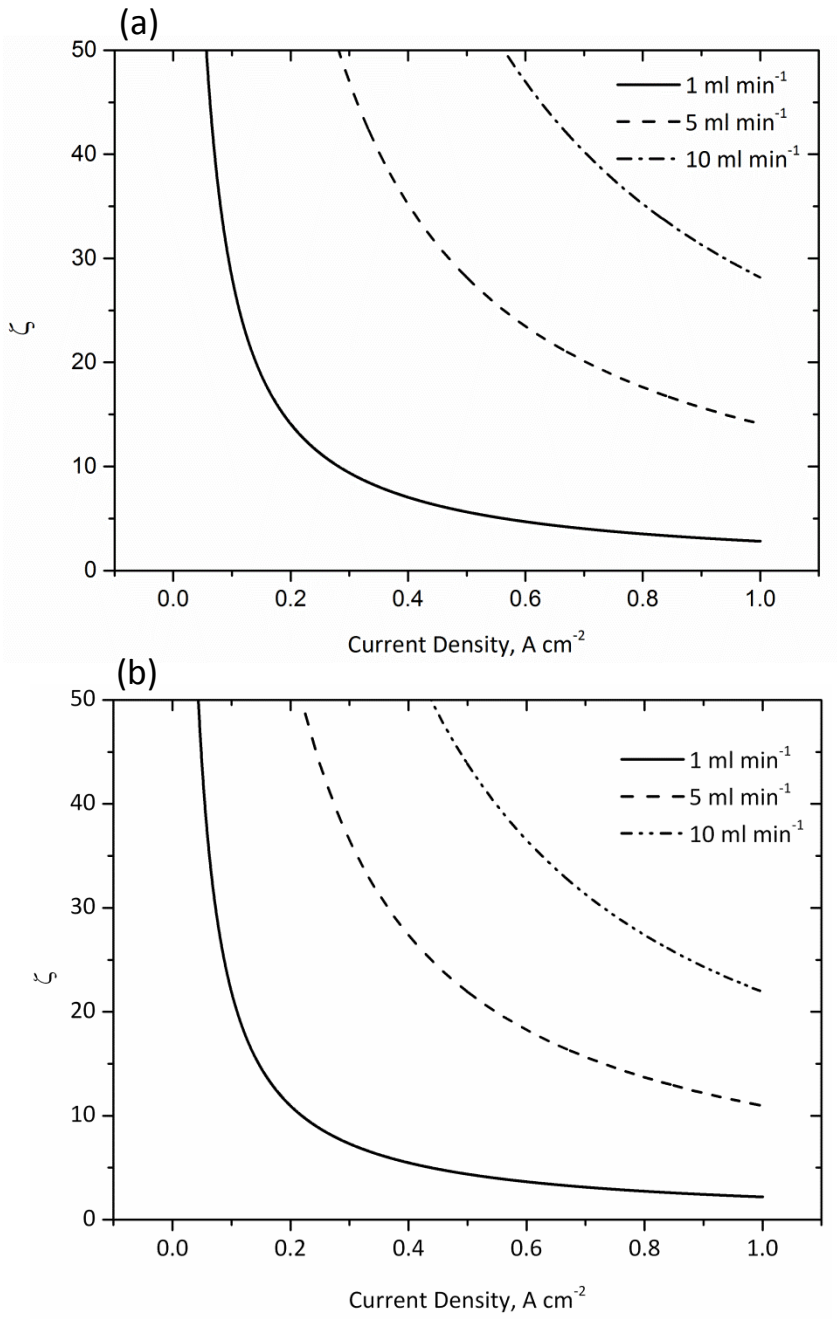

Figure 16: Variation of ζ from 0 – 1 A cm^{-2} when the PEMWE of (a) 28 cm^2 and (b) 25 cm^2 are operating with feed water flow rates of 1 ml min^{-1}, 5 ml min^{-1} and 10 ml min^{-1}.

3.1.3. Electrochemical Impedance Spectroscopy (EIS)

Figure 17 (a) show the shape of a Nyquist plot for an operational PEMWE with charge and mass transfer limitations. The high frequency arc represents the charge transfer of the electrocatalyst layer (dominated by the anode reaction). The ohmic resistance, including the membrane resistance together with the GDL, bipolar plate and contact resistances, is given by the high-frequency intercept with the real axis [131] and the diameter of the high frequencies arc relates to the charge transfer resistance of the electrodes. The low frequency arc is attributed to the mass transport limitations in electrolysis and its diameter corresponds to the resistance caused by the formation of bubbles limiting reactant water access to the electrodes.

The electrical analogy representing the Nyquist plot is shown in Figure 17 (b) [86, 89] where R_{el} is attributed to the internal resistance of the cell, R_{ct} and CPE_1 represent the charge transfer resistance of the OER and constant phase element at the highest frequency which relates to the electrode structure. R_b and CPE_2 represent the resistance and capacitance due to the formation of bubbles (mass transport limitations).

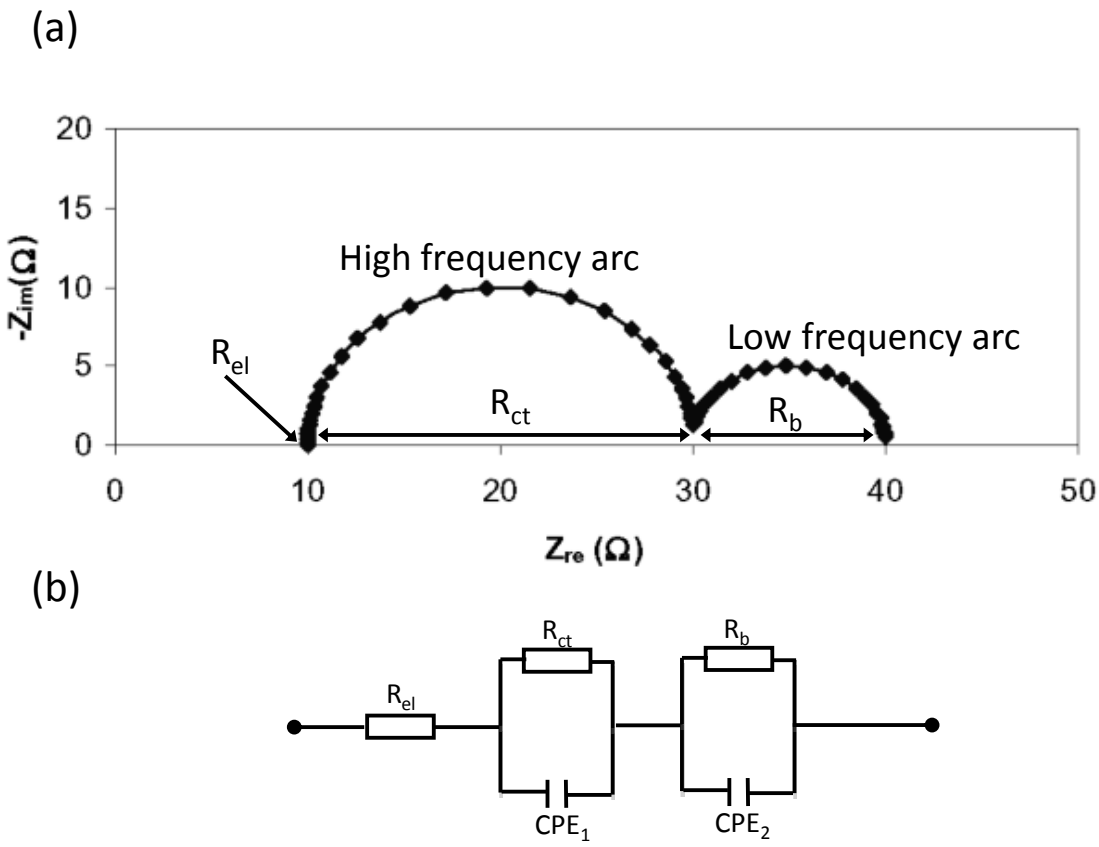

Figure 17: (a) Nyquist plot for a PEM electrolyser with charge and mass transport limitations. (b) Equivalent circuit.

3.1.4. Two Phase Flow and Bubble Phenomena

The Reynolds number (Equation (36)) is a dimensionless quantity that describes the flow in different fluid situations. This is typically in the range of 0.1 – 10 for the feed water flow rates considered in this study and hence the flow is considered to be laminar.

$$Re = \frac{\rho u_l D}{\mu} \quad (36)$$

where u_l is the velocity of water in a channel (m s^{-1}), μ is the dynamic viscosity of water (Pa s) and D is the hydraulic diameter of the channel which can be written as below for rectangular channels.

$$D = \frac{4A}{P} \quad (37)$$

where P is the wetted perimeter of the channel.

Two phase flow

Two flow regimes predominate in the channels of PEM electrolyser cells:

Single phase flow occurs when there is only liquid water flowing in the channels. This occurs at zero or very low current densities when there is no generation of gases or when the product dissolves in the water.

Two phase flow can be observed when reaction is such that gas bubbles form and detach from the electrode. Liquid water and gases produced distribute themselves in different flow regimes in the channels depending on reaction geometry and operating conditions. These flow regimes are illustrated in Figure 18, and include: bubbly flow, slug flow, churn flow and annular flow [132].

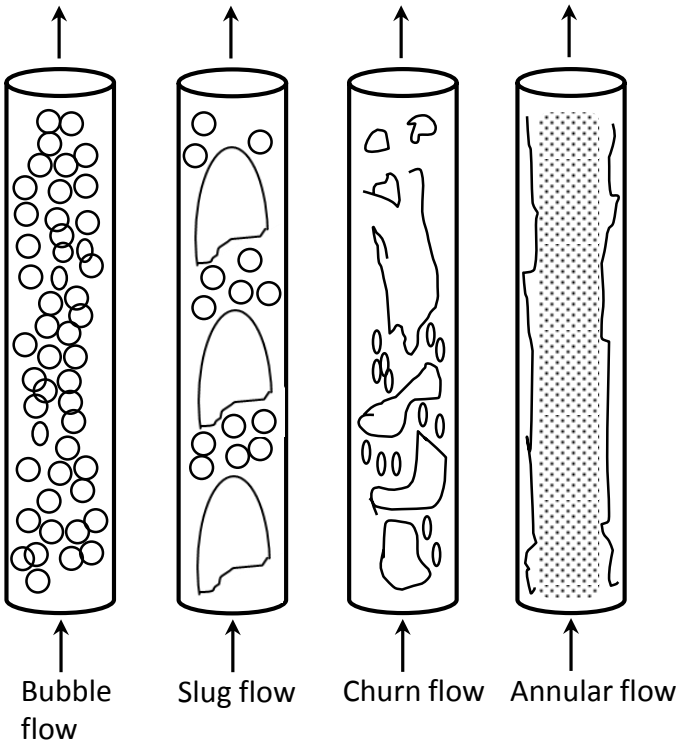

Figure 18: Flow regimes in a vertical channel where gas is in coexistence with liquid water.

Bubbly Flow: The bubbles are dispersed in a discrete form in the continuous liquid phase. The bubbles are typically nearly spherical and have a diameter much smaller than the channel width. However, each of them may vary in size and shape [133]. This type of flow is observed at high liquid flows.

Slug Flow: It is also referred to as *Plug*, *Segmented*, *elongated bubble*, *intermittent*, *Taylor* or *Train flow*. As the gas void fraction increases and the proximity of bubbles is very close, elongated cylindrical bubbles longer than the channel width are formed due to pressure squeezing mechanism in the surface tension dominated region [134]. These bubbles are known as Taylor bubbles and have a characteristic shape similar to a bullet with a hemispherical nose with a blunt tail end [133]. They are separated by slugs of continuous liquid that contains small gas bubbles. The liquid between the pipe and the Taylor bubble flows downward in the form of a thin falling film [135].

Churn Flow: It occurs at very high gas velocities when the flow becomes unstable and frothy with fluid travelling in a chaotic form. The instability of the flow is due to the relative parity of the gravitational and shear forces acting in opposing directions. This flow pattern is an intermediate regime between slug and annular flow regimes [133].

Annular Flow: It is a stable flow regime and is characterised by the continuity of the gas phase along the pipe in the core. This flow regime is observed when the interfacial shear of the high velocity gas on the liquid film becomes dominant over gravity. The gas flows as a continuous phase up the centre of the tube whereas the liquid is expelled from the centre and flows as a thin film on the wall [133].

Forces and their regimes (surface tension, inertial and transitional regime) dominating the flow patterns are shown in Figure 19 [134].

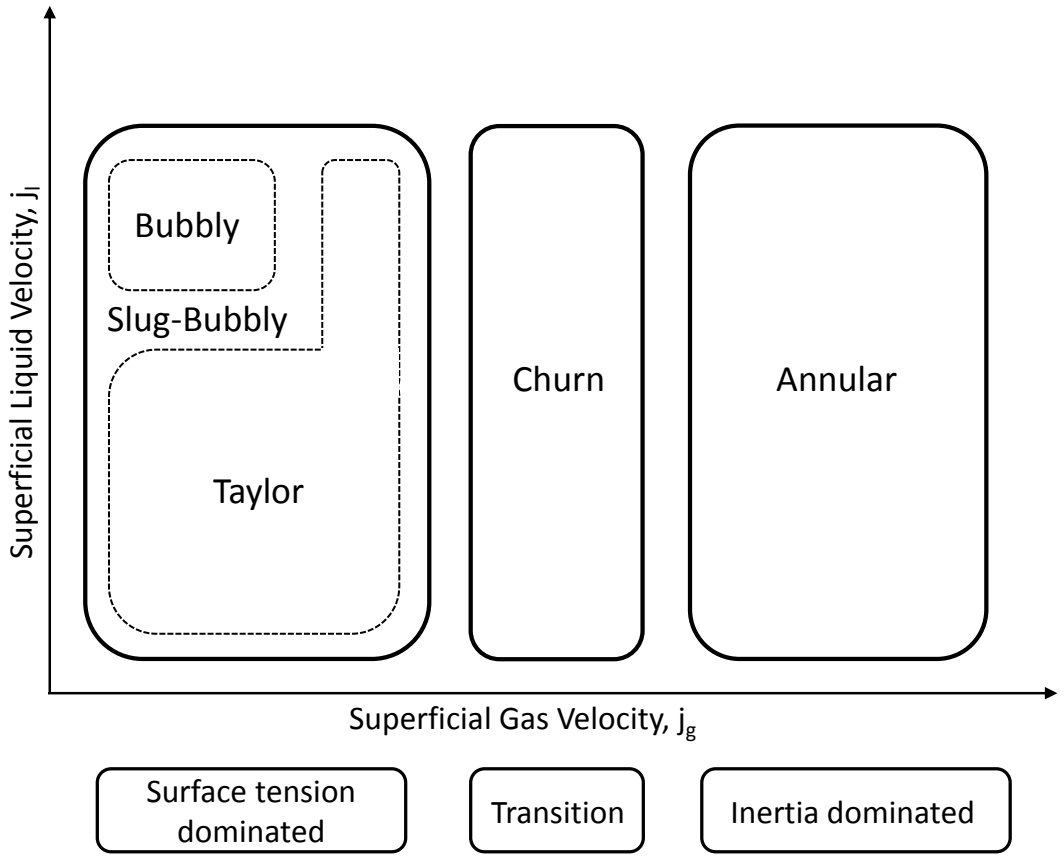

Figure 19: Classification of flow patterns and the dominating force in each regime adapted from [134].

Parameters determining flow regimes and their transitions [136]:

*Flow Orientation***:** The flow patterns and dominating forces acting on the flow are dependent on whether the cell is horizontal or vertical.

Channel Size: Channel size differentiates macro and micro-channel flow that have different transition properties. In micro channels, surface tension forces are dominant of buoyancy forces and satisfy the following condition [137]:

$$Bo = \frac{\Delta \rho g D_b^2}{\gamma} \quad (38)$$

Where Bo is the Bond number, $\Delta\rho$ is the difference between the density of liquid and gas, g is gravitational acceleration and γ is the surface tension of the interface. The flow channels considered in this study satisfy this relation and hence fall under micro channels.

Channel geometry: Studies have shown that the shape of the channel (rectangular, circular, triangular, etc.) has an influence on the flow patterns observed.

Wall wetting properties: The hydrophobic / hydrophilic (wettability) nature of the channel walls determines the contact angle, θ. Higher contact angles inhibit the liquid from spreading on the tube walls. Therefore, conditions for flow regime transition depend on the contact angle values.

Fluid Properties: Studies have shown that surface tension which is a measure of the fluid properties has an influence on the flow regime transition.

The flow regimes observed in a PEM electrolyser channels vary between these flow regimes depending on the superficial velocity of each phase, which is defined as the bulk velocity of the phase based on the flow area of the channel [120].

The superficial gas velocities of each phase are related to the mass flux (G) and the quality of the two-phase flow (x) which can be found using Equations (39)-(44) [69, 138]:

$$G_g = \frac{Imw_{O_2}}{4Fn_{ch}A_{ch}} \quad (39)$$

$$G_{con} = \frac{Imw_{H_2O}}{2Fn_{ch}A_{ch}} \quad (40)$$

$$G_{eo} = n_{drag}\frac{Imw_{H_2O}}{Fn_{ch}A_{ch}} \quad (41)$$

$$G_l = G_{in} - G_{con} - G_{eo} \quad (42)$$

where G_g, G_l, G_{in}, G_{con} and G_{eo} are the mass fluxes of gas , liquid, feed water, water consumed and water transported due to electro-osmotic drag; n_{drag} is the drag coefficient, mw_{O_2} and mw_{H_2O} are the molecular weight of oxygen and water, n_{ch} is the number of channels and A_{ch} is the cross sectional area of a channel, giving:

$$x = \frac{G_g}{G_g + G_l} \tag{43}$$

$$G = G_g + G_l \tag{44}$$

The superficial velocities of gas, j_g, and liquid, j_l:

$$j_g = {Gx}/{\rho_{O_2}} \ , j_l = {G(1-x)}/{\rho_{H_2O}} \tag{45}$$

When analysing two-phase flow that exhibit various flow regimes, it is important to have a good understanding of transition between them. These transitions are usually presented in the form of void fraction, using simple geometrical consideration.

The void fraction, α_v of the cell is given by [139]:

$$\alpha_v = \frac{j_g}{u_g} \tag{46}$$

where u_g is the gas velocity given by:

$$u_g = C_1\left(j_g + j_l\right) + u_{go} \tag{47}$$

and C_1 (the ratio of maximum to mean velocity) has a value close to 1.2 for rectangular channels [139] and u_{go} is the velocity in the stagnant water column given by:

$$u_{go} = 0.35\sqrt{(gD_e)} \quad (48)$$

where g is the acceleration due to gravity (9.81 m s^{-2}) and D_e is the equi-periphery diameter, given by;

$$D_e = \frac{periphery}{\pi} \quad (49)$$

Bubble Phenomena

Bubbles formed on the electrode surface get detached only after they reach a critical diameter. The detachment diameter of a bubble in an open water pool when a gas is injected through an orifice is given by [140]:

$$D_b = 2\left[\frac{\gamma R_0}{g\Delta\rho}\right]^{1/3} \quad (50)$$

where R_0 is the radius of the gas nozzle.

Bubble detachment and its motion along the channel are dependent on a balance of forces acting on it. These forces acting on a spherical bubble can either favour bubble detachment (detaching / positive forces) or oppose detachment (attaching / negative forces) [141-144].

Buoyancy force (F_B): is a detaching force as it acts vertically upwards.

$$F_B = V_b\Delta\rho g = \Delta\rho g\frac{4}{3}\pi R_b^3 \quad (51)$$

where V_b is the volume of the bubble and R_b is the radius of the bubble.

Surface tension force (F_γ): is the force that acts to hold bubbles on to the solid surface, thus it is an attaching force

$$F_\gamma = \pi D_b \gamma sin^2(\theta) \quad (52)$$

Inertia forces (F_I): consists of two parts; the inertia due to bubble motion (bubble inertia) and the inertia of the liquid that is pushed by the accelerating surface of the expanding bubble (liquid inertia). The bubble inertia is attaching and the direction of the liquid inertia depends on the relative magnitude of the velocity of bubble centre and superficial liquid velocity.

$$F_I = \frac{d}{dt}\left(\rho_g V_b \frac{ds}{dt}\right) + \frac{d}{dt}\left[\rho_l C_{MC} V_b \left(\frac{ds}{dt} - j_l\right)\right] \quad (53)$$

where $\frac{ds}{dt}$ is the velocity of the bubble centre and C_{MC} is the added mass coefficient.

Drag force (F_D): when the bubble velocity is greater than the liquid velocity, the bubble front has to push the liquid and hence drag force acts as an attaching force. In reverse conditions, drag force acts as a detaching force as the surrounding liquid pulls the bubble away from the surface.

$$F_D = \frac{1}{2} n_d \rho_l V_l A_p \quad (54)$$

where V_l is the liquid velocity, A_p is the projected area of the droplet and n_d is the drag coefficient.

Bubble flow is characterised by uniform distribution of discrete bubbles with diameter considerably smaller than the channel width (D_b<w_{ch}) in a continuous liquid phase. Whereas slug flow is characterised by 'bullet shaped' bubbles which have diameters almost equal to the channel width ($D_b \approx w_{ch}$) and with elongation along the channel direction.

Therefore, from first principles it can be determined that the criterion for bubbly flow is:

$$\frac{D_b}{w_{ch}} < 1 \quad (55)$$

and for slug flow:

$$\frac{D_b}{w_{ch}} \cong 1 \quad (56)$$

The spherical bubbles in the bubbly region increase in volume as the flow transitions to the slug flow region, forming 'bullet shaped' bubbles with a length, l_b that satisfies:

$$\frac{D_b}{l_b} < 1 \quad (57)$$

3.2. Construction of Materials

3.2.1. Multilayer Bonding of Pre-pregs

Multilayer bonding of pre-preg was employed in this study to attach PCB boards together by hot pressing. The 'press cycle' for bonding multilayers is of utmost importance to obtain results of high quality. It expresses the relation between the temperature, pressure and time in three different regimes, which are pre-preg melt down and flow, resin cure and cooling, as shown in Figure 20 [145].

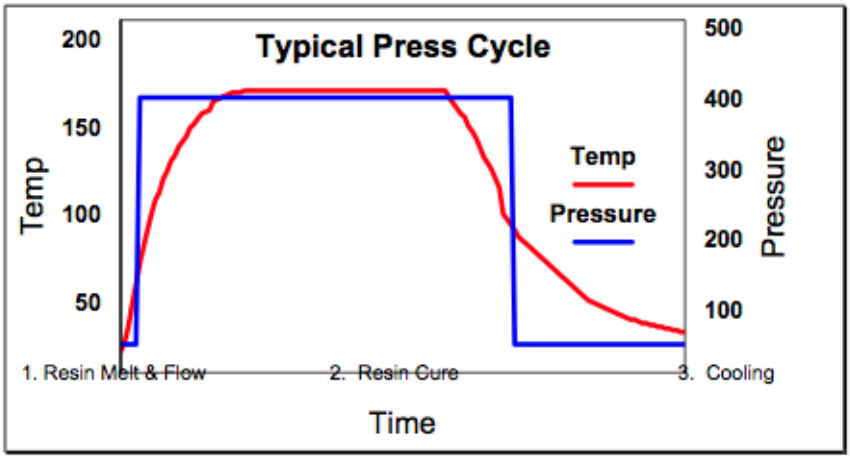

Figure 20: Press cycle for multilayer bonding [145].

Resin Melt and Flow - In this region the plates get heated up, hence the resin in the pre-preg melts at around 60 °C and the pressure applied makes the pre-preg flow. The PCB stack should be wrapped in aluminium foil that will act as a lagging material as the stack needs to be heated up at a rate of 5 to 8 °C min^{-1}. Further, the aluminium foil evens out the heat flow into the stack. The resin becomes less viscous as it melts until it reaches its minimum melt viscosity, the point at which it flows through the PCB plates. The resin is more viscous after this point until about 140 °C at which it gels or sets.

Resin Cure - Once the resin has flowed and gelled, it requires continued heat and pressure for full cure. Typically 30 minutes at 170 °C for FR4 boards.

Cool Down - The cooling down rate should be similar to the heating up rate and should be even throughout the stack. Failing to do so will result in bowed boards due to thermal shock.

3.2.2. Electroplating

Electroplating technology was used to obtain a layer of gold on the PCB flow field boards used in this study. In order to obtain a stable and even layer of gold, the copper surface needs to be cleaned. The science behind plating procedure is as explained in the following section.

Copper surface pre-treatment

Contamination of the copper surface has a major effect on the electroplating results and even dust could hinder the desired performance of electroplating.

Therefore, an ultrasonic cleaning for gross fragment removal and an acidified peroxide chemistry for fine fragments, surface contamination and oxide removal was used. The acidified hydrogen peroxide solution used targets the Cu^{+}/Cu^{2+} species on the surface of the copper layer, leaving the copper layer intact as expressed in Equations (58) – (61) based on Fenton's mechanism [146].

$$Cu^{+} + H_2O_2 \rightarrow Cu^{2+} + OH^{-} + OH \cdot \quad (58)$$

$$Cu^{2+} + H_2O_2 \rightarrow Cu^{+} + H^{+} + OOH \cdot \quad (59)$$

$$OH \cdot + H_2O_2 \rightarrow H_2O + OOH \cdot \quad (60)$$

$$OH \cdot + Cu^{+} \rightarrow Cu^{2+} + OH^{-} \quad (61)$$

It can be seen that H_2O_2 acts as both as an oxidant and a redundant in Equations (58) and (59) respectively producing hydroxyl radical which are highly oxidative, making it feasible for the process to be effective even at dilute concentrations.

Electroplating

The copper surfaces of the PCB boards were gold plated to avoid high voltage losses of the cell due to corrosion. However, copper and gold tend to undergo solid state diffusion into each other with copper at a faster rate. This process is accelerated by increasing temperature and could cause the gold layer to tarnish and corrode. Plating a barrier layer between the copper and the gold to prevent gold migrating into copper could minimise this effect [62].

Nickel is a commonly used barrier layer, which provides several benefits:

- Serves as an extra backing to the gold for extra hardness.
- Provides an effective diffusion barrier layer between gold and copper.
- Provides a finish that is heat and corrosion resistant, environmentally stable and durable.

The process of gold deposition is explained and illustrated in Figure (65) in the appendix.

4. Experimental

Multilayer bonding and electroplating of PCBs were carried out to obtain the desired thickness of flow field plates and to gold plate the copper layer of the PCBs to prevent passive corrosion of the cell anode. Executions of these processes are elaborated along with design and construction of cell designs that allow optical access and CDD measurements. Furthermore, different experimental set ups employed for each cell design and the performance of engineering and diagnostic measurements at room temperature (20 °C) and atmospheric pressure (1 atm) are discussed in this chapter.

4.1. Multilayer Bonding of PCBs

Firstly, PCBs were treated in ferric chloride solution for 20 minutes to etch off the copper layer. The ferric chloride solution was prepared by dissolving 250 g of ferric chloride pellets from RS Components in 500 ml of warm water. The etched plates were machined with the desired flow designs and then hot pressed with another PCB using a Carver 4122CE hot press. The pre-preg material used for bonding was No-Flo® FR406NF from Isola, which gives minimum resin flow. A layer of pre-preg material was placed in between each of the PCBs and the layers were then covered in aluminium foil. It was carefully placed between the hot press plates that were pre-heated to a temperature of 60 °C using temperature controllers. A pressure of 37 psi was applied to the PCB stack for 10 minutes. The temperature was then raised and maintained at 170 °C over the next 30 minutes.

The applied pressure on the hot press was calculated using Equation (62) [145] as the indicated pressure on the hot press is the pressure on the hydraulic ram and not that applied on the PCBs.

$$Pressure = \frac{pressure\ to\ be\ applied\ to\ PCBs \times area\ to\ be\ bonded}{cross\ sectional\ area\ of\ ramp} \quad (62)$$

The area of the PCB plate was 160 cm^2 (24.8 $inch^2$) and of the ram was 900 cm^2 (140 $inch^2$). Therefore, the applied pressure on the PCB was calculated to be 208 psi. The pressure applied on the ram was 37 psi.

The multilayer PCB plates were then cooled at a temperature of 80 °C in an oven for 10 minutes to reduce the thermal shock, followed by room temperature cooling for another 30 minutes.

4.2. Electrolytic Plating

The procedure followed for electrolytic plating of the copper layer of PCB is described below. In order, to obtain a stable even layer of gold, the copper layer was initially pre-treated and cleaned to prevent any contamination of the copper surface. It was then plated with a layer of nickel followed by a layer of gold.

Copper Surface Pre-Treatment

The copper surfaces of the PCB plates were pre-treated using an ultrasonic bath. The solution used for ultrasonic cleaning was made up of 3 wt% H_2O_2 and 1 M H_2SO_4 solutions in a 4 : 1 ratio. The PCB plates were immersed in the solution and placed in an ultrasonic bath for 60 s. the copper surfaces were then cleaned with DI water and dried in an oven.

Electrolytic Cleaning

A three compartment electroplating bath each for electrolytic cleaning, nickel plating and gold plating as shown in Figure 21, was employed to perform plating of

the copper surfaces of PCBs. The pre-treated PCB material was initially immersed in the cleaning solution made up of 52.6 g of cleaning salts (in 1 L of DI water) from Balco Engineering, for 30 s at 50 °C. A stainless steel anode and a voltage of 4 V were used for this process.

Nickel Electroplating

After electrolytic cleaning, the PCBs were cleaned with DI water and immersed in the nickel plating solution to deposit a nickel layer on copper. The solution was prepared by adding boric acid and nickel chloride to a 65 wt% nickel sulphamate ($Ni[SO_3NH_2]_2.4H_2O$) solution in quantities as shown in Table 3 [147].

Table 3: Makeup of nickel plating solution.

Nimate Nickel Sulphamate	200 ml L^{-1}
Nickel Clhloride	25 g L^{-1}
Boric Acid	35 g L^{-1}

The electroplating was carried out using a stainless steel electrode at 50 °C and a voltage of 3.5 V for 20 minutes while bubbling nitrogen through the solution to rid the copper surface of bubbles. A nickel layer of 10 – 15 µm was obtained.

Gold Electroplating

The nickel-plated PCBs were washed again with DI water before immersing them in an Oresene 999 23.9 ct acid gold plating solution. Gold plating was also carried out at 50 °C and at 4 V for 15 minutes using a platinised titanium mesh counter electrode to obtain an uniform layer of gold coating of about 3 – 5 µm [148].

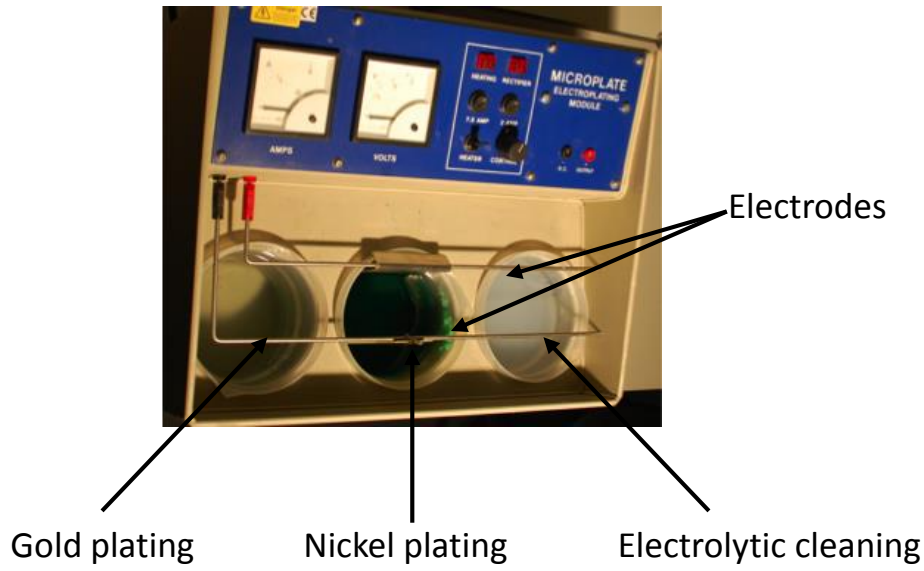

Figure 21: Electroplating bath used for electrolytic cleaning, nickel plating and gold plating.

4.3. Rig Development

The common rig design employed for all the testing of the cell was a combination of the following components and is illustrated in Figure 22:

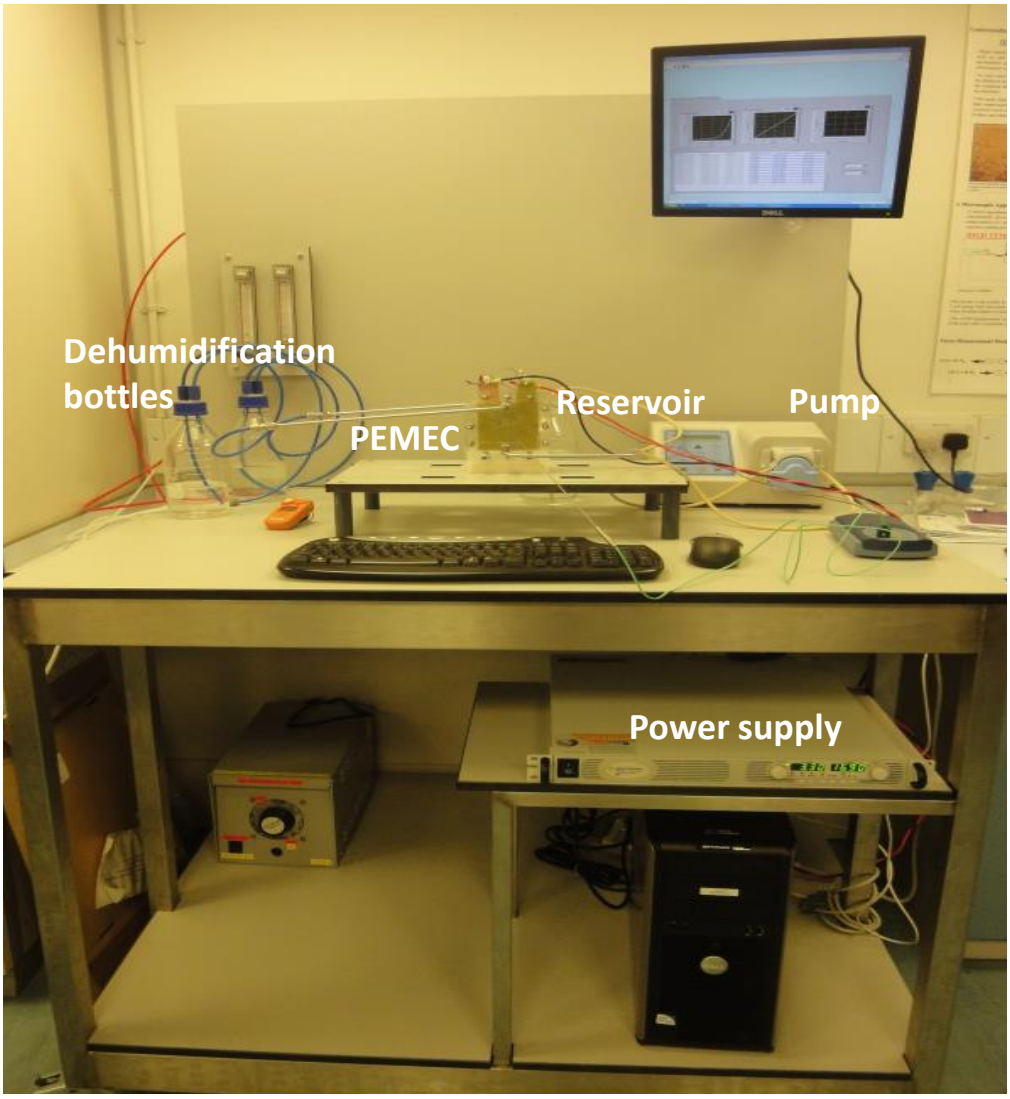

Figure 22: Caption of the common rig setup.

The water reservoir was filled with DI water (18 MΩ cm purity) at room temperature (20 °C) and was connected to a pump to provide feed water to the PEMWE. The water was circulated using a Verderflex programmable peristaltic pump capable of producing flow rates from 0.8 – 1312 ml min^{-1} at angular velocities 10 - 250 rpm depending on the tube diameter used (0.8 – 8.0 mm). For the purpose of this project a 0.8 mm diameter tube was used. Hydrogen and oxygen gases produced were sent to dehumidification bottles that were filled with

DI water. The cell was connected to the water reservoir and the dehumidification bottles using 316 stainless steel pipes and nylon tubing.

4.3.1. Software Control

A general control system for the rig was developed in LabVIEW (National instruments, LabVIEW 2009). It was interfaced with the power supply and allowed the system variables, voltage and current to be controlled. It collects and stores data that can be viewed in an easy to read format.

The LabVIEW system comprised of a front panel and a block diagram as shown in Figures 66 - 68 in the appendix. The front panel displays the values of the variables in real time and the data collected from the system. The block diagram connects different function nodes by 'wires' that execute variables when the input data is available.

4.4. Lab Scale Test Cell

A commercially available single cell system with a reference electrode was employed to explore the effect of feed water flow rate on the voltage-current properties of the cell. EIS measurements were performed on the cell at different operating potentials and different water flow rates to analyse the findings further.

4.4.1. PEM Cell Setup and Test Rig

Electrochemical measurements were made on a 25 cm^2 cell (Fuel Cell Technologies, USA). The anode bipolar plate was made from a Ti plate with a single channel flow-field containing channels 2.5 mm wide and 3.0 mm deep. The cathode bipolar plate was a graphite plate with a triple serpentine flow-field, integrated Pt reference electrode and channels 1.0 mm wide and deep. The MEA was provided by Proton OnSite, (CT, USA) and comprised a Nafion 117 membrane and a 40–60 µm thick layer of Pt catalyst on either side. This was a baseline MEA as it is realised that Pt is not the most suitable catalyst for the OER. The anode GDL was a combination of a platinised porous Ti sheet and a mesh, Toray carbon (TGP_H_120) paper was used as the cathode GDL.

Figure 23 shows the testing arrangement used. The reservoir was filled with 18 MΩ cm DI water at room temperature (20 °C), which was fed to the cell at the required flow rate by the use of a programmable peristaltic pump (AU UPC EZ, Verderflex, UK). A thermocouple was positioned at the centre of the Ti plate (anode side) to measure the cell temperature. Oxygen and hydrogen gases produced at the anode and the cathode respectively were sent through dehumidification bottles before going to extraction. Electrochemical measurements were made using an Iviumstat.XRi high current potentiostat, along with an Iviumboost, (Ivium, Eindhoven, NL).

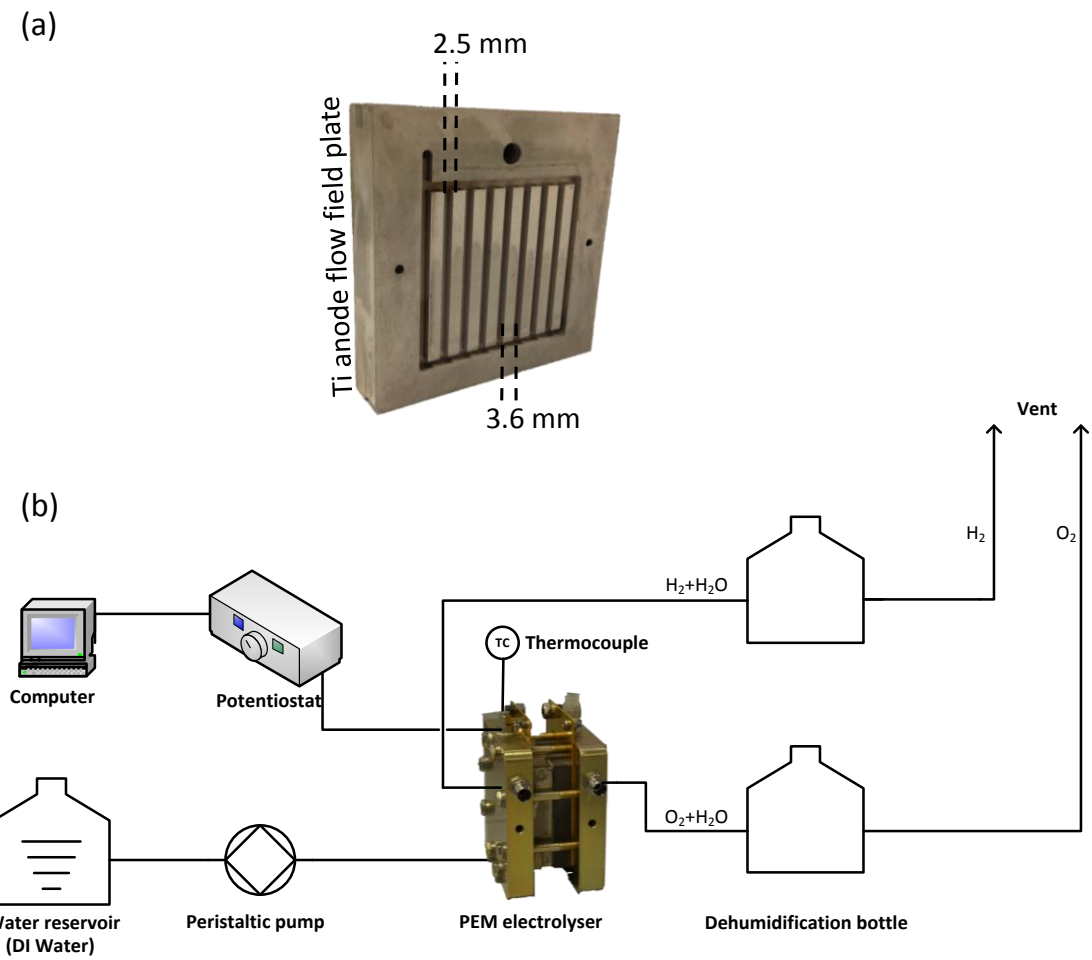

Figure 23: (a) Flow field pattern and channel and channel support dimensions of the anode flow field plate; (b) P&ID of the test bench for electrochemical measurements of the lab scale test cell.

4.4.2. Linear Voltage-Current Measurements

Voltage-current measurements were made by using a linear galvanostatic sweep up to 20 A with a step current of 0.1 A at a scan rate of 0.015 A s^{-1}. Water flow rates of 1 ml min^{-1}, 5 ml min^{-1}, 10 ml min^{-1}, 15 ml min^{-1} and 20 ml min^{-1} at room temperature (20 °C) and pressure (1 atm) were supplied. The cell temperature was monitored at the start and end of each linear sweep.

4.4.3. Electrochemical Impedance Spectroscopy (EIS) Measurements

The measurements were performed in a constant potential mode in a frequency range between 10 kHz – 0.1 Hz by frequency sweeping in single-sine mode with an amplitude of 10 mV_{rms} and 5 frequencies per decade. The measurements were made relative to the integrated reference in the cathode and the anode was set as the working electrode. Impedance spectra were obtained at different operating potentials and water flow rates, which were then fitted to an equivalent circuit.

4.5. Optical Visualisation Cell

An electrolyser cell with circular active area, parallel flow channels and transparent end plates was designed and constructed to gain optical access. Basic engineering measurements, EIS measurements and optical observations were made on the cell at different flow rates of water (at 20 °C).

4.5.1. Cell Development

The PEM electrolysis cell utilised for electrochemical measurements consisted of a 28 cm^2 circular MEA (Proton OnSite, CT, USA). The MEA comprised a Nafion 117 membrane and a layer of platinum catalyst on either side of it. It was sandwiched between a titanium mesh and carbon paper that acted as anode and cathode GDL materials respectively. The MEA and the GDLs were held together by anode and cathode flow field plates that were designed and developed with the aid of CAD / CAM software (Rhino 4.0) and a CNC machine (Roland MDX 40). A flow field design was machined on both anode and cathode flow field plates as shown in

Figure 24. The cathode flow field was made using a 2.0 mm thick graphite block and the anode flow field plate was developed using a 1.6 mm thick PCB material, which consists of an FR4 board with a 35 µm thick copper layer. The flow channel and land width of both anode and cathode flow field plates were set to 2.5 mm. The depths of the anode and cathode channels were set to 2.5 and 1.5 mm respectively, as shown in Figure 24. Therefore, in order to obtain 2.5 mm deep flow channels, a three layer PCB board configuration was employed. Each of the layers was machined with the relevant design and hot pressed together with no flow pre-preg ('pre-impregnated' composite fibres) to obtain the final flow field design. Further, in order to avoid degradation, the copper layer of the PCB plate was electroplated with a 12 µm nickel layer and finally a 5 µm gold layer. A 0.38 mm thick silicon gasket material was used to prevent leakage of reactants and products.

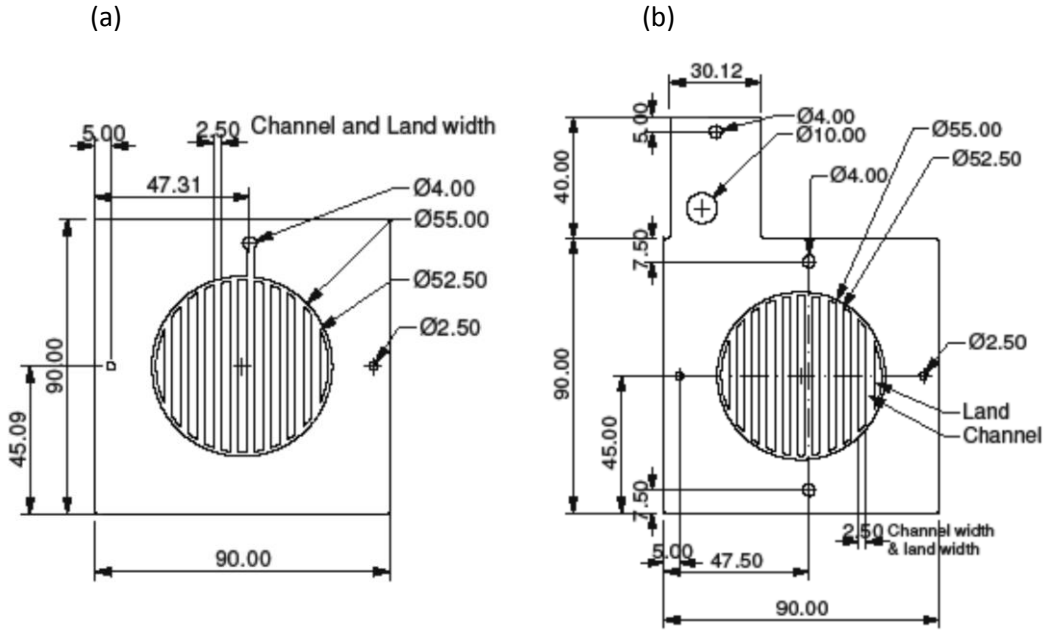

Figure 24: Design and dimensions of the (a) cathode and (b) anode flow field plates.

The current was collected through the PCB flow field plate on the anode side and an additional PCB plate was used on the cathode side for current collection. End plates made of 20 mm thick clear Perspex were used to gain optical access. The final cell configuration can be seen in Figure 25.

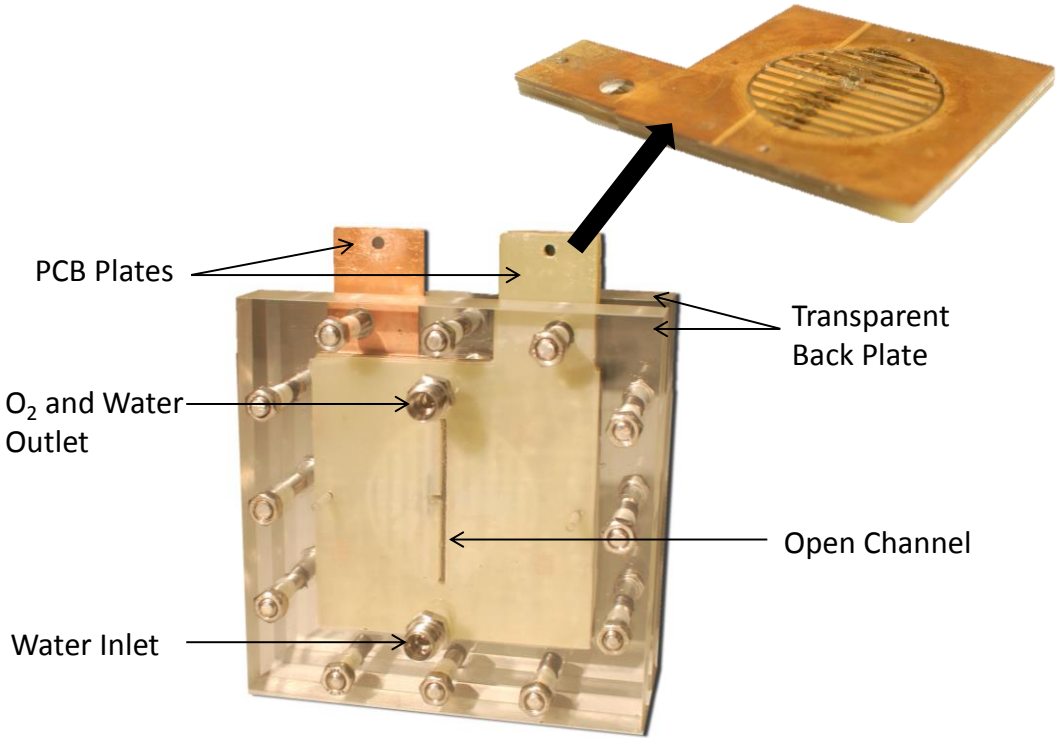

Figure 25: The assembly of end plates, flow field plates, current collectors of a PEMWE and the flow field design on the anode plate.

4.5.2. Test Rig

A piping and instrumentation diagram (P&ID) diagram of the test bench used for electrochemical measurements of the PEM electrolysis cell is shown in Figure 26. The reservoir was filled with 18 MΩ cm DI water at room temperature, which was fed to the cell at a required flow rate by the use of a programmable peristaltic pump. Oxygen and hydrogen gases produced at the anode and the cathode

respectively were sent through dehumidification bottles and the hydrogen gas stream was connected to a gas flow calibrator (Gilibrator-2, Gilian, UK) to record the flow rate of hydrogen gas. A network of thermocouples was used to evaluate the temperature variation of the cell when in operation. Electrochemical measurements were made using an Iviumstat.XRi high current potentiostat, A11700 along with an Iviumboost, IB7108 (Alvatek Ltd, UK).

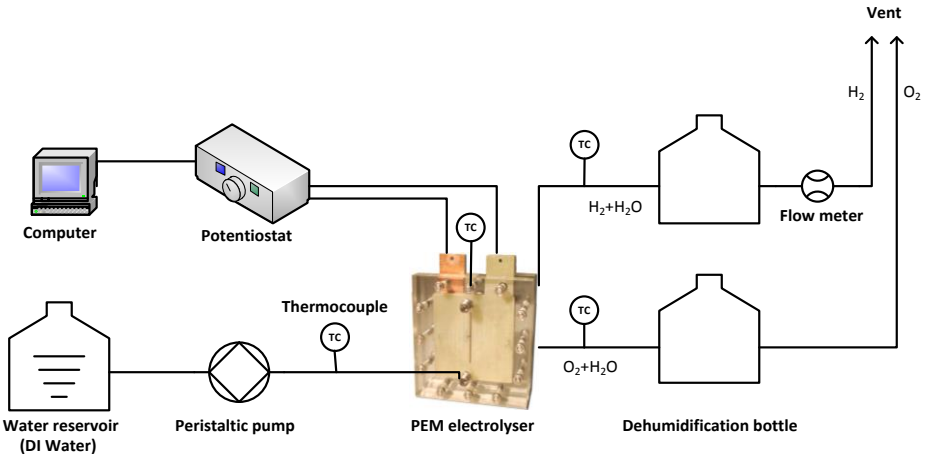

Figure 26: P&ID diagram of the test bench employed for engineering and electrochemical measurements of the optical cell showing thermocouple locations.

4.5.3. Polarisation Measurements

Polarisation (current – voltage) measurements on the cell were made by using the linear galvanostatic sweep option on the potentiostat and by setting the start and the end current values to 0 and 28 A, respectively. The step current was set at 3.3 mA and the scan rate at 3.3 mA s^{-1}. Current sweeps were performed at feed water flow rates of 1 ml min^{-1}, 5 ml min^{-1} and 10 ml min^{-1} at room temperature (20 °C) and pressure (1 atm). Note that regardless of the flow rate or current density used, a sufficient amount of water is always within the cell so that all of the MEA

remains hydrated. This is done by ensuring there is a head of water above the cell leading to the dehumidification bottle.

4.5.4. Electrochemical Impedance Spectroscopy (EIS) Measurements

EIS measurements were performed in a constant potential mode in a frequency range between 100 kHz – 0.1 Hz by frequency sweeping in the single sine mode with amplitude of 10 mV_{rms} and 5 frequencies per decade. The cathode of the PEM cell was used as the reference electrode and the anode was used as the working electrode. Impedance spectra were obtained at different operating potentials at different feed water flow rates and were fitted to an equivalent circuit.

4.5.5. Thermal Imaging

Thermal imaging measurements on the electrolysis cell were carried out using a FLIR SCS5000MB camera which was calibrated for the temperature range 15-100 °C. A 27 mm (F/3) lens was used for the imaging process and the images were recorded using commercially available software (FLIR ResearchIR, FLIR Systems, Croissy-Beaubourg, France). The images were recorded at a frequency of 25 Hz with a spatial resolution of ~0.1 mm. Thermal imaging was carried out on the PEM cell operating at conditions described in Section 4.5.3 and a feed water flow rate of 1 ml min^{-1} was selected for these measurements. Images were obtained at selected current densities to show the variation of temperature across the cell. Figure 27 shows the side face of the PEM cell with P_1-P_6 indicating the points at which discrete temperature measurements were recorded.

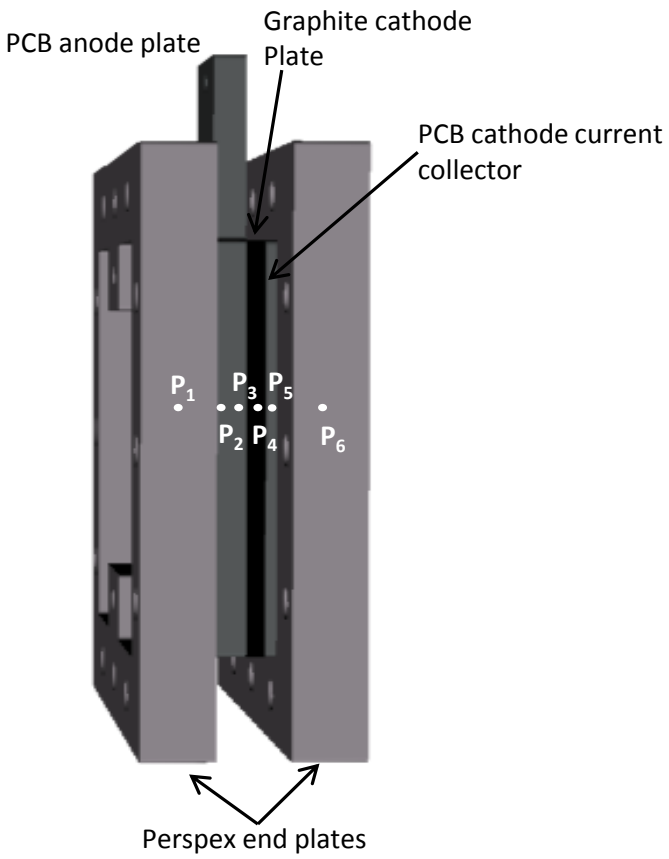

Figure 27: Side face of the assembled PEM cell with the key components and the points at which the temperature variation was analysed.

4.5.6. Visualisation of Bubble Formation

Figure 25 shows the transparent cell used to gain optical access to the anode chamber through an open channel. Images of the bubbles formed and their flow patterns along the middle channel were viewed using a high speed video system (Photron SA-5, Photron, USA) and a Solarc® light source was used for illumination. Images were obtained at a frame rate of 7000 fps and at a resolution of 1024 × 1024. The images were digitally evaluated using Phantom Camera Control (PCC, version v2.14.727.0.) software.

4.6. Segmented Cell

An optical cell was designed and constructed to perform CDD measurements along an electrolyser channel. A Pt/Ru MEA with 8 segments was fabricated to perform these measurements. Voltage-current measurements were made at each segment and the coexistence of gas and liquid in the flow channel was observed through a high speed camera.

4.6.1. Synthesis of Electrocatalyst Ink

The Pt-Ru ink was prepared using a commercial Pt:Ru 50:50 atom% black powder from Alfa Aesar, UK. The ink was composed of aqueous dispersion of the catalyst, 40% Nafion solution and 18 MΩ cm DI water (Millipore Milli-Q® system); the resulting ink was sonicated for 2 h.

4.6.2. Preparation of Catalyst Coated Membranes (CCM)

Two sheets of untreated Toray carbon paper, each with an area of 5.1 cm^2 (0.6 cm × 8.5 cm), were cut and separated into 8 segments using 0.1 cm strips of Kapton® tape. The top and bottom segments have an area of 0.72 cm^2 (0.6 cm × 1.20 cm) and the rest of the segments have an area of 0.54 cm^2 (0.6 cm × 0.9 cm) each.

The brushing technique [25] was used to deposit the catalyst ink on the carbon paper followed by application of the decal method [149] to prepare the CCMs. The carbon sheets were painted with the catalyst ink after sonication and dried at 140 °C for 30 min. The strips of Kapton® tape were peeled off and the coated carbon paper was carefully weighed. The anode and cathode loadings were targeted to be 3.0 mg cm^{-2}. The painted carbon sheets were then sandwiched on both sides of a 33 cm^2 (3 cm × 11 cm) Nafion® 117 membrane and hot-pressed at 500 psi pressure

and 120 °C for 4 min. The carbon papers on either side of the MEA composed were carefully peeled off and weighed again to calculate the exact amount of catalyst transferred to the membrane. Finally, the CCM prepared was immersed in 18 MΩ cm DI water to attain complete hydration. The membrane configuration and the dimensions of the segments are shown in Figure 28 (a).

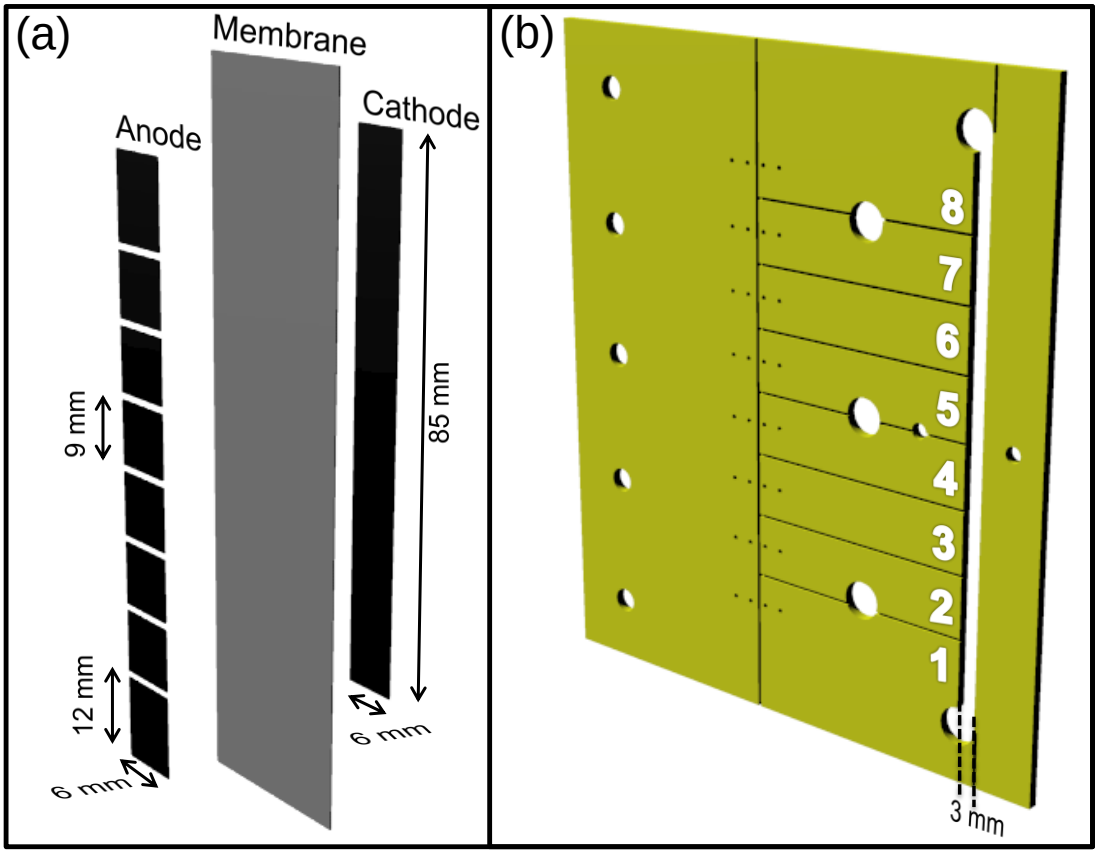

Figure 28: (a) Distended image of the CCM showing catalyst layer dimensions and (b) configuration of the segmented PCB board.

4.6.3. Design of PEMWE Test Cell

The anode and cathode flow fields were machined out of a 1.6 cm thick PCB board using a CNC machine (Roland MDX 40). Each plate consisted of a single channel (0.3 cm × 8.5 cm). As shown in Figure 28 (b), the anode plate was separated into 8 segments. Shunt resistors with 2 mΩ resistance were connected to each segment of the anode. The copper layers (35 μm thick) of both the anode and cathode boards were electroplated with a 0.25 μm gold layer to avoid corrosion and to reduce contact resistance.

Figure 29 (a) shows an exploded view of the electrolyser cell showing the components used and their assembly. A sheet of untreated (no Teflon content) Toray carbon paper (TGP_H_120) was used as the cathode GDL and the anode side was left unsupported (no GDL) in order to prevent lateral conduction of current between individual segments of electrode and to gain optical access to the electrode surface. The MEA and the cathode GDL were positioned between gasket material and flow field plates (that also acted as the current collectors) in such a way that one half of the MEA (0.3 cm × 8.5 cm strip) was in contact with the plates and the other half was aligned within the flow channel. The cell was held together using end plates made of 2 mm thick Perspex (with 3 mm wide channels) that had 12 bolts going through them which were tightened to a torque of 1.2 Nm, as shown in Figure 29 (b).

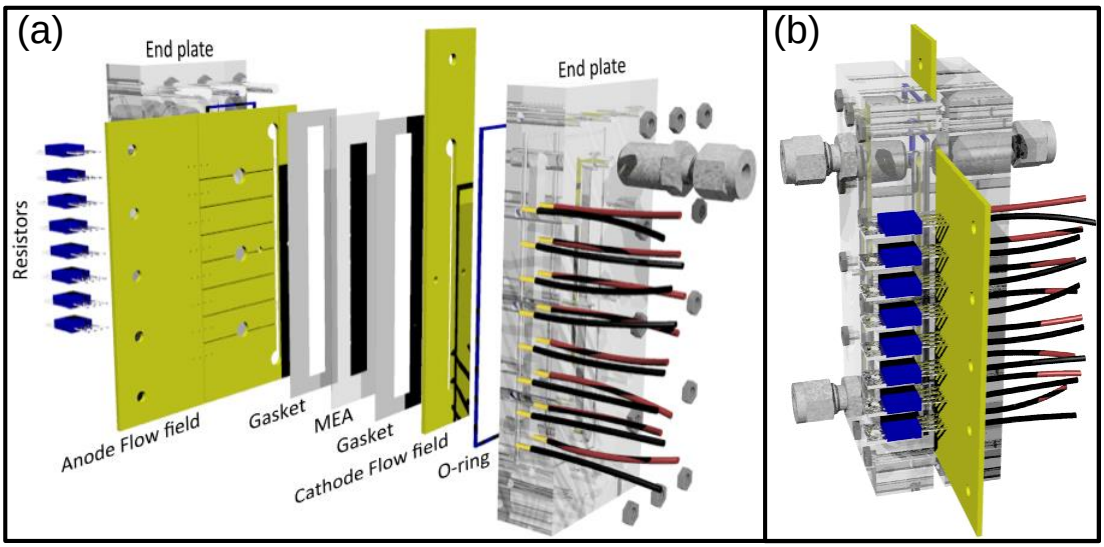

Figure 29: (a) An exploded view of the cell illustrating the cell components and their assembly. (b) Illustration of an assembled electrolyser cell used for current mapping measurements.

4.6.4. Measurement System and Procedure

A schematic of the testing arrangement is shown in Figure 30. DI water (18 MΩ cm) from the reservoir was pumped through the cell using a programmable peristaltic pump. The gasses produced were sent through dehumidification bottles and then to vent. The voltage across each of the shunt resistors on the anode flow-field plate was measures using an 18–bit data acquisition board (DAQ) from National Instruments, UK to calculate the current generated from each segment. The DAQ board was interfaced with LabVIEW program that displayed the current across each segment. In the appendix, Figure 69 and 70 show the interface panel used during experimentation and a block diagram of the virtual interface (VI) network. The main anode and cathode flow-field plates were connected to an Iviumstat.XRi high current potentiostat, A11700 (Alvatek Ltd, UK).

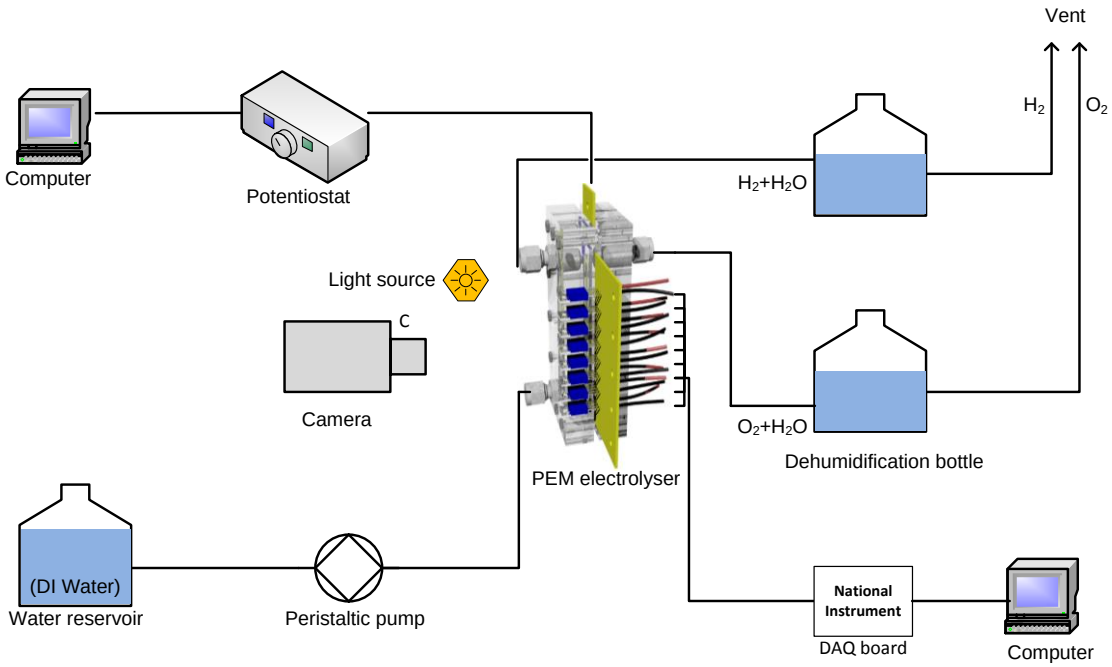

Figure 30: Illustration of testing arrangement for current mapping and optical visualisation along electrolyser channel of the segmented cell.

4.6.5. Polarisation and CDD Measurements

Whole-cell polarisation measurements were performed using the linear galvanostatic sweep option on the potentiostat (scan rate at 10 mA s^{-1}, step current 50 mA). The measurements were carried out at a water flow rate of 1 ml min^{-1} at which the ratio of circulating water to the amount of water required to service the process, ζ, has a value greater than 1 ($\zeta > 1$) throughout all operating conditions [150]. Therefore, this flow rate is sufficient to keep the membrane hydrated throughout the electrolysis process.

The electrolyser cell was polarised to a range of operating potentials at different water flow rates (1, 3 and 5 ml min^{-1}) using the chronoamperometry mode on the potentiostat. The current densities for each current collector were inferred by measuring voltage drop across each of the shunt resistors.

4.6.6. Optical Visualisation Measurements

Images of the liquid and gas flow patterns along the channel and gas bubble formation were viewed using a high speed video system (Photron SA-5) with Solarc® light source for illumination. Images were obtained at a frame rate of 2000 fps and at a resolution of 1024 × 1024. The images were digitally evaluated using Phantom Camera Control (PCC, version v2.14.727.0.) software.

5. Results

A mathematical model is developed in this chapter which is validated using experimental data. Furthermore, results obtained from engineering and diagnostic measurements made on cell prototypes are discussed in detail in this chapter.

5.1. Electrochemical Model

As discussed in the literature review (chapter 2) of this thesis, it is apparent that PEMWE technology has tremendous scope for further development; mainly in the materials of construction sector that will reduce production costs to meet market requirements and in system performance in order to increase operational efficiencies. Therefore, in order to address these matters it is important to have a good understanding of the electrochemical properties and the behaviour of an electrolyser.

PEMWE modeling is a useful tool to understand the fundamental nature of device operation depending on system design and operating conditions. A model not only provides a framework to analyse the characteristics of current and voltage of an electrolyser but it also supplies the values of internal variables which are difficult to measure, such as the exchange current densities.

Models have been developed that describe the current-potential characteristics of PEMWEs [32, 80, 151], determine control strategy [152, 153] and understand the effect of operating parameters on the performance [67, 129] and the effect of temperature on the cell performance [154] . Furthermore, models that look at the integration with renewable energy sources are presented in literature [155]. Electrical equivalent circuit models [156, 157] and thermal models have also been developed [155].

This study presents a simple steady-state electrochemical model focusing on activation and ohmic overpotentials to obtain a relationship between the operating voltage of the cell and the current which will be validated using experimental results obtained from a single cell PEMWE.

5.1.1. Assumptions

The model presented here is based on the following simplifying assumptions:

- The PEMWE operates under steady-state conditions.
- All physical processes are taking place at a constant temperature (room temperature, 20 °C) and pressure (atmospheric pressure, 1 atm). i.e ohmic heating in the current collector plates is neglected.
- Gases produced at the anode and the cathode are considered to be ideal gases.
- 100% Faradaic efficiency in the system.
- The current density is used as the independent variable, whereas other operating conditions such as temperature and pressure are kept constant, as mentioned above.
- The current across the cell is assumed to be uniformly distributed:

$$I = iA \tag{63}$$

where i is the current density and A is the active area.

- The membrane is assumed to be fully hydrated.
- No cross-over of gases produced.

5.1.2. Mass Balances

The mass balance over a controlled volume can be expressed using the mass flow rates ($\dot{m}$) of the feed water and the products, hydrogen and oxygen. Figure 31 illustrates the mass flow in a PEMWE, where $\dot{m}_{H_2O,in}$, $\dot{m}_{H_2O,out,an}$ and $\dot{m}_{H_2O,out,cat}$ are the inlet and outlet mass flow rates of water at the anode and the outlet mass flow rate of water at the cathode respectively. $\dot{m}_{H_2}$ and $\dot{m}_{O_2}$ are the mass flow rates of hydrogen and oxygen produced at the cathode and the anode. $\dot{m}_{H_2O,dd}$ and $\dot{m}_{H_2O,eo}$ are the mass flow rate of water flowing from the anode to the cathode due to the concentration gradient and the electro-osmotic drag. $\dot{m}_{H_2O,con}$ is the mass flow rate of water consumed by the electrochemical reaction.

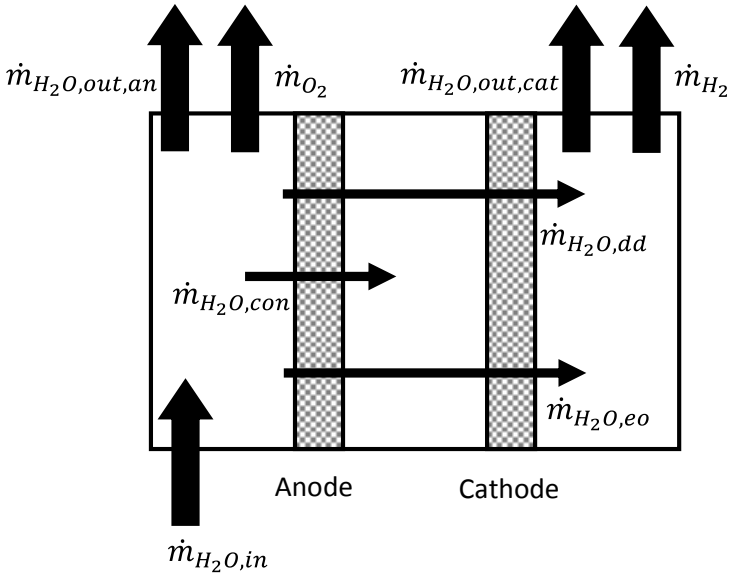

Figure 31: Illustration summarising mass flow inside a PEMEC.

The formal definition for material balances from mass conservation in a system can be written as:

$$Input + Generation - Output - Consumption = Accumulation \quad (64)$$

Therefore, a simple mass balance can be performed as described below.

5.1.2.1. Anode Chamber

As shown in Figure 31, the water coming out from the anode chamber is the difference between the water fed at the anode, water being consumed to produce oxygen and the amount of water that flows through the membrane:

$$\dot{m}_{H_2O,out,an} = \dot{m}_{H_2O,in} - \dot{m}_{H_2O,m} - \dot{m}_{H_2O,cons} \quad (65)$$

where $\dot{m}_{H_2O,m}$ is the mass flow rate of water through the membrane.

5.1.2.2. Cathode Chamber

The amount of water flowing out from the cathode chamber is equal to the amount that flows through the membrane, as water is not consumed at the cathode.

$$\dot{m}_{H_2O,out,cat} = \dot{m}_{H_2O,m} \quad (66)$$

The water flux through the membrane is governed by three mechanisms: electro-osmotic drag from the anode to cathode, diffusion driven by concentration gradient from the anode to cathode and convection if a pressure gradient is present [158]. In this study, convection in not considered as the pressure is

assumed to be at a constant value of 1 atm at the anode and the cathode. The direction of water flux across the membrane is shown in Figure 31 and can be written as [159]:

$$\dot{m}_{H_2O,m} = \dot{m}_{H_2O,dd} + \dot{m}_{H_2O,eo} \quad (67)$$

Molar flow rate of species i can be related to its mass flow rate as:

$$\dot{N}_i = \frac{\dot{m}_i}{mw_i} \quad (68)$$

where $\dot{N}_i$ is the molar flow rate of component i and mw_i is the molecular weight of component i.

The molar flow rates of the hydrogen and oxygen produced and the water consumed can be related to the current applied to the cell by Faraday's law as illustrated in Equations (20)-(22) in the electrochemical kinetics section (2.1.6).

5.1.2.3. Diffusion Transport

The water diffusion through the membrane is due to the concentration gradient of water across the membrane that favours the water flow from the anode to the cathode as the anode is constantly flooded due to fluent water from the pump. A large concentration gradient can be expected when the electrolyser starts operation as the cathode side is initially dry. The diffusion transport can be evaluated by the following equation [128]:

$$\dot{N}_{H_2O,dd} = \frac{AD_{eff}}{\delta_m}\left(C_{H_2O,an} - C_{H_2O,cat}\right) \quad (69)$$

where D_{eff} is the effective water diffusion coefficient in the membrane, δ_m is the membrane thickness and $C_{H_2O,an}$ and $C_{H_2O,cat}$ represent the water concentrations at the two sides of the membrane.

The effective diffusion coefficient for water transport inside the GDL and the membrane can be expressed using the Bruggeman equation as below [157, 160, 161]:

$$D_{eff} = \varepsilon^{1.5} D_w \tag{70}$$

where D_w is the diffusion coefficient of water and can be evaluated to have a value of 1.28 × 10^{-10} m^2 s^{-1} through expressions reported by Springer *et al.* [162] and ε is the porosity of the electrode and a commonly used value of ε = 0.3 is used for the calculations [163].

The concentration gradient of water between the electrodes is the driving force in diffusion through the membrane and is illustrated in Figure 32. The concentration of water on either side of the membrane can be expressed as a function of water content as shown in the following expressions [164]:

$$C_{H_2O,an} = \frac{\rho_{m,dry}}{M_{m,dry}} \lambda_{an}, \quad C_{H_2O,cat} = \frac{\rho_{m,dry}}{M_{m,dry}} \lambda_{cat} \tag{71}$$

where $\rho_{m,dry}$ is the density of the dry membrane, $M_{m,dry}$ is the equivalent weight of a dry membrane and λ_{an} and λ_{cat} represent the water content on both sides of the membrane. The following expression has been formulated based on studies performed by Zawodzinski *et al*. [165] for the water content of a Nafion 117 membrane [162, 164]:

$$\lambda = 0.043 + 17.81 a_{H_2O} - 39.85 a_{H_2O}^2 + 36 a_{H_2O}^3, 0 < a_{H_2O} \leq 1 \tag{72}$$

where a_{H_2O} is the activity of water and can be obtained using the following expression:

$$a_{H_2O} = x_{H_2O} \frac{P}{P_{sat}} \tag{73}$$

where, P_{sat} is the saturation pressure of water and x_{H_2O} is the amount fraction of water given by:

$$x_{H_2O,an} = \frac{\dot{n}_{H_2O,an}}{\dot{n}_{H_2O,an}+\dot{n}_{O_2}}, \quad x_{H_2O,cat} = \frac{\dot{n}_{H_2O,cat}}{\dot{n}_{H_2O,cat}+\dot{n}_{H_2}} \tag{74}$$

The activity of water at the anode can be assumed to have a value close to unity as water is present in bulk compared to the amount of oxygen being produced.

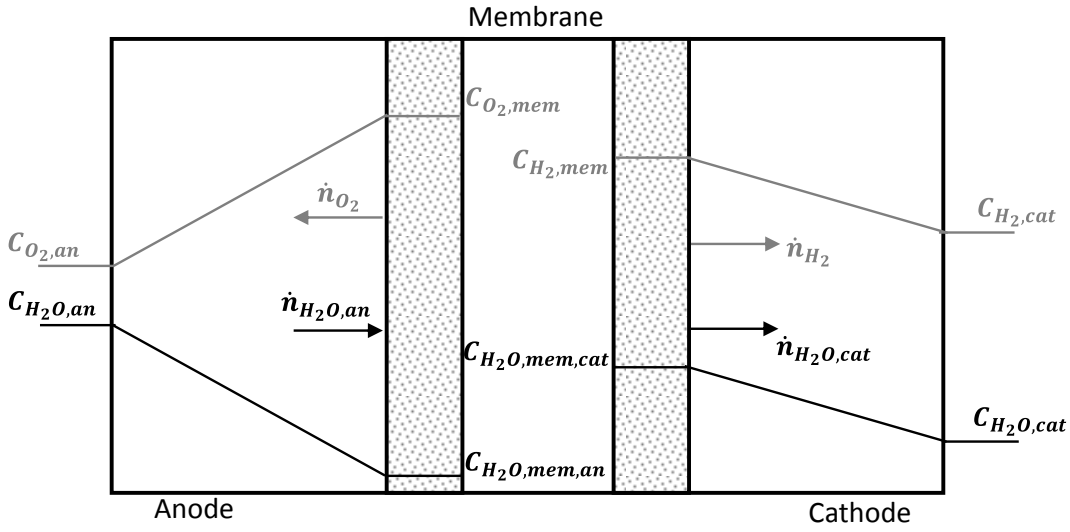

Figure 32: Species concentration inside a PEMEC.

5.1.2.4. Electro-Osmotic Drag

The transport of water from the anode electrode domain to the cathode electrode domain due to the flux of hydrated protons migrating between the electrodes is known as the electro-osmotic drag. Hence, the molar flow can be expressed as [129, 130, 166]:

$$\dot{N}_{H_2O,eo} = n_d \frac{I}{F} \tag{75}$$

where n_d is the electro-osmotic drag coefficient $\left[mol_{H_2O}/mol_{H^+}\right]$.

There are a number of expressions presented in literature to find the electro-osmotic drag coefficient. Onda *et al*. [167] has reported that the electro-osmotic drag coefficient of a MEA fabricated using electroplating is only dependent on the operating temperature as expressed below:

$$n_d = 0.03 + 0.0134T \tag{76}$$

Work done by Ge *et al.* [168] reports that n_d is enhanced by the water content of the membrane and can be expressed as below. The water content of a PEM electrolyser is at a maximum due to the high amounts of water at the anode.

$$n_d = 0.011 + 0.1949\lambda - 0.0139\lambda^2 + 4.060 \times 10^{-4}\lambda^3, \lambda \leq 1.40 \tag{77}$$

5.1.3. Open Circuit Voltage (OCV)

The OCV is the voltage caused by the chemical redox reaction when the net current is zero (*I*=0). As discussed in the thermodynamics section (Section 2.1.4),

the OCV at non-standard conditions can be calculated from the Nernst Equation as illustrated in Equation (7) [13, 153].

Furthermore, the expression derived by LeRoy and Bowen [169] can be used to determine the OCV at atmospheric pressure:

$$E = 1.5184 - 1.5421 \times 10^{-3}T + 9.523 \times 10^{-5}Tln(T) + 9.84 \times 10^{-8}T^2 \quad (78)$$

The practical cell voltage of a PEM electrolyser is higher than the open circuit voltage. This difference is caused by the voltage drops that occur across a cell due to activation, diffusion and ohmic overpotentials (losses). Therefore, the real cell voltage can be written as:

$$E_{cell} = E + \eta_{act} + \eta_{ohm} + \eta_{dd} \quad (79)$$

where η_{act} is the activation overpotential, η_{ohm} is the ohmic overpotential and η_{dd} is the diffusion over potential.

5.1.4. Activation Overpotential

Activation overvoltage represents the electrochemical kinetic behaviour; hence it is a representation of the speed of the reactions taking place at the electrode surface. Therefore, a portion of the voltage applied is lost in transferring the electrons to or from the electrodes. This activation loss (η_{act}) can be deduced from the Butler-Volmer equation [74]:

$$i = i_0 \left[exp\left(\frac{\alpha_{an} nF}{RT}\eta_{act}\right) - exp\left(\frac{-\alpha_{cat} nF}{RT}\eta_{act}\right)\right] \quad (80)$$

where i_0 is the exchange current density, n is the number of electrons transferred and α_{an} and α_{cat} are the charge transfer coefficients for the anodic and cathodic processes.

The charge transfer coefficient is governed by the electron transfer occurring across the electrode-electrolyte interface. Equations (81) and (82) can be used to determine the anode and cathode charge transfer coefficient of a process where the reaction mechanisms are known [82].

$$\alpha_{an} = \frac{n-\gamma}{\nu} - s\beta \quad (81)$$

$$\alpha_{cat} = \frac{\gamma}{\nu} + s\beta \quad (82)$$

where n is the total number of electrons transferred in the overall reaction, γ is the number of electrons transferred before the rate determining step (rds), ν is the number of times the rds occurs for one act of the overall reaction, s is the number of electrons transferred in the rds and β is the symmetric factor.

They can be simplified for a PEM system as follows [170]:

$$\alpha_{an} = (1-\beta)s \quad (83)$$

$$\alpha_{cat} = \beta s \quad (84)$$

Symmetric factor, β is the fraction of potential energy applied to a system that changes the reaction rate. For simplicity, this factor is commonly assumed to be 0.5 [170]. However, values ranging from 0.3 to 0.6 have been obtained from experimental data presented in literature [82]. Values between 0 - 2 have been used for α_{an} and 0 - 1 for α_{cat} in literature [79, 170].

For a system where the activation loss is large (η_{act}> 200 mv), the Butler-Volmer equation can be simplified to Equation (85) [82]:

$$\eta_{act} = \frac{RT}{F}\sinh^{-1}\left(\frac{i}{2i_0}\right) \quad (85)$$

Hence, the activation overvoltage at the anode and the cathode can be written as:

$$\eta_{act} = \frac{RT}{F}\sinh^{-1}\left(\frac{i}{2i_{0,an}}\right) \quad (86)$$

$$\eta_{act} = \frac{RT}{F}\sinh^{-1}\left(\frac{i}{2i_{0,cat}}\right) \quad (87)$$

The exchange current density values have a substantial effect on the activation overpotential and are greatly dependent on the materials and porosity of the electrodes; concentration, distribution and dimensions of the catalyst particles and operating temperature [171]. The exchange current density can be calculated from an Arrhenius-type relation:

$$i_0 = Ae^{-E_A/RT} \quad (88)$$

where A is the pre-exponential factor and E_A is the activation energy.

Typically, $i_{0,an}$ and $i_{0,cat}$ vary in a range between 10^{-3} – 10^{-12} A cm^{-2} and 0.2 – 10^{-3} A cm^{-2} respectively [155, 170, 172-175]. However, experimental values at 20 °C obtained for a HOGEN-40 electrolyser manufactured by Proton Energy systems and published by Biaku *et al.* [154] is used for the cathode exchange current density; $i_{0,cat}$ = 0.287 A cm^{-2} and $i_{0,an}$ = 3.50 × 10^{-3} A cm^{-2} is chosen for the anode exchange current density.

5.1.5. Diffusion Overpotential

Diffusion overvoltage, also known as the concentration overpotential, occurs due to the change in concentration of the reactants at the electrode surfaces when electrolysis is in progress.

In a PEM electrolysis system, as the electrochemical reaction takes place, water needs to be supplied to the electrode-membrane interface, whereas hydrogen and oxygen should be removed from it. Therefore, the mass flows are transported through the porous electrode according to the diffusion phenomena described by Fick's law. If the oxygen and hydrogen produced in an electrolysis system are not removed as fast as they are being produced, there will be an increase in mass transport limitation. This diffusion overvoltage can be estimated using the Nernst equation, as shown below [74, 129]:

$$\eta_{dd} = V_1 - V_0 = \left(E^0 + \frac{RT}{nF} lnC_1\right) - \left(E^0 + \frac{RT}{nF} lnC_0\right) = \frac{RT}{nF} ln \frac{C_1}{C_0} \quad (89)$$

where n is the number of electrons transferred during the reaction and '0' is a working condition taken as reference.

Hence, Equation (89) can be applied to find the diffusion overvoltage at both the anode and the cathode:

$$\eta_{dd,an} = \frac{RT}{4F} ln \frac{C_{O_2,m}}{C_{O_2,0}} \quad (90)$$

$$\eta_{dd,cat} = \frac{RT}{2F} ln \frac{C_{H_2,m}}{C_{H_2,0}} \quad (91)$$

where $C_{O_2,m}$ and $C_{H_2,m}$ represent oxygen and the hydrogen concentrations at the membrane electrode interface, respectively.

Diffusion overvoltage occurs when the current is high enough to hinder the reaction by overpopulating the membrane surface with oxygen gas bubbles and hence slowing down the reaction rate [154]. However, diffusion overvoltage is assumed to be negligible as this work focuses on PEM electrolysers operating at moderate current densities (up to 1 A cm^{-2}).

5.1.6. Ohmic Overpotential

The ohmic overvoltage is caused by the resistance to the flow of electrons by the electrolyte, the electrodes and their various interconnectors. Ohmic overvoltage is linearly proportional to the current and can be expressed as:

$$\eta_{ohm} = R_{cell} I \tag{92}$$

where R_{cell} is the ohmic resistance of the cell.

The magnitude of the ohmic resistance is a combination of the resistances opposed by the electrodes, the plates and the membrane and can be written as:

$$\eta_{ohm} = \left(R_{an} + R_{cat} + R_p + R_m\right) I = \left(R_e + R_p + R_m\right) I$$
$$\eta_{ohm} = \eta_{ohm,e} + \eta_{ohm,p} + \eta_{ohm,m} \tag{93}$$

where R_{an}, R_{cat}, R_p and R_m are resistances of the anode, cathode, bipolar plates and the membrane, and $\eta_{ohm,e}$, $\eta_{ohm,p}$ and $\eta_{ohm,m}$ are the ohmic overpotentials caused by the electrodes, bipolar plates and the membrane respectively.

5.1.6.1. Electrodes and Plates

The voltage losses associated with electron transfer through the electrode and the flow field plate are found by adopting the electric circuit analogy presented by Marr and Li [161] shown in Figure 33. Applying ohms law on the electrode and the flow field plate gives:

$$R = \rho_{eff} \frac{\iota}{A} \tag{94}$$

where ι is the length of the electrons path, A is the cross-section of the conductor and ρ_{eff} is the effective resistivity of the electrode which is given by:

$$\rho_{eff} = \frac{\rho_{bulk}}{(1-\varepsilon)^{3/2}} \tag{95}$$

where ρ_{bulk} and ε are the resistivity and the porosity of the electrode.

Assuming that the total average path length of an electron is $(w_c + w_s)/4$, where w_c and w_s are the width of a channel and channel support respectively. Therefore, the average resistance in the electrode per half flow channel becomes [161]:

$$R_1 = \frac{\rho_{eff}(w_c+w_s)}{4\delta_e L} \tag{96}$$

where δ_e and L are the thickness and the length of the electrode. If the number of channels in the flow field plate is n_{ch} then the total resistance of the electrode becomes:

$$R_e = \frac{\rho_{eff}(w_c+w_s)}{8n_{ch}\delta_e L} \tag{97}$$

R_2 denoted in Figure 33 indicate the resistance caused by the right portion of the flow field plate that is given by:

$$R_2 = \frac{\rho_P h_p}{wL} \tag{98}$$

where ρ_P is the resistivity of the current collection plate, h_p is the distance from the outside border of the plate to the channel surface, W is the width and L is the length of the plate. Similarly, the resistance of each channel support is:

$$R_s = \frac{\rho_P h_c}{w_s L} \tag{99}$$

where h_c is the height of the channel. Considering there are $n_{ch} + 1$ channel supports, the total resistance of the flow-field plate becomes:

$$R_p = \frac{R_s}{n_{ch}+1} + R_2 \tag{100}$$

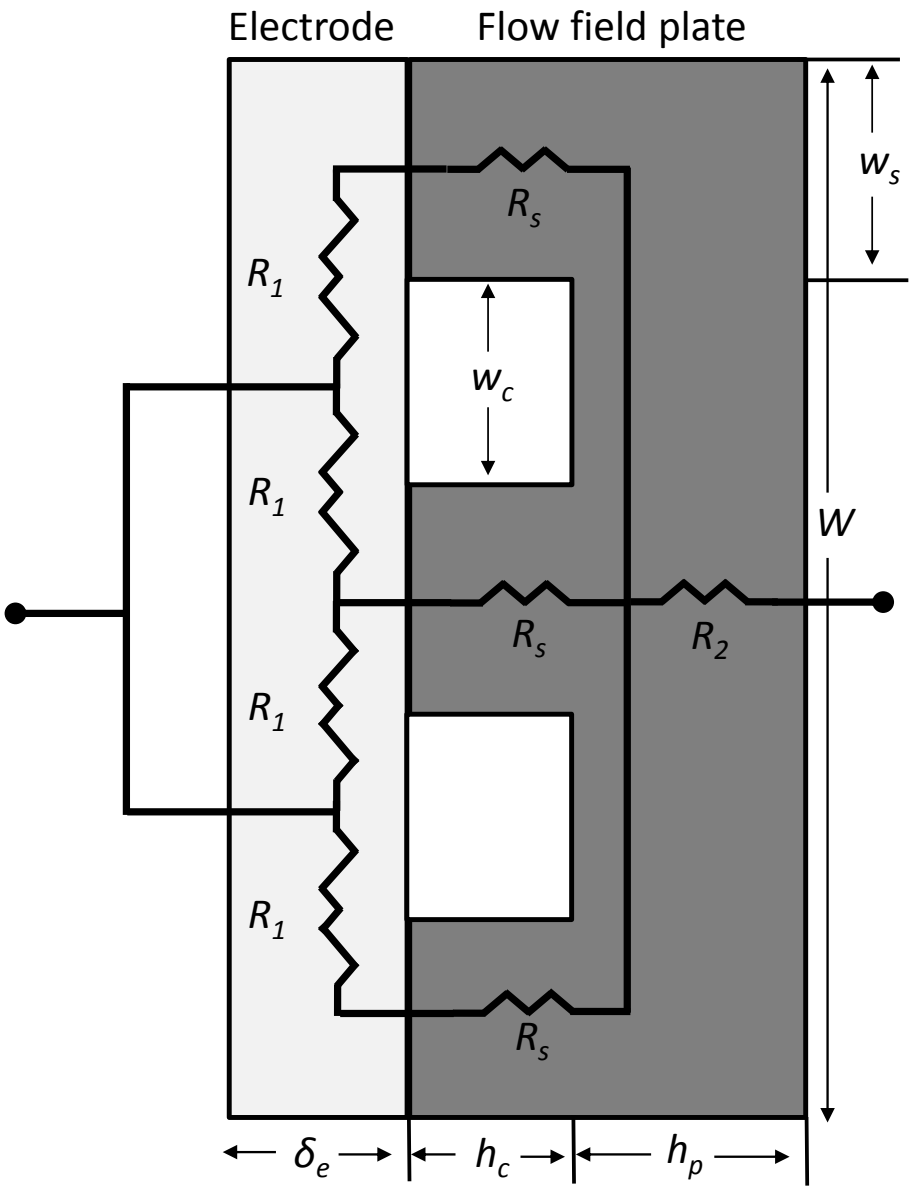

Figure 33: Electrical circuit representation of the resistances of the plates and the electrode in a PEMWE.

5.1.6.2. Membrane

The dominant losses in η_{ohm} are the ionic losses caused by resistance to the ion flow through the membrane. This resistance caused by the membrane can be expressed as shown in Equation (101):

$$\eta_{ohm,m} = \frac{\delta_m}{\sigma_m} i \quad (101)$$

Where σ_m and δ_m are the conductivity and the thickness of the membrane.

A study by Ito *et al*. [176] compares different analysis present in literature on proton conductivity of Nafion membranes. The expression (Equation 102) suggested by Springer *et al*. [162] provides conductivity in terms of water content and the temperature of the membrane. The expression suggested by Bernardi and Verbrugge [160] (Equation 103) gives conductivity as a function of protonic diffusion coefficient and concentration of protons in the membrane and is used in this model. Further studies done by Radev *et al*. [177] suggest a value of 0.094 S cm^{-1} for the proton conductivity of a Nafion 117 membrane at 80 °C and 100% relative humidity.

$$\sigma_m = (0.005139\lambda - 0.00326) exp\left[1268\left(\frac{1}{303} - \frac{1}{T}\right)\right] \quad (102)$$

$$\sigma_m = \frac{F^2 C_{H^+} D_{H^+}}{RT} \quad (103)$$

where λ and T are the water content and temperature of the membrane and C_{H^+} and D_{H^+} are the concentration of H^+ ions and protonic diffusion coefficient in the membrane.

5.1.7. Model Development

A simple electrochemical model was developed to understand the overpotentials associated with PEMWEs operating at room temperature (20 °C) and atmospheric pressure (1 atm). An analysis is carried out to find the sensitivity of the model to estimated parameters.

The model is developed for a PEMWE cell assembled with key components listed in Table 4 and assuming mass transport limitations are negligible in the current density range considered. The physical parameters of the electrolysis cell are listed in Table 5.

The developed model was implemented in MATLAB along with estimated parameter values listed in Table 6 to obtain a theoretical voltage-current relation for the electrolyser.

Table 4: Physical properties of the PEMWE.

Membrane	Nafion 117
Anode/Cathode electrode	Platinum
Anode GDL	Platinum coated titanium porous sheet and a mesh
Cathode GDL	Toray carbon paper
Anode flow field plate	Titanium - parallel flow
Cathode flow field plate	Graphite - triple serpentine

Table 5: Physical parameters of the PEMWE cell.

Temperature, T	293 K
Pressure, P	1.0 atm
Membrane active area, A	25×10^{2} mm^{2}
Membrane thickness, δ_m	0.178 mm
Anode Thickness, δ_{an}	5.0×10^{-2} mm
Cathode thickness, δ_{cat}	5.0×10^{-2} mm
Length of the electrode, L	50 mm
Width of the electrode, W	50 mm
Width of anode channel, $w_{c,an}$	2.5 mm
Width of cathode channel, $w_{c,cat}$	1.0 mm
Width of anode support, $w_{s,an}$	3.6 mm
Width of cathode support, $w_{s,cat}$	1.0 mm
Distance from anode plate edge to the channel surface, $h_{p,an}$	12 mm
Distance from cathode plate edge to the channel surface, $h_{p,cat}$	11.7 mm
Anode channel height, $h_{c,an}$	3.0 mm
Cathode channel height, $h_{c,cat}$	1.0 mm
Number of anode channels, $n_{ch,an}$	9
Number of cathode channels, $n_{ch,cat}$	30
Number of anode supports, $n_{s,an}$	8
Number of cathode supports, $n_{s,cat}$	30

Table 6: Estimated parameter values

Parameter	Value	Unit	Reference
Anode charge transfer coefficient, α_{an}	0.10		[74]
Cathode charge transfer coefficient, α_{cat}	0.90		[74]
Water diffusion coefficient, D_w	1.28×10^{-10}	$m^2\ s^{-1}$	[162]
Porosity of the electrodes, ε	0.30		[163]
Anode exchange current density, $i_{0,an}$	3.50×10^{-3}	$A\ cm^{-2}$	[155, 170, 172-175]
Cathode exchange current density, $i_{0,cat}$	0.29	$A\ cm^{-2}$	[154]
Hydrogen concentration, C_{H^+}	1200	$mol\ m^{-3}$	[160]
Diffusivity of hydrogen, D_{H^+}	4.50×10^{-9}	$m^2\ s^{-1}$	[160]
Electrode resistivity, ρ_{bulk}	9.85×10^{-8}	Ω m	[178]
Anode resistivity, ρ_{an}	47.80×10^{-8}	Ω m	[179]
Cathode resistivity, ρ_{cat}	16.0×10^{-6}	Ω m	[180]
Saturated water vapor pressure P_{sat}	0.47	atm	[160]
Equivalent weight of dry membrane, $M_{m,dry}$	1.10	$kg\ mol^{-1}$	[157, 181]
Density of dry membrane, $\rho_{m,dry}$	2000	$kg\ m^{-3}$	[157, 181]

5.1.8. Theoretical Performance of the PEMWE

Figure 34 shows the theoretical V-I curve obtained from the mathematical model developed. Values of 0.1 and 0.9 were assumed for anode and cathode charge transfer coefficients respectively and the exchange current density of the anode and the cathode were assumed to have values of 3.5×10^{-3} and 0.29 $A\ cm^{-2}$ respectively. A value of 4.5×10^{-9} $m^2\ s^{-1}$ was assumed for D_{H^+} and the temperature and pressure were set to ambient conditions, 20 °C and 1 atm. It was observed that the theoretical polarisation curve agrees with data presented in literature [80].

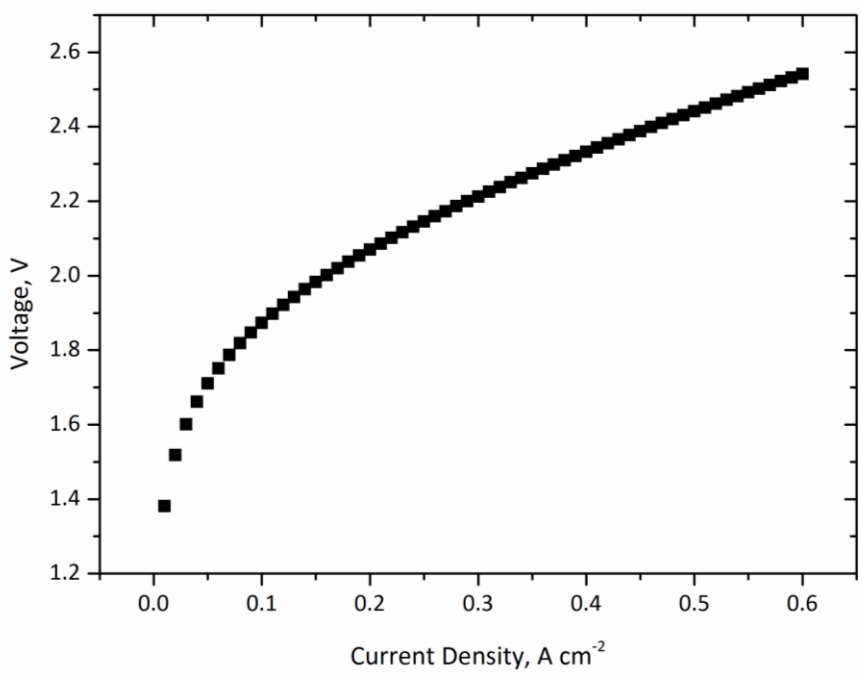

Figure 34: Theoretical polarisation curve obtained for a PEMWEC operating at ambient conditions (T = 20 °C, P = 1 atm).

Figure 35 shows the contribution of each of the overpotentials towards the overall performance of the cell. It can be seen that activation overpotential dominates the output voltage of the cell. However, cathode overpotential is relatively small due to fast kinetics of HER; therefore, the cell potential is dominated by the anode activation overpotential due its slow kinetics. It can be seen that the ohmic overpotential increases linearly with current density but is much lower than $\eta_{act,an}$; hence, the relatively high operating potential of the cell can be explained by the high activation overpotential of the platinum electrode.

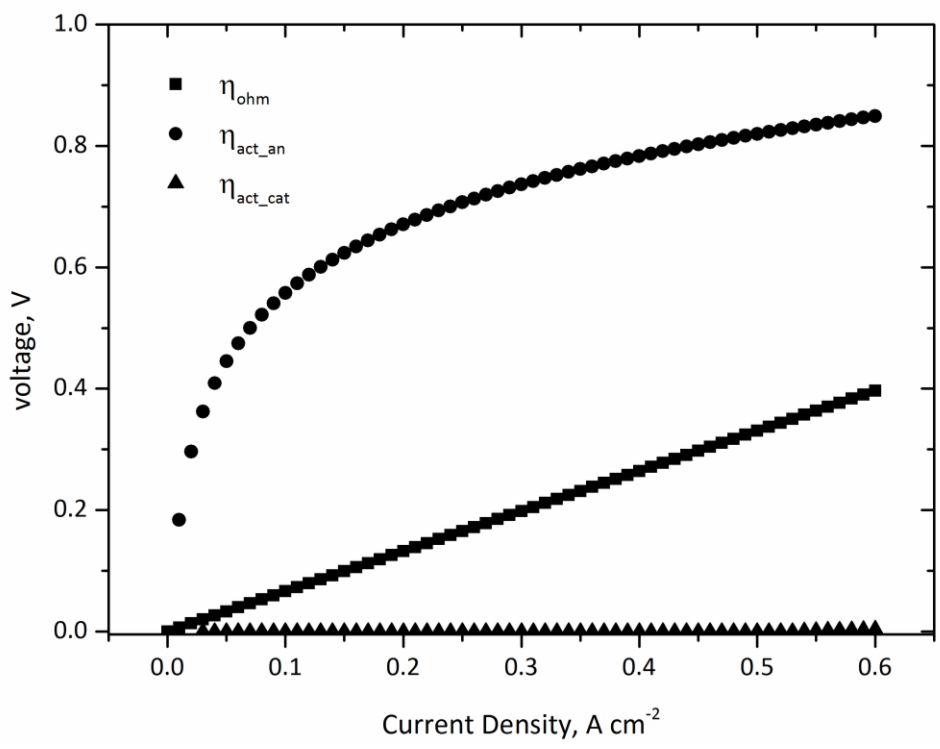

Figure 35: Contribution of anode and cathode activation overpotentials and ohmic overpotential towards the operating potential of a PEMWE cell.

5.1.9. Sensitivity Analysis

The sensitivity of the model to parameters that were assumed in obtaining the theoretical V-I relation was explored for a Nafion 117 membrane at T= 20 °C and P= 1 atm. The freed parameters were the anode and cathode charge transfer coefficients (α_{an}, α_{cat}), anode and cathode exchange current densities ($i_{0,an}$, $i_{0,cat}$) and the diffusivity of hydrogen (D_{H^+}).

The charge transfer coefficients of the anode and the cathode can have values between 0 – 2 and 0 – 1 respectively. Therefore, α_{an} and α_{cat} were varied between this range to observe the effect on the performance of the electrolyser. Figure 36 shows the effect of different values of α_{an} on the total voltage across the cell with increasing current density. It can be seen that the operating potential

of the cell decreases with increasing α_{an} indicating improved performance of the electrolyser. The effect of α_{an} on the cell potential decreases as its value increases. Increasing α_{an} reflects higher proportion of the overpotential being used for the OER which explains the improved performance of the cell.

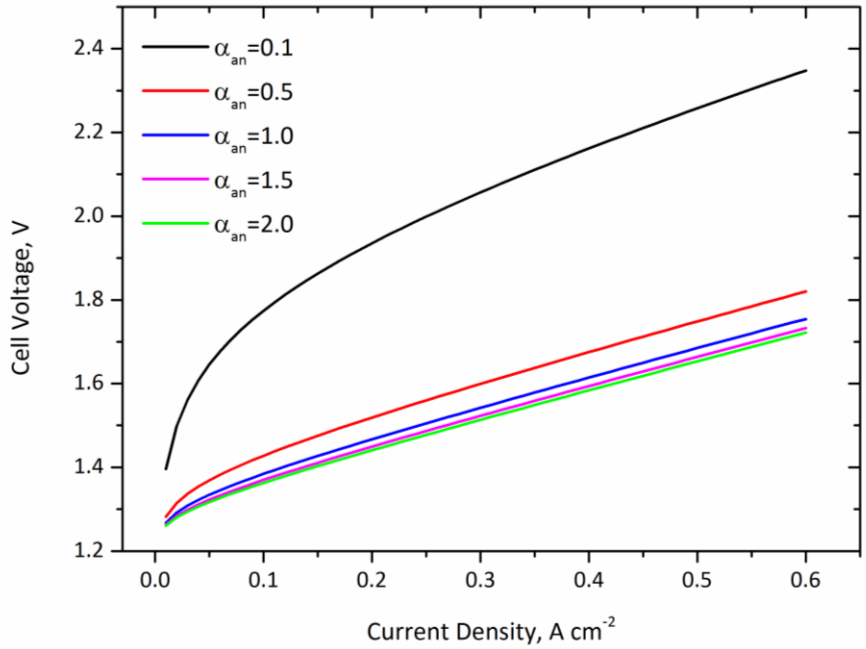

Figure 36: Influence of the anode charge transfer coefficient (α_{an}) on the operating potential of a PEMEC operating at ambient conditions (T = 20 °C, P = 1 atm).

The effect of α_{cat} on the operating potential of the cell is shown in Figure 37 and it can be seen that it has a small influence on the cell performance. It can be seen that the lower cathode charge transfer coefficients favour the electrolysis process as a lower operating voltage can be observed. Further, it can be noticed that the influence of α_{cat} becomes negligible with increasing current density. α_{cat} is dependent on the reaction involved, which is the water splitting reaction in this case and the electrode materials.

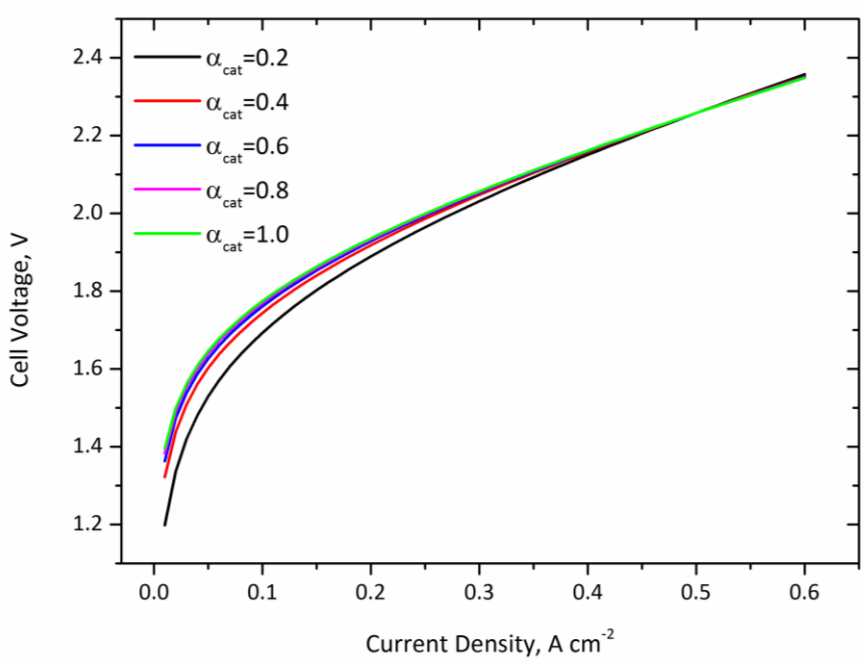

Figure 37: Influence of the cathode charge transfer coefficient (α_{cat}) on the operating potential of a PEMEC operating at ambient conditions (T = 20 °C, P = 1 atm).

Figure 38 (a) and (b) show the effect of $i_{0,an}$ and $i_{0,cat}$ parameters on the performance of the electrolyser. The parameters were varied based on values in literature. The value of $i_{0,an}$ was dispersed between 10^{-3} – 10^{-13} A cm^{-2} [129] and the value of $i_{0,cat}$ was varied in a range of 0.1 – 10^{-3} A cm^{-2} as it has a value close to 10^{-3} A cm^{-2} for Pt based catalysts [32]. It can clearly be see that change in $i_{0,cat}$ is insignificant on the overall cell voltage when compared with that of $i_{0,an}$. As discussed above, this can be explained by the fast kinetics of the HER. It can also be seen that the overall performance of the cell increases (indicating lower cell voltage) with the increasing i_0 values as expected. i_0 can be defined as the measure of amount of electron transfer activity at the equilibrium electrode potential, representing how easy an electrochemical reaction can take place, which justifies observations discussed.

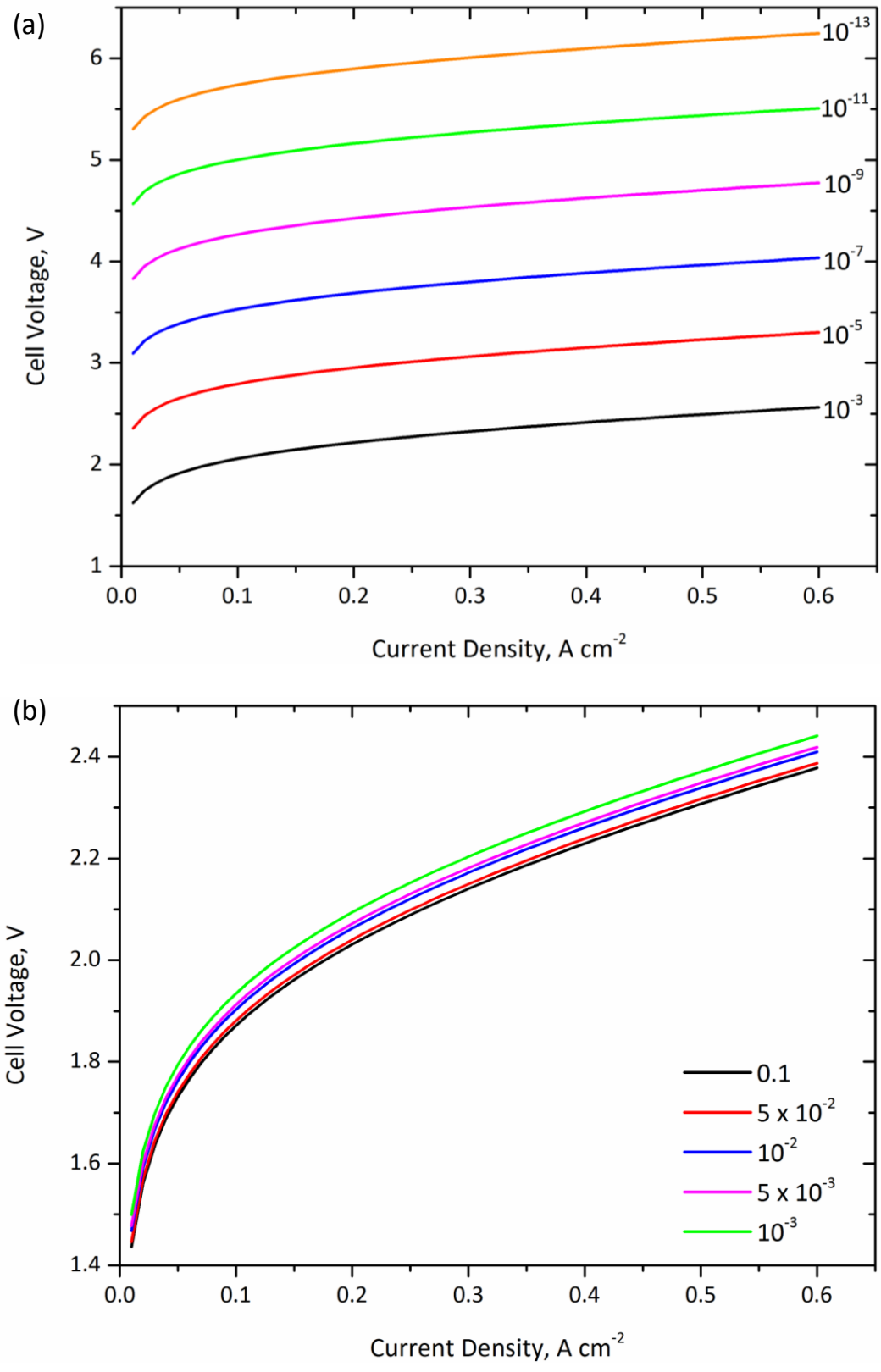

Figure 38: Influence of (a) $i_{0,an}$ and (b) $i_{0,cat}$ (A cm^{-2}) on the operating potential of a PEMWE cell operating at ambient conditions (T = 20 °C, P = 1 atm).

H^+ ions are the only mobile ions in the membrane and therefore the sensitivity of the cell potential to the diffusivity of H^+ions (D_{H^+}) was carried out and the results are shown in Figure 39. The mathematical model developed by Marangio *et al*. [129] studies the influence of temperature and pressure on D_{H^+} and its influence on the operating potential of a high pressure PEMWE. The value of D_{H^+} was varied between 5×10^{-9} – 1×10^{-10} m^2 s^{-1} based on this study. It can be seen that D_{H^+} has a significant influence on the operating potential of the cell as it increases in a magnitude of two when the value of D_{H^+} decreases from 5×10^{-10} m^2 s^{-1} to 10^{-10} m^2 s^{-1}. The influence of D_{H^+} on the cell voltage increases as its value decreases and with increasing current density.

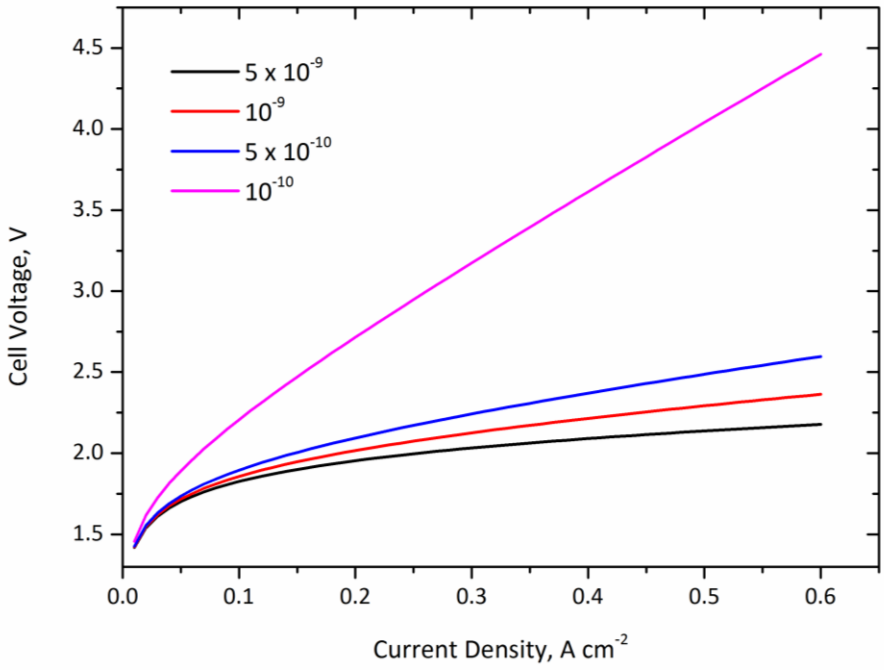

Figure 39: Influence of the proton diffusivity (D_{H^+}, m^2s^{-1}) on the operating potential of a PEMEC operating at ambient conditions (T = 20 °C, P = 1 atm).

5.1.10. Conclusion

The electrochemical model developed gives insight into the various overpotentials influencing PEMWE operation under ambient conditions. Activation and ohmic overpotentials are dominant under low current density operation and the anode activation overpotential governs the operating potential of the cell under operating conditions considered in this study.

The electrical model developed agrees well with data published in literature and it was determined that the model is very sensitive to the anode charge transfer coefficient α_{an}, anode exchange current density $i_{0,an}$ and the proton diffusivity D_{H^+} of the membrane. The accuracy of the model will be established by comparing it with experimental voltage-current data obtained from a PEMWE cell operating under identical conditions in the following section and each of the parameter values estimated above will be calculated by fitting the theoretical and experimental polarisation curves.

5.2. Lab Scale Test Cell (commercial)

The effect of water flow rate on the performance of a PEMWE was studied using a lab-scale (25 cm^2) cell at atmospheric pressure. The linear polarisation curves and EIS data were obtained at each of the water flow rates considered. Polarisation measures obtained at a water flow rate of 1 ml min^{-1} is compared with results obtained from the model in Section 5.1 for validation and fitted parameter values are reported.

5.2.1. Experimental Voltage-Current Measurements

Figure 40 compares the voltage-current characteristics at different water flow rates. The performance of the cell is consistent with data in literature for PEMWEs operating at similar conditions [18, 21] and agrees well with baseline data provided by Proton Onsite, CT, USA. The cell reaches a higher heating value (HHV) efficiency of 67% at room temperature (20 °C), atmospheric pressure (1 atm) and a water flow rate of 1 ml min^{-1} and is in close agreement with data published in literature [18, 182, 183]. It can also be seen that the water flow rate has a negligible effect on the operating voltage of the cell at lower current densities, in agreement with observations by Selamet *et al.* [184]. However, a deteriorating performance (higher voltage) of the cell can be observed with increasing water flow rate towards higher current densities. In order to delineate the various loss mechanisms in the cell and identify the source of the water flow rate dependence, EIS measurements were applied.

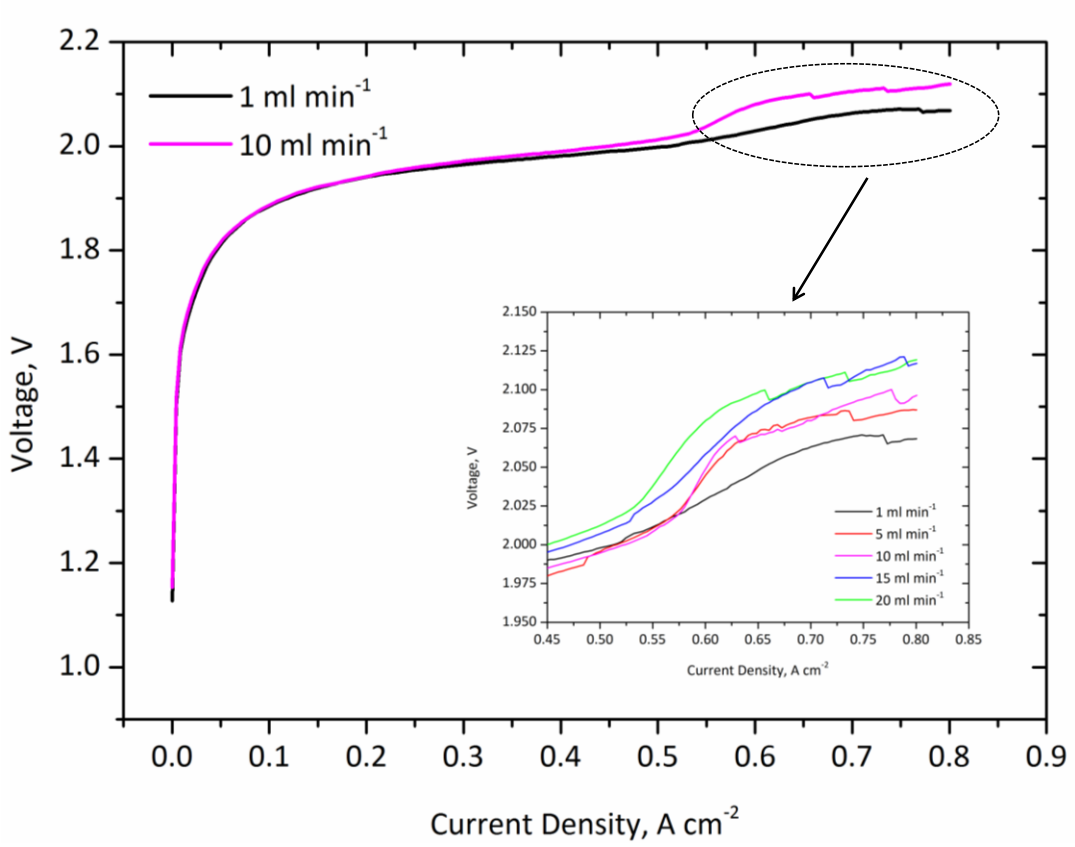

Figure 40: Voltage-current measurements of the PEMWE at varying water flow rates, with inset figure showing the variation of performance at high current density for flow rates ranging from 1 ml min^{-1} to 20 ml min^{-1}. Operation is notionally at room temperature (20°C), atmospheric pressure (1 atm).

5.2.2. Electrochemical Impedance Spectroscopy

Figure 41 (a) shows Nyquist plots obtained at 1.5, 1.7 and 1.8 V for a PEMWE cell operating at a feed water flow rate of 1 ml min^{-1} ($\zeta > 50$). The equivalent circuit shown in Figure 41 (b) can be used for theses operating potentials as there is only one impedance arc visible at this voltage range, indicating that there are no discernible mass transportation limitations. The electrical equivalent circuit is composed of a resistor in series with an RC parallel combination. R_{el} is attributed to the purely ohmic resistance of the cell that is a combination the Nafion membrane and current collector plates. This can be determined by the high

frequency intercept with the real axis. R_{ct} represents the charge transfer resistance (polarisation resistance) of the anode, since measurements are made with respect to the integrated reference electrode on the cathode side. CPE_1 is the constant phase element, which takes into account the nonuniformity and roughness of the electrode. R_{ct} can be determined by the difference between the low and high frequency intercepts on the real axis.

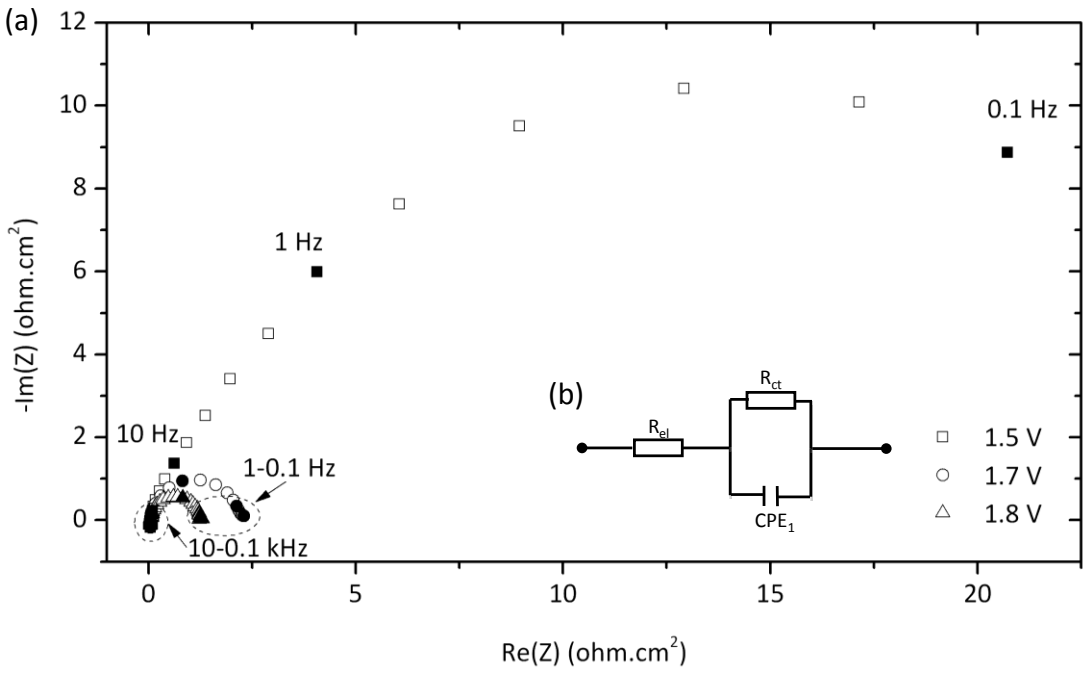

Figure 41: (a) Nyquist plots for 1.5, 1.7 and 1.8 V (ζ > 50) for a PEM water electrolyser operating at room temperature (20 °C), atmospheric pressure (1 atm) and a water flow rate of 1 ml min^{-1}. (b) Equivalent circuit for the electrolysis cell with ohmic and charge transfer resistances.

It can be seen that the high frequency intercepts of the impedance arcs are independent of the operating voltage, assuring the stability of the membrane and that it remains well-hydrated. Furthermore, it shows that the low frequency intercept of the (depressed) semicircle of the impedance spectra decreases with increasing operating voltage, indicating acceleration of the OER with increasing operating potential. Table 7 shows the fit parameters and it can be seen that the

internal resistance values obtained for this system at 1.5 V are lower than values published in literature (R_{el} > 0.1 Ω cm^2) [43, 93, 185].

Table 7: Parameters evaluated from EIS data fitting to the equivalent circuit shown in Figure 41(b) for a cell operating at 1.5, 1.7, and 1.8 V and water flow rate of 1 ml min^{-1}.

Cell Voltage (V)	R_{el} (Ω cm^2)	R_{ct} (Ω cm^2)	CPE_1	n_1[†]
1.5	0.058	28.90	0.631	0.79
1.7	0.056	2.17	0.304	0.94
1.8	0.056	1.17	0.273	0.96

[†] *n1* characterises the phase shift of CPE_1

Figure 42 (a) and (b) compares Nyquist plots obtained at 2.0 and 2.1 V when operated under water flow rates of 1 ml min^{-1}, 5 ml min^{-1} and 10 ml min^{-1}. It can be seen that a second impedance arc, that represents mass transport limitations within the PEMWE cell, begins to appear at 2.0 V. The existence of the second (low frequency) arc is due to the formation of bubbles on the electrode surface that hinder the reactant water from reaching the electrode surface [150]. The equivalent circuit used is shown in Figure 42 (c), where R_b and CPE_2 represent the resistance and constant phase element that accounts for the limited access of reactant water caused by the formation of bubbles.

When comparing Figures 42 (a) and (b), it can be seen that the second impedance arc becomes prominent with increasing operating voltage, signifying higher mass transport limitations. The voltage-current data obtained in Section 5.2.1 indicates that the current density of the cell increase from 0.6 to 0.7 A cm^{-2} during this voltage change. The reason for higher mass transport limitations at higher current densities could be due to the increase in generation of gas (oxygen and hydrogen) bubbles. It is therefore vital to have an understanding of the two-phase flow regimes that exist within the current density range considered in this study.

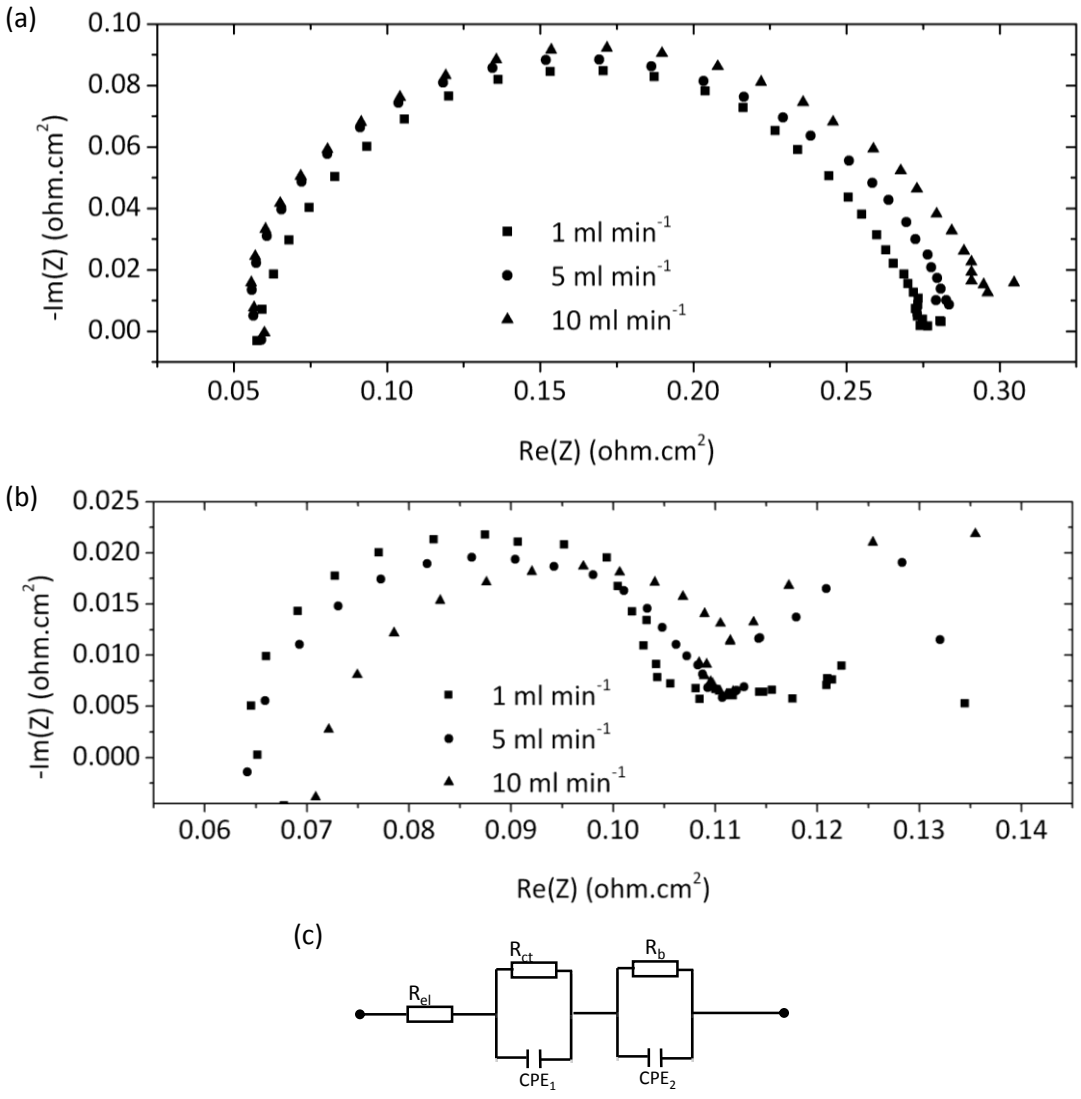

Figure 42: Nyquist plots for (a) 2.0 V and (b) 2.1 V for a PEMWE operating at room temperature (20 °C), atmospheric pressure (1 atm) and water flow rates of 1 ml min^{-1} (3 ≤ ζ ≤ 4), 5 ml min^{-1} (15 ≤ ζ ≤ 20), and 10 ml min^{-1} (30 ≤ ζ ≤ 35). (c) Equivalent circuit for the electrolysis cell with ohmic, charge transfer and mass transfer features.

Another feature observed to be a function of flow rate is the high frequency intercepts with the real axis, which is seen to increase with increasing water flow rate (Figure 42 (b)). It decreases from 0.065 Ω cm^2 at 1 ml min^{-1} to 0.064 Ω cm^2 at 5 ml min^{-1} to 0.070 Ω cm^2 at 10 ml min^{-1}. This can be attributed to a temperature effect on the proton conductivity of the electrolyte membrane. Temperature

measurements made at the exit of the cell following each polarisation sweep showed values of 24.4 °C, 22.5 °C, 22.0 °C, 21.8 °C and 20.5 °C for water flow rates increasing from 1, 5, 10, 15 and 20 ml min^{-1}, respectively. The longer residence time in the cell for lower water flow rates is consistent with a higher exit temperature that increases the proton conductivity of the membrane. While the increase in membrane resistance with water flow rate is consistent with the features seen in the voltammetry, mass transport features are much more potent at high overpotentials as seen in Figure 42 (b). Similarly, Sigrist *et al.* [186] and Cui *et al*. [187] observed a decrease in mass transport with increasing liquid flow.

5.2.3. Theoretical Two-Phase Flow

Void fraction calculations made on the system indicate that it increases from 0.03 at 0.1 A cm^{-2} to 0.19 at 0.7 A cm^{-2} (2.1 V), as shown in Figure 43. Studies by Hibiki and Mishima [188] on rectangular flow channels with upward flow indicate that the transition from bubbly to slug flow occurs when the void fraction reaches a value of 2 (α_v = 2). Therefore, the two phase flow during the impedance measurements are expected to be located exclusively within the bubbly flow regime.

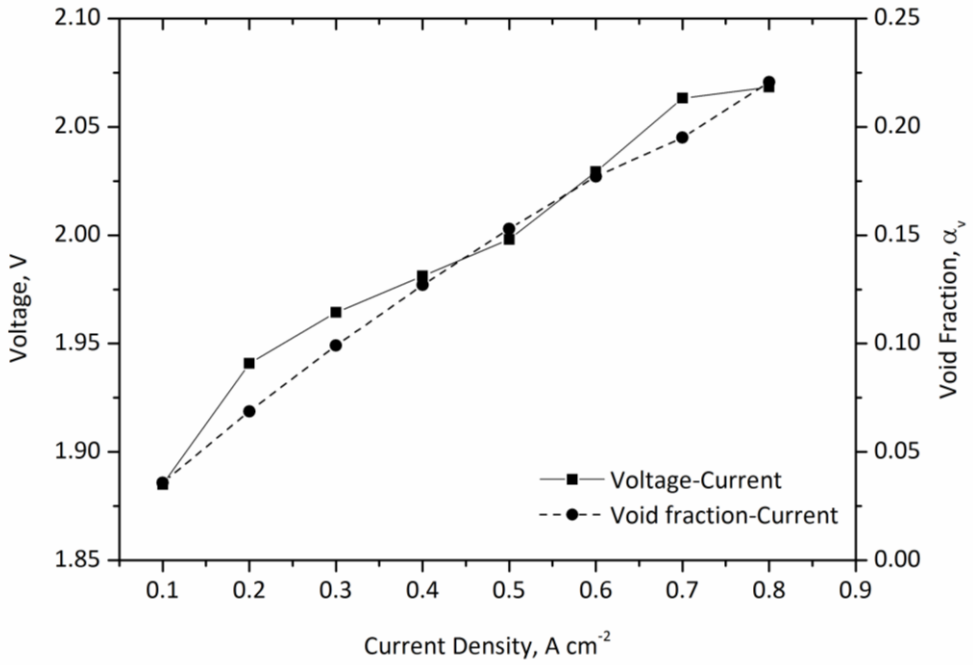

Figure 43: Variation of voltage and void fraction with current density of the PEMWE cell operating at room temperature (20 °C), atmospheric pressure (1 atm) and water flow rate of 1 ml min^{-1}.

As no transition between flow regimes is expected, the increase in mass transport limitation from Figure 42 (a) to (b) can be explained by the increase in gas formation and bubble dynamics.

Sigrist *et al*. [186] showed that gas void fraction, which is a measure of the bubble size [189], depends on the mass transfer coefficient the same way it depends on gas velocity, demonstrating an inverse relationship. Counter intuitively to a standard electrochemical system, where increased feed supply rate lowers mass transport losses, the opposite is observed in this process. This can be explained by the bubble motion and dispersion dominating the active area of the electrode. Figure 44 shows bubbles in an electrolyser channel displacing water as they rise; thus transverse motion of water enhances mass transport (assuming the motion of water due to rising bubbles is more dominant than that of pumping forces). This is because the turbulence created by the rising channel bubbles sweep bubbles off the electrode surface. However, higher water flow rates reduce the bubble size

(void fraction) and therefore reduces the mass transport / access of water to the electrode surface, as shown in Figure 44 (c).

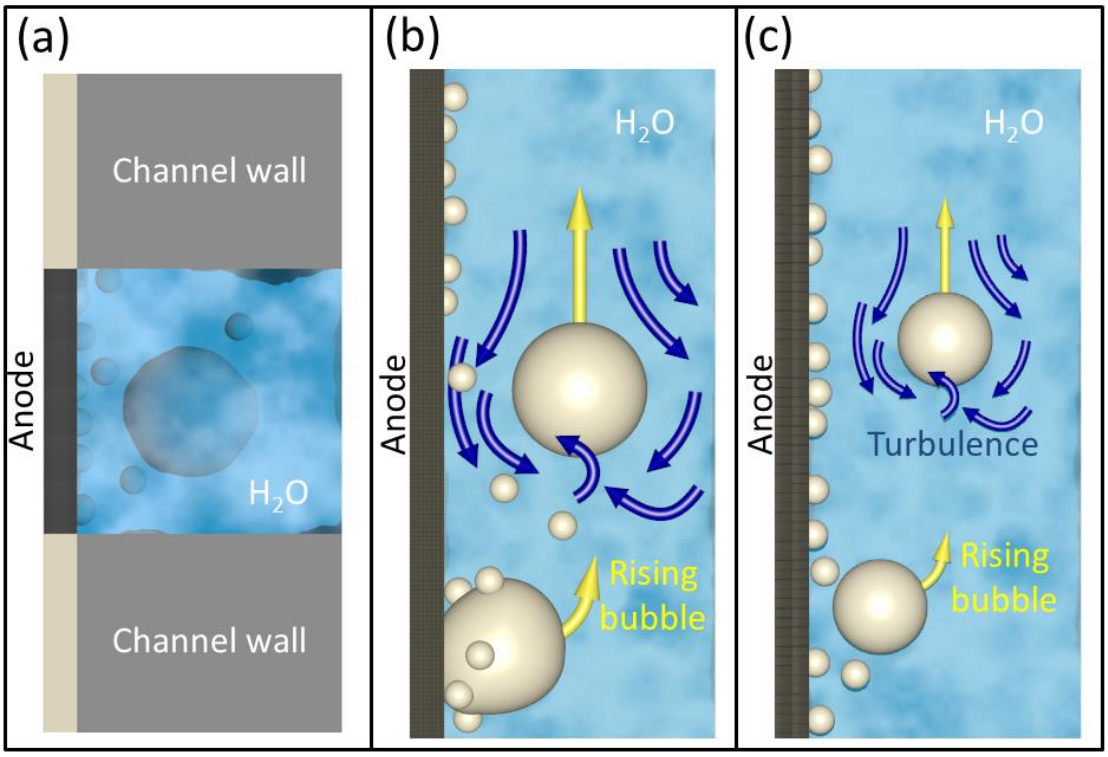

Figure 44: (a) Cross-section of the electrolyser channel; (b) flow dynamics of a rising bubble in a channel at low water flow rates with higher void fraction; and (c) higher water flow rates with lower void fraction.

5.2.4. Experimental Validation of the Model

The model developed in Section 5.1 for a PEMWE was configured to represent the cell used for experiments, operating at room temperature (20 °C) and atmospheric pressure (1 atm) and assuming negligible mass transfer losses is validated using experimental data obtained above. Experimental and theoretical anode polarisation results are shown in Figure 45. It shows that the model fits well with the experimental data obtained for the anode.

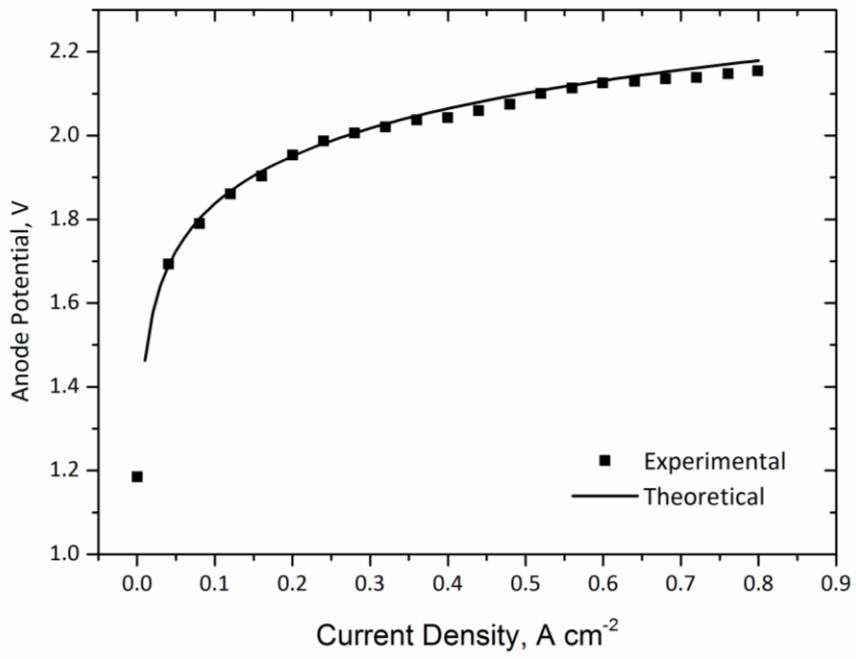

Figure 45: Comparison of the experimental and theoretical anode polarisation of PEMWE operating at room temperature (20 °C) and atmospheric pressure.

Figure 46 presents a comparison between the experimental and theoretical voltage-current data obtained for the PEMWE under identical conditions. It can be seen that the model developed agrees well with the experimental data, supporting the validity of the model. However, it can be noticed that the experimental data begins to deviate from the model as the current density increases (at about 0.5 A cm^{-2}) due to mass transport limitations that was captured by performing EIS but neglected in the model.

Concentration losses are more dominant at higher current densities, at which the oxygen gas produced forms bubbles on the electrode surface, hindering the electrolysis of water.

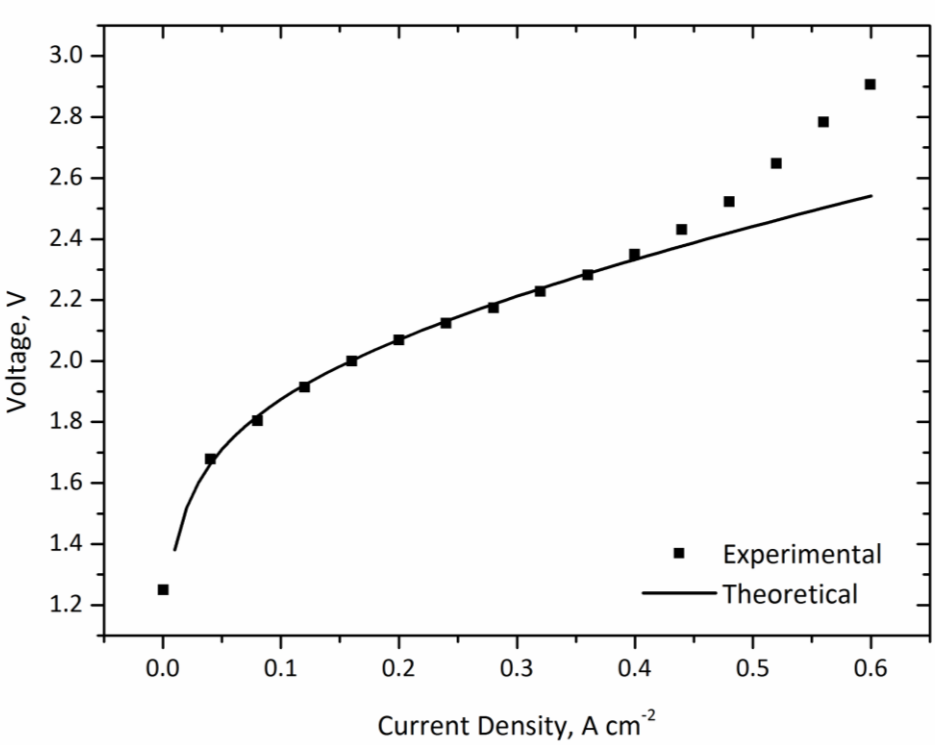

Figure 46: Comparison of theoretical and experimental V-I data for a PEMWE operating at room temperature (20 °C), atmospheric pressure and water flow rate of 1 ml min^{-1}.

A sensitivity analysis carried out on the estimated parameters of the electrolysis cell exhibited that the anode exchange current density has the largest influence on the cell potential. It also showed that the model was sensitive to charge transfer coefficients, cathode exchange current density and water diffusivity. The model can be expressed as illustrated in Equation (104) and it was fitted to experimental voltage-current data using non-linear least square (NLS) method to obtain values for the estimated parameters. In fitting the data, care was taken to ensure non-negative values for all parameters, parameters were only allowed to be within the range of those previously reported in the literature and ensuring $i > i_{0,cat}$ for the Tafel equation to be valid.

$$V = E_0 + \frac{RT}{F}\left(arcsinh\left(\frac{i}{2i_{0,an}}\right)\right) + \frac{RT}{F}\left(arcsinh\left(\frac{i}{2i_{0,cat}}\right)\right) + (R_e + R_p)Ai + \frac{\delta_m RT}{F^2 C_{H^+} D_{H^+}} i \quad (104)$$

Statistical comparison was made between the mathematical model and the experimental data in order to evaluate the accuracy of the mathematical model. It can be seen that the fit obtained for experimental data shows a good match with the model, as the goodness of fit (R^2) is close to unity with a value of 0.98 and the sum of squares due to errors (SSE) and the root mean squared error (RMSE) have values of 4.35×10^{-2} and 6.59×10^{-2} respectively.

Table 8 compares the numerical values used in the mathematical model with the experimental values. Furthermore, EIS measurements carried out previously on the cell gave an ohmic resistance of 0.058 Ω cm^2 which corresponds to a D_{H^+} value of 5.0×10^{-10} m^2 s^{-1}, which is similar to the fitted value of 6.0×10^{-10} m^2 s^{-1}. Therefore, the parameter values obtained by fitting the experimental values to the model are in close proximity with the parameter values obtained from EIS data, confirming the accuracy of the measurements.

Table 8: Initial estimated and fitted parameter values of the PEMWE.

Parameter	α_{an}	α_{cat}	$i_{0,an}$ **(A cm^{-2})**	$i_{0,cat}$ **(A cm^{-2})**	D^+_H **(m^2 s^{-1})**
Estimated	0.1	0.9	3.50×10^{-3}	0.29	1.0×10^{-9}
Fitted	0.079	0.921	3.24×10^{-3}	0.5	6.0×10^{-10}

5.2.5. Conclusion

Linear polarisation and EIS measurements were used to characterise the effect of water flow rate on the performance of a lab-scale PEMWE. Calculations of void fraction show that the flow is exclusively within the bubbly flow regime for the range of flow and current densities studied. Polarisation measurements showed a voltage increase at higher current densities that increases with water flow rate.

Decrease in water temperature with increasing water flow rate is observed; however, EIS measurements indicate that the effects of mass transport at high current densities are significantly greater than the temperature effect on membrane conductivity. Increased mass transport limitation at high current densities is attributed to bubble formation dynamics and reduced gas void fraction caused by higher water flow rates. Therefore, the coexistence of bubbles and liquid water and its effect on the performance of a PEMWE should be experimentally investigated. Furthermore, flow rate of water should be altered such that the effect of different operating flow regimes on the cell performance can be studied.

Experimental data obtained was used to validate the model developed and fitted parameter values are reported and are within the range of those published in literature.

5.3. Optical Cell

An optically transparent PEMWE cell was studied using a high-speed camera, thermal imaging and EIS to examine the relationship between flow and electrochemical performance. Flow characteristics obtained theoretically in the previous section are explored experimentally.

5.3.1. Performance Characterisation

Figure 47 compares the theoretical hydrogen gas flow rate, calculated using Faraday's law, with the actual value measured using a gas flow meter, as a function of current density. It shows that the theoretical and measured hydrogen flow rates are in close agreement, confirming that there are no side reactions in the system and the Faradaic efficiency is close to unity.

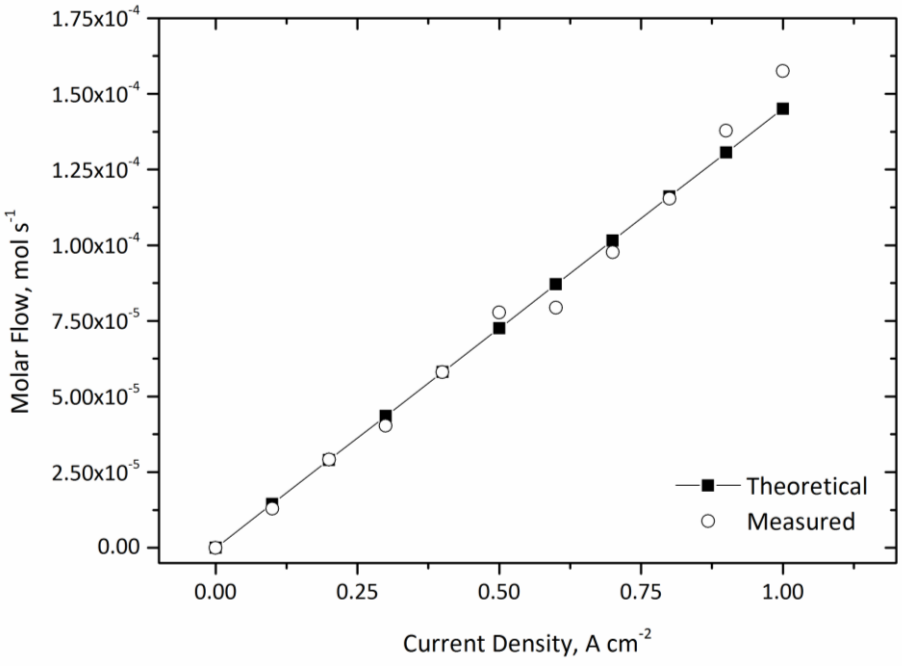

Figure 47: Comparison between the theoretical hydrogen gas flow calculated using Faraday's law and the measured hydrogen gas flow at a water flow rate of 1 ml min^{-1}.

Figure 48 (a) shows the efficiency distribution and rate of heat loss across the electrolysis cell with increasing current density when operated at standard conditions and a range of feed water flow rates. Here the efficiencies have been calculated in terms of the HHV of hydrogen as water is used in liquid form (using Equation 10). It can be seen that the electrical efficiency of the electrolyser decreases with increasing current density which is in close agreement with results presented in the literature [12]. It can also be seen that the efficiency of the cell decreases with increasing operating flow rate of inlet water, as observed by Zhang *et al.* [68]. However, the influence of feed water flow rate on the efficiency is prominent only at low current densities. This could be related to the temperature profile of the cell, as discussed above, which in turn decreases the performance of the cell.

Furthermore, Figure 48 (b) shows how the rate of heat loss from the cell initially decreases and reaches a minimum. This is associated with the thermoneutral condition of the cell, the current density for which increases with increasing water flow rate as more heat is abstracted from the system with higher flow rate.

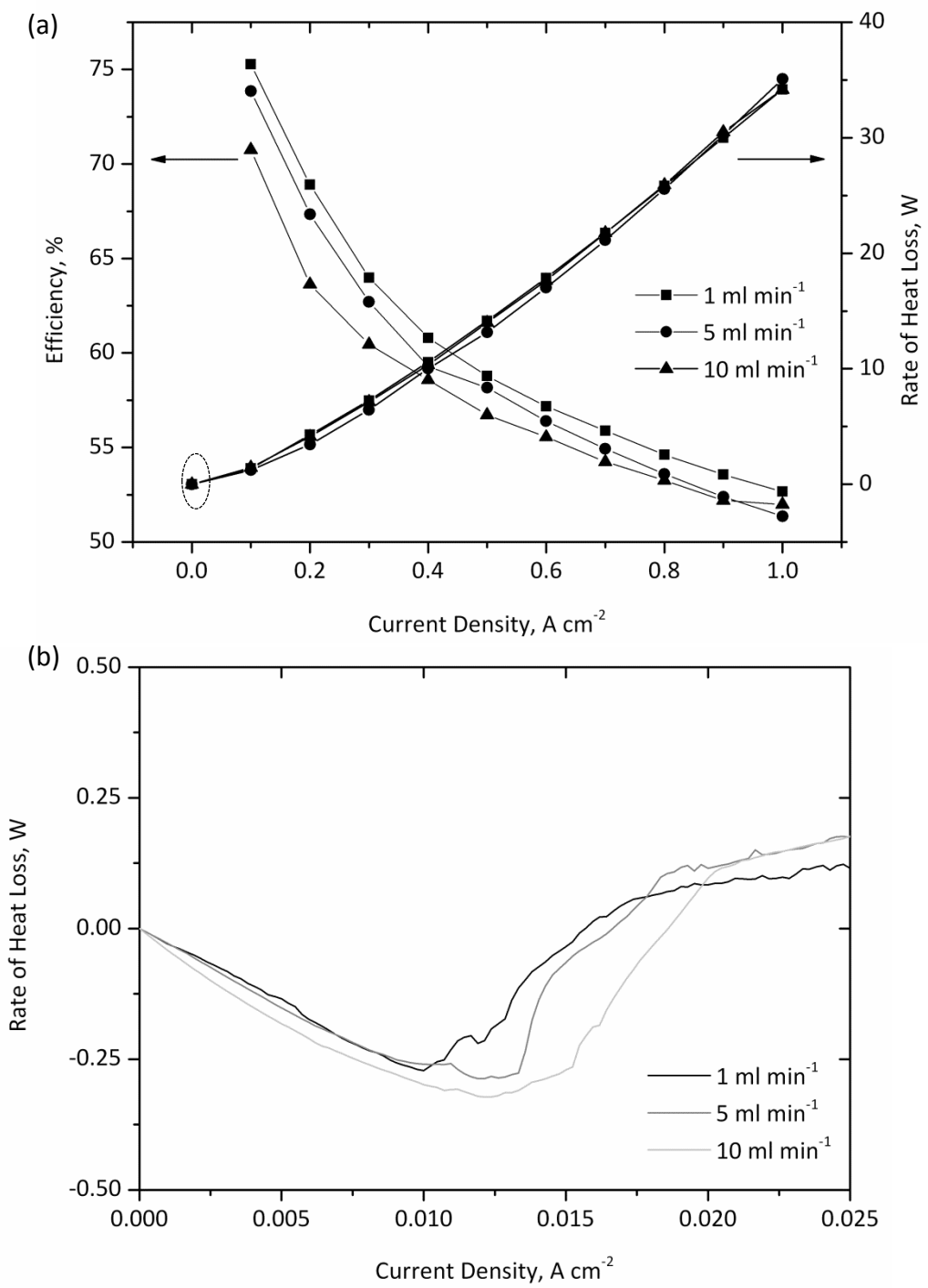

Figure 48: (a) Variation of efficiency and rate of heat loss; (b) a close up of rate of heat loss at low current densities across the electrolysis cell at different current densities when operating at 1 ml min^{-1}, 5 ml min^{-1} and 10 ml min^{-1}, room temperature (20 °C) and atmospheric pressure (1 atm).

5.3.2. Thermal Imaging

Figure 49 shows temperature profiles of the cell taken at 0.2 A cm^{-2}, 0.5 A cm^{-2}, 0.7 A cm^{-2} and 1.0 A cm^{-2} when operated at atmospheric pressure and water was fed at room temperature (20 °C) at 1 ml min^{-1}. According to the temperature scale, it can be seen that the temperature of the bipolar plates and the current collector increase gradually with increasing current density.

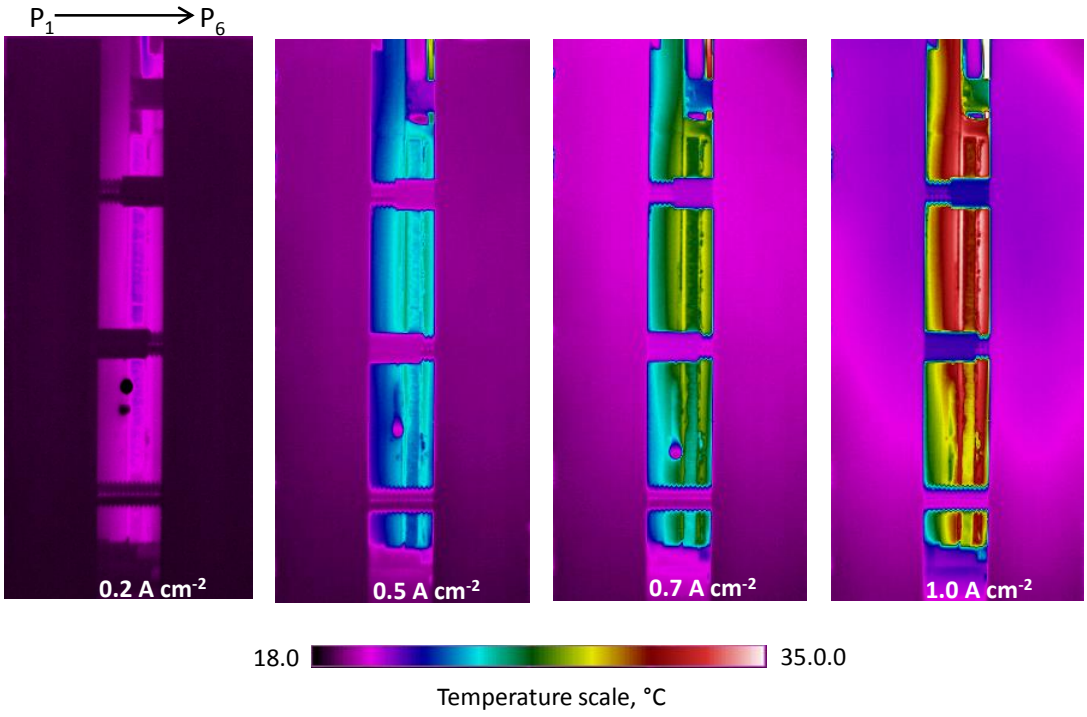

Figure 49: Thermal images of the PEM cell when operating at different current densities.

Emissivity values given in Table 9 were calculated using Equation (105) (assuming radiation of the room is negligible) and were used to calculate the temperature at the face of each plate.

$$\varepsilon_2 = \varepsilon_1 R_1 / R_2 \qquad (105)$$

where R is the radiance and is given by the software used [190].

Table 9: Properties of the materials at each temperature measurement point.

Position	Material	Thickness, mm	Emissivity	Thermal conductivity, W m^{-1} K^{-1}
P_1, P_6	Perspex	20	0.85	0.20
P_2, P_3	FR4	3.2	0.79	0.25
P_4	Graphite	2	0.27	25
P_5	FR4	1.6	0.79	0.25

Figure 50 compares the local temperature at each of the six points shown in Figure 27 as a function of current density. It can be seen that the initial temperature (at 0 A cm^{-2}) is the same for all the point and that P_4 has the highest temperature increase. P_4 represents the graphite flow field of the plate, which has the highest thermal conductivity and explains reasons for having the highest temperature increase during electrolysis. It can be seen that the overall temperature of each plate increases with increasing operating current density confirming findings in Section 5.3.1.

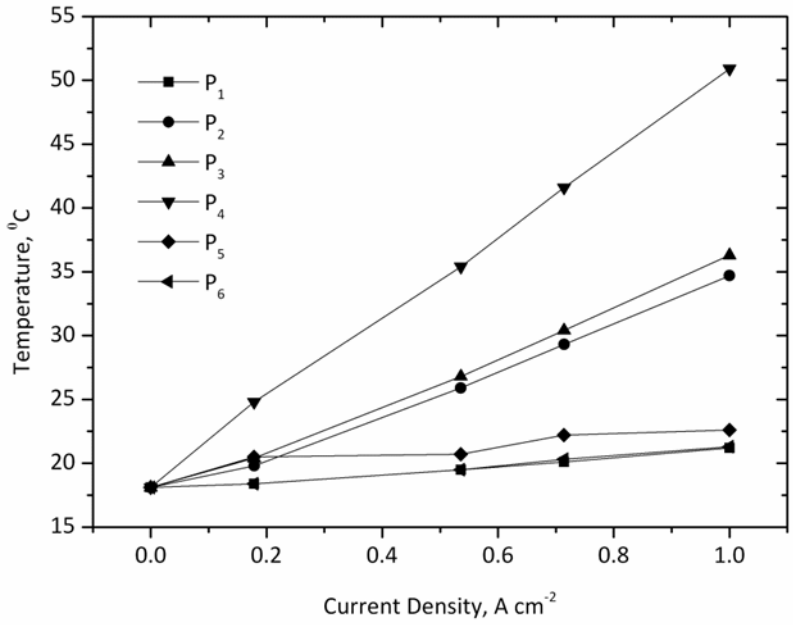

Figure 50: Temperature distribution at each point on the PEM cell when electrolysis in progress.

5.3.3. Electrochemical Performance

Figure 51 compares the performance of the electrolyser cell when operating at 1 ml min^{-1}, 5 ml min^{-1} and 10 ml min^{-1} feed water flow rates and other conditions identical to that discussed in Section 4.5.3. The overall performance of the cell agrees with data in literature and the high operating potential is similar to experimental data reported by García-Valverde *et al.* [155]. Furthermore, the figure shows that the cell has an OCV just below 1.5 V.

It can be seen that there is a small decrease in voltage with decreasing water flow rate indicating an increase in cell performance at lower current densities, which has a similar trend as results presented by Ito *et al.* [69] at lower temperatures. The reason for the improved performance can be explained by the difference in cell temperature when operating at each flow rate. It was noted that the rate of increase in cell temperature decreases with increasing flow rate of feed water as more heat is removed from the system by excess water leaving the cell. At higher

temperatures, the activation overpotential of the reaction decreases and the ionic conductivity of the membrane increases, giving lower activation and ohmic overpotentials respectively; this leads to higher performance at lower water flow rates.

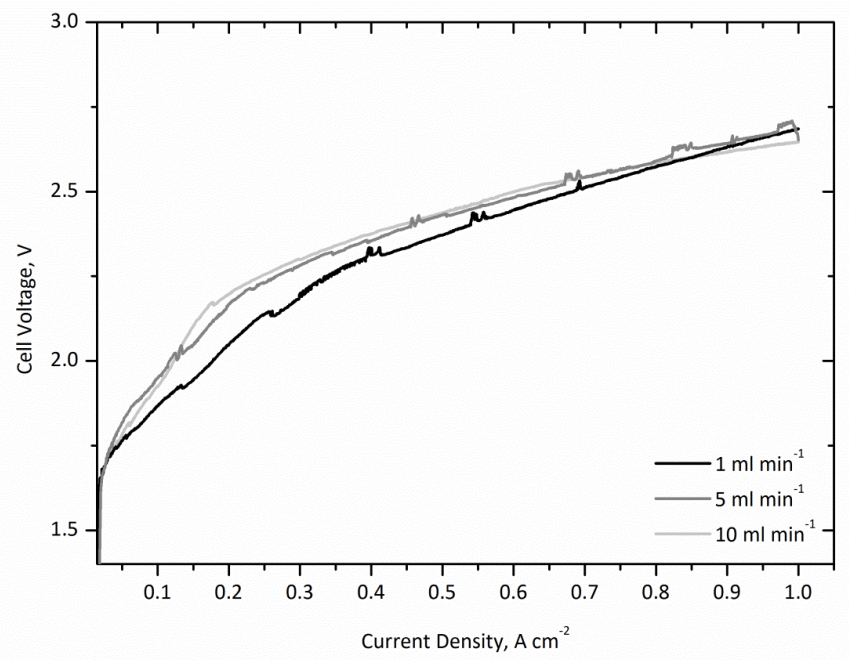

Figure 51: Galvanostatic linear sweep from 0 – 1 A cm^{-2} on the electrolysis cell with feed water flow rates of 1, 5 and 10 ml min^{-1}.

5.3.4. Electrochemical Impedance Spectroscopy

In order to get more insight into the various loss mechanisms that dictate electrochemical performance, EIS was performed under a range of operating conditions. Nyquist plots obtained at 1.6 V (1 ml min^{-1} water flow rate, $\zeta > 10$) at different time intervals are shown in Figure 52 (a). The electrical equivalent circuit is shown in Figure 52 (c) and is composed of a resistor in series with an RC parallel combination. R_{el} is attributed to purely the ohmic resistance of the cell that is a combination of the Nafion membrane and current collectors. This can be

determined by the high frequency intercept with the real axis, as shown in Figure 52 (b). R_{ct} represents the charge transfer resistance (polarisation resistance) of the anode, assuming that of the cathode is relatively insignificant due to fast kinetics of the HER. CPE_1 is the constant phase element, which takes into account the nonuniformity and the roughness of the electrode. R_{ct} can be determined by the difference between the low and high frequency intercepts on the real axis.

Figure 52 (b) shows that the high frequency intercept of the impedance arc remains relatively unchanged, decreasing slightly (from 1.53 Ω cm^2 at 0 s to 1.40 Ω cm^2 at 1375 s); this can be related to the increase in cell temperature that was observed during the measurements. Table 10 shows the fit parameters. The internal resistance values obtained for this system are relatively high compared to some published values for PEM electrolysers (0.38 Ω cm^2) [191] but close to values published by Millet *et al*. [43] (typ. 1 Ω cm^2). The relatively high values can be attributed to the unique design using PCBs to allow optical access to the electrode. R_{ct} remains stable indicating that there is no sign of electrode degradation on this timescale.

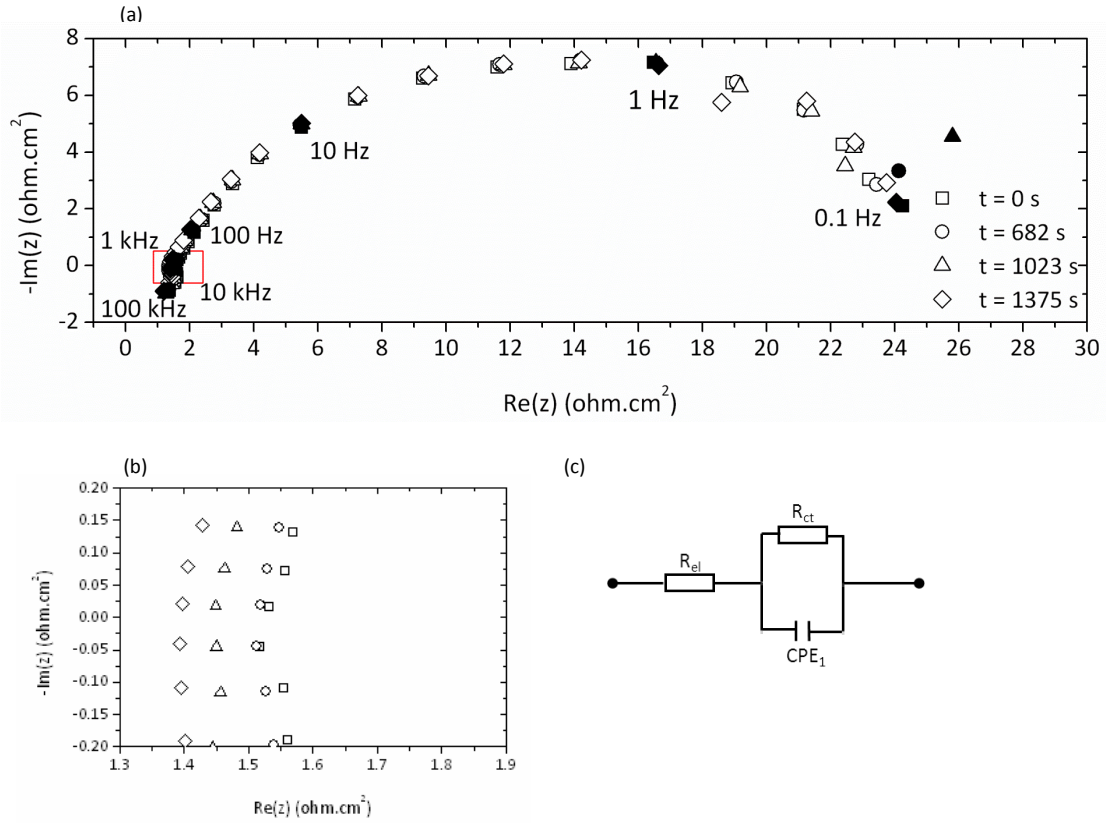

Figure 52: (a) Nyquist plots for electrolysis cell operating at 1.6 V and a feed water flow rate of 1 ml min^{-1} (ζ > 10) for a period of 1375 s. (b) A close up of high frequency intercepts of Nyquist plots. (c) Equivalent circuit for the electrolysis cell with ohmic and charge transfer resistances.

Table 10: Parameters evaluated from EIS data fitting to the equivalent circuit shown in Figure 50 (c) for a cell operating at 1.7 V at different time intervals.

Time (s)	R_{el} (Ω cm^2)	R_{ct} (Ω cm^2)	CPE_1	n_1
0	1.530	24.10	0.113	0.70
682	1.520	24.50	0.112	0.70
1023	1.450	25.40	0.114	0.68
1375	1.400	24.40	0.108	0.70

Figure 53 (a) shows the EIS results at varying operating potentials (1.5, 1.6 and 1.7 V). There is only one impedance arc visible at this voltage range, indicating that there are no significant mass transportation limitations. Therefore, the electrical analogy presented in Figure 53 (c) can be used for this range of operation. It can be seen that the diameter of the semicircle of the impedance spectra decreases with increasing operating voltage, indicating acceleration of the OER with increasing overpotential. The high frequency intercepts are independent of the operating voltage showing that the membrane remains well-hydrated and stable.

Under standard conditions of temperature and pressure and when water is in liquid form and hydrogen and oxygen are in gaseous form, the enthalpy of Reaction (3) is: $\Delta H_r(H_2O)$ = 285.84 kJ mol^{-1}, which corresponds to a thermoneutral voltage of 1.48 V [18]. A value of 0.01 A cm^{-2} was obtained for the thermoneutral current density using impedance values obtained at 1.5 V (close to thermo-neutral voltage) which agrees with the experimental value that is given by Figure 48 (b) (0.015 A cm^{-2}).

Figure 53 (b) compares impedance plots obtained at higher voltages (2.3 and 2.5 V). It can be seen that the Nyquist plot at 2.3 V consists of a noticeable second feature at low frequencies which is associated with mass transport limitations. The existence of the second arc can be explained by the formation of bubbles on the electrode surface that hinders access of water, as discussed later. Therefore, its equivalent electrical circuit has an addition RC combination, as shown in Figure 53 (d), where R_b and CPE_2 represent the resistance and constant phase element due to limited access of reactant water caused by the formation of bubbles. Fitted parameters for the various polarisation conditions are given in Table 11.

Table 11: Parameters evaluated from EIS data fitting to the equivalent circuit shown in Figure 53 (c) for a cell operating at 1.5, 1.6, 1.7, 2.3 and 2.5 V.

Voltage (V)	R_{el} (Ω cm^2)	R_{ct} (Ω cm^2)	CPE_1	n_1
1.5	1.66	145.0	0.13	0.64
1.6	1.49	24.40	0.11	0.70
1.7	1.36	9.50	0.14	0.73
2.3*	0.88	0.70	0.17	0.74
2.5	0.85	0.54	0.10	0.78

*only the high frequency arc is considered

When the voltage is increased further to 2.5 V the second arc disappears, indicating that the mass transport limitation effect has ceased. As this effect is taken to be linked to bubble formation and the hydrodynamics within the cell, further investigation of the flow regime and effect of changing flow conditions is required and will be discussed in the following section.

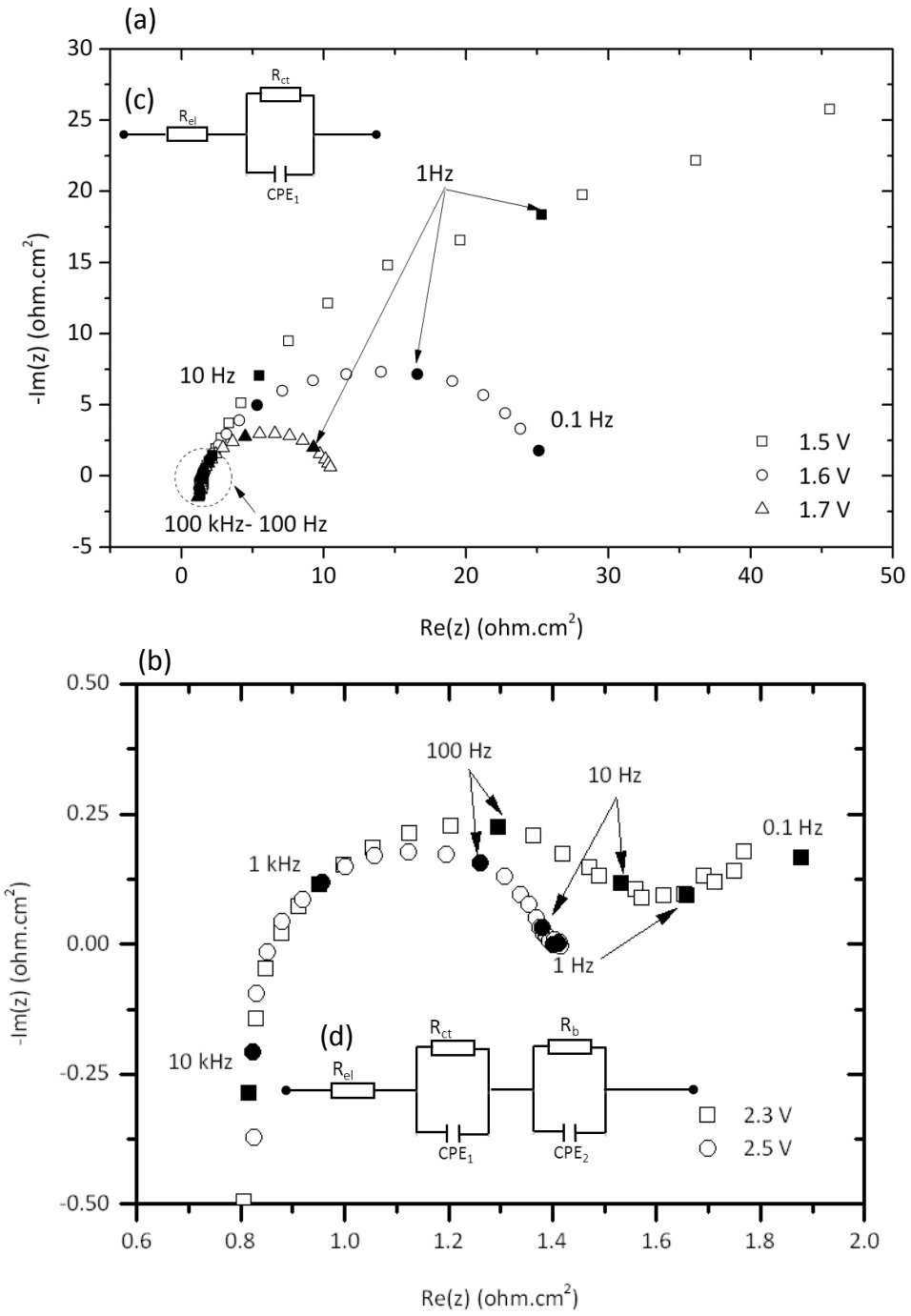

Figure 53: Nyquist plots for: (a) 1.5, 1.6 and 1.7 V (ζ > 10); (b) 2.3 (ζ = 2) and 2.5 V (ζ = 1) for a PEM water electrolyser operating at room temperature (20 °C), atmospheric pressure (1 atm) and a water flow rate of 1 ml min^{-1}. (c) Equivalent circuit for the electrolysis cell with ohmic, charge transfer resistances and (d) mass transfer limitations.

Figures 54 and 55 compare Nyquist plots of the electrolysis cell at 1.6 V and 2.0 V when operated under different feed water flow rates. In Figure 54 it can be seen that feed water flow rate has little effect on EIS measurements when operated close to OCV. The internal resistances at each flow rate is fairly similar and explains the similar current density values obtained at this potential by the VI sweeps in Section 5.3.3.

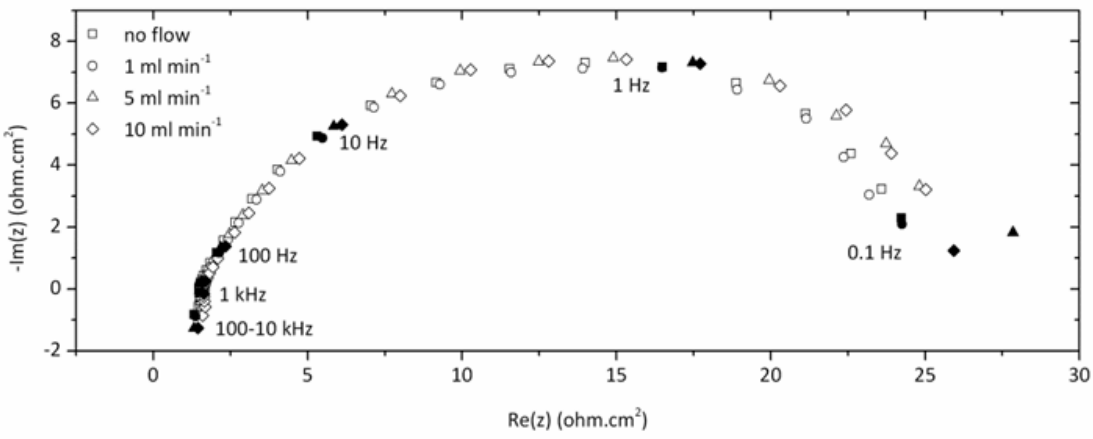

Figure 54: Nyquists plots of the PEM cell at 1.6 V when operating at 0 ml min^{-1}, 1 ml min^{-1}, 5 ml min^{-1} and 10 ml min^{-1}.

However, Figure 55 shows that increasing feed water flow rate has a negative impact on the performance of the cell which is indicated by the increase in the second arc of the Nyquist plots and will be explained with the aid of optical measurements. Furthermore, it can be seen that the internal resistances increase with increasing water flow rate. This is consistent with the lower increase in temperature associated with higher flow rates, as described previously.

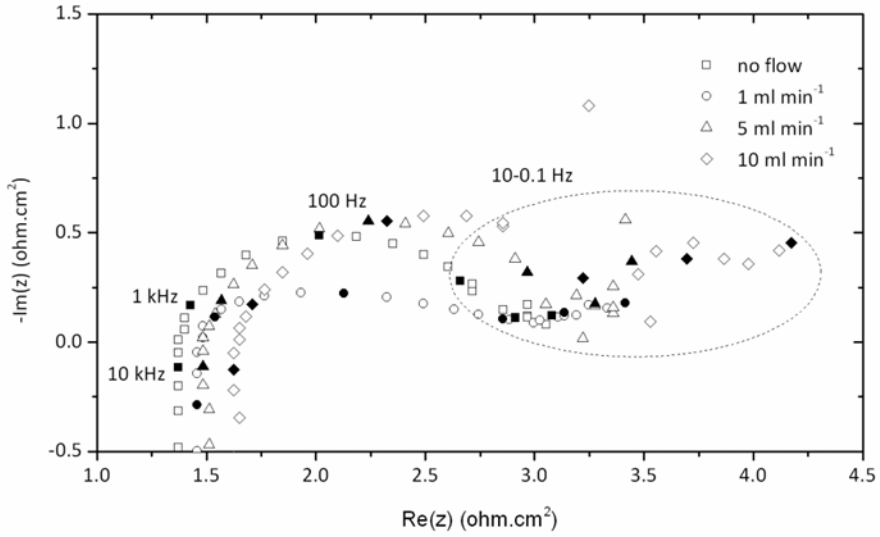

Figure 55: Nyquist plots of the PEM cell at 2.0 V when operating at 0 ml min^{-1}, 1 ml min^{-1}, 5 ml min^{-1} and 10 ml min^{-1}.

5.3.5. Optical Visualisation

Formation of oxygen and hydrogen gas bubbles on the electrode surface and their transportation in the flow fields can hinder access of fresh water to the electrode and negatively impact performance. Therefore, it is vital to have a thorough understanding of the two-phase flow inside an electrolysis cell and the formation and detachment mechanism of bubbles formed on the electrode surface. This section uses an optical cell and high-speed camera to examine these issues under different operating conditions.

It was observed that increase in current density increases the size of the bubbles and the regularity of their occurrence, indicating an increase in generation of oxygen gas. Figure 56 shows the variation of the oxygen gas bubble sizes and its flow along (up) the channel with increasing current density (0.1 – 1.0 A cm^{-2}). With increasing current density, bubbles cover a larger portion of the electrode, starving

the surface of fresh reactant and supporting the association of the low frequency EIS arc with bubble formation, as seen in Figure 53 (b).

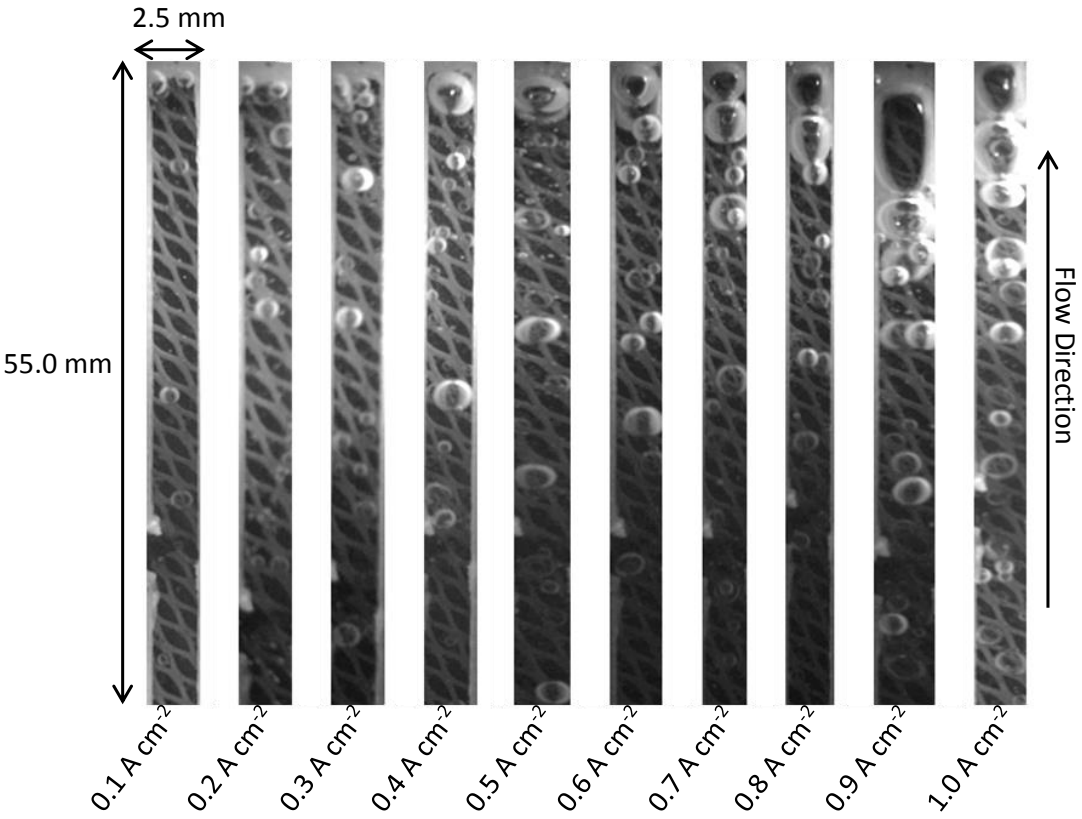

Figure 56: Flow regimes visible in the middle anode channel of a PEM water electrolyser operating at room temperature (20 °C), atmospheric pressure (1 atm) and feed water flow rate of 1 ml min^{-1}.

Figure 57 shows two-phase flow profiles for three different feed water flow rates, each operating at 1 A cm^{-2}. It can be seen that the size of the bubbles decrease significantly with increasing flow rates of water. Bubbles are discharged from the electrode surface when their diameter reaches a critical value, at which the force of adhesion is equal to the gravitational buoyancy force [192]. Adhesion force is inversely proportional to the size which gives smaller bubbles at higher flow rates [193].

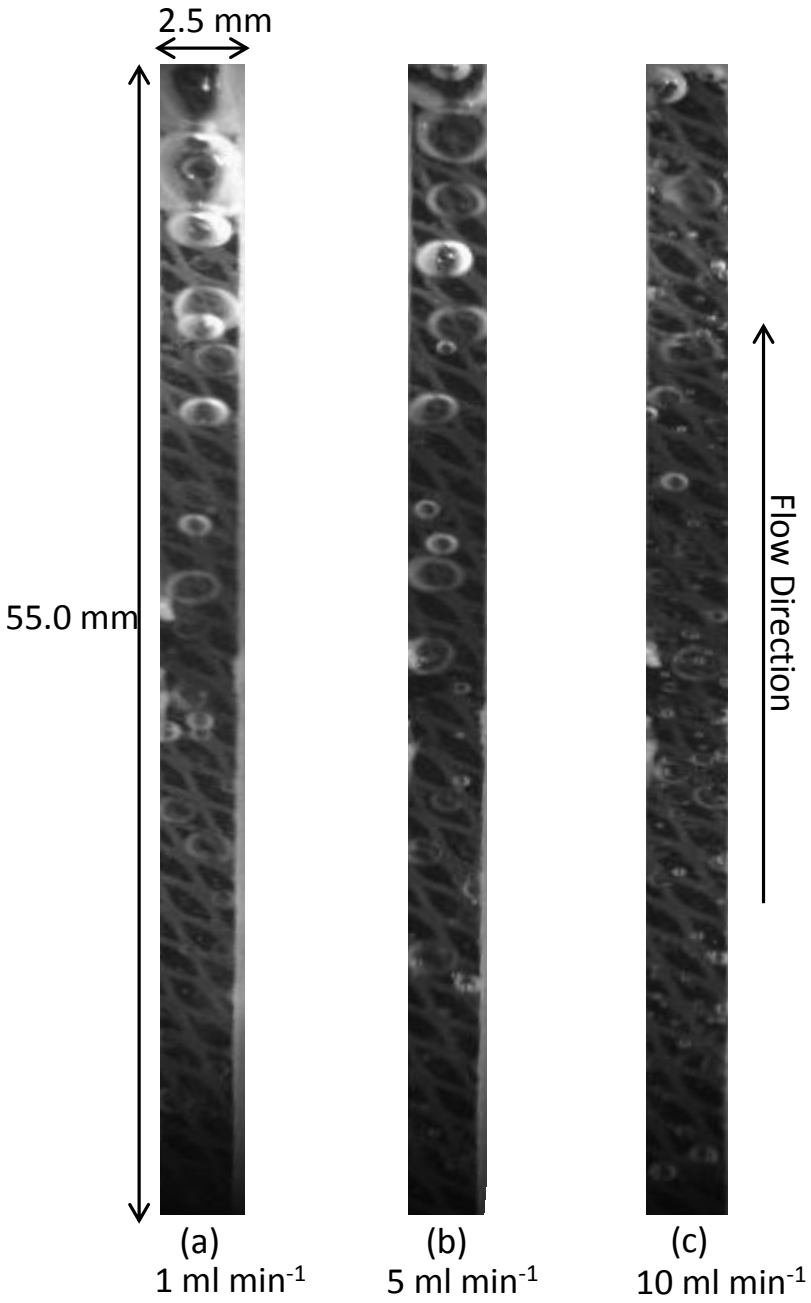

Figure 57: The two-phase flow pattern in the middle anode channel of the PEMWE when operated at 1 A cm^{-2} and a feed water flow rate of: (a) 1 ml min^{-1}, (b) 5 ml min^{-1} and (c) 10 ml min^{-1}.

Figure 58 shows the flow map presented by Mishima and Hibiki [194] for a small diameter channel of 2.05 mm and shows the flow regimes inside the middle channel of the electrolyser based on superficial velocity calculations and confirms the above observations. It can be seen that the flow is mostly bubbly at low current densities and shifts to slug flow as the current density increases. Furthermore, the flow patterns tend to be within bubbly flow as the feed water flow rate increases.

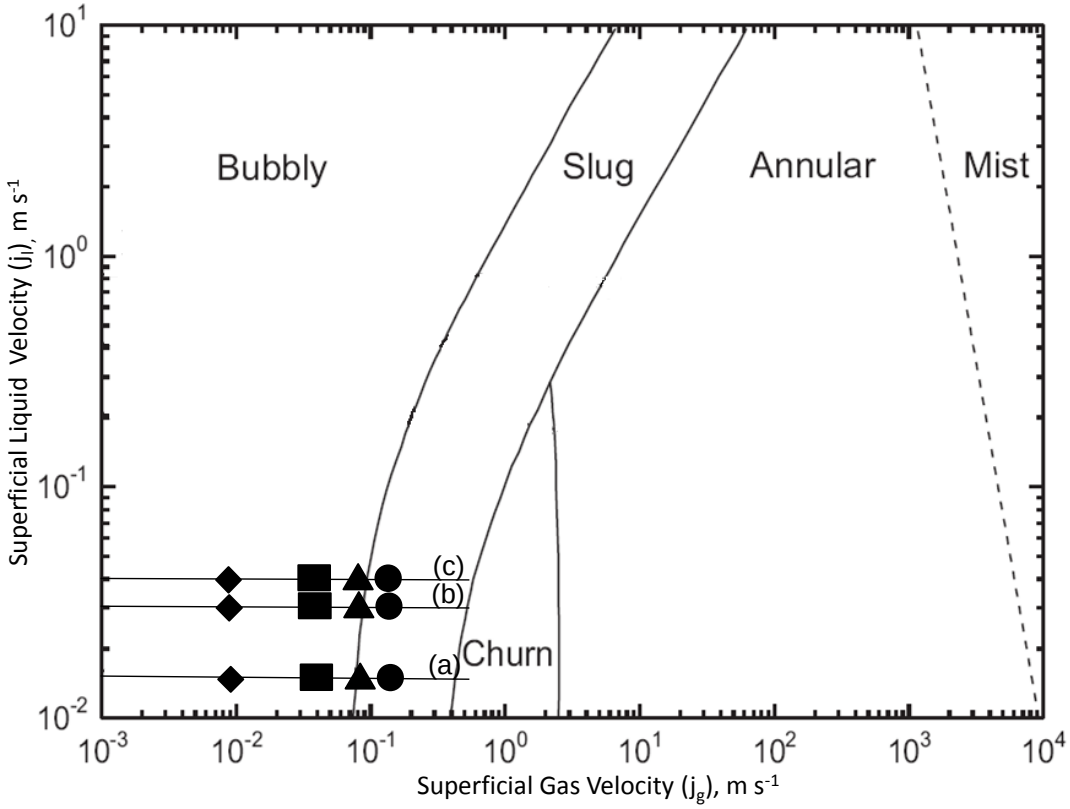

Figure 58: Two-phase flow patterns visible on the flow regime map presented by Mishima and Hibiki [194] at (♦) 0.2 A cm^{-2}, (■) 0.5 A cm^{-2}, (▲) 0.7 A cm^{-2} and (●) 1.0 A cm^{-2} in the middle channel on the anode side when operating at a feed water flow rate of (a) 1 ml min^{-1}, (b) 5 ml min^{-1} and (c) 10 ml min^{-1}.

When operating at a feed water flow rate of 1 ml min^{-1} transition from bubbly to slug flow occurs at 0.7 A cm^{-2}, (corresponding to a cell voltage of 2.5 V, see Figure 51). Work done by Ito *et al*. [69, 138] looked at the two phase flow in a PEM water electrolyser from a theoretical perspective and suggests that transition from bubbly to slug flow has a negative impact on the mass transport in a PEM water electrolyser cell. However, the experimental work illustrated here presents evidence that the transition from bubble to slug flow enhances mass transport, as has been reported in other electrochemical systems [195-197]. This explains the EIS results in Figure 53 (b), that shows improved mass transport properties associated with an increase in cell voltage / current density.

5.3.6. Conclusion

Assessment of technology performance, understanding the mechanism of operation and optimising process variables and device design, all benefit from the availability of suitable diagnostic techniques. Here, electrochemical impedance spectroscopy, thermal imaging and high-speed photography have been used to study the operation of an optically transparent water electrolyser based on a PCB current collector.

The heating effect on cell performance points to performance improvements associated with lower membrane resistance. The two-phase flow in channels shows a transition from bubble to slug flow that is associated with improvement in mass transport. This transition is a function of flow rate and current density. It was observed that the flow changes from bubbly to slug flow at higher current densities which improves mass transport at the surface of the electrode. This result suggests that operational parameters (flow and current density) can be optimised to ensure effective performance.

5.4. Segmented Cell

A PEMWE employing a segmented current collector made utilising PCB technology with optical access to the channel was demonstrated for the first time. The cell allowed the local current density, flow regime and bubble formation dynamics to be studied in real time.

5.4.1. Performance of Pt/Ru Electrodes

Whole-cell polarisation performance of the prepared Pt / Ru electrodes (1 ml min^{-1} water flow, 20 ° C, unpressurised) is presented in Figure 59. The performance of the electrocatalyst is reproducible and stable under the current density range considered and has a relatively good performance compared to literature reports under similar conditions [18, 21].

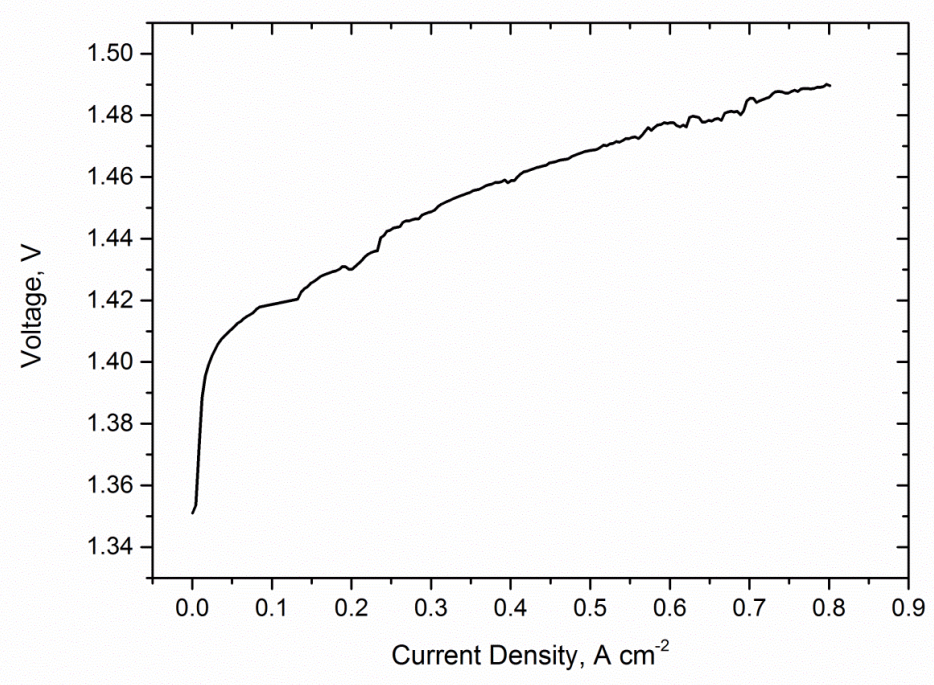

Figure 59: Polarisation curve of whole-cell PEMWE with Pt / Ru electrocatalyst on the anode and cathode operated at room temperature (20 °C) atmospheric pressure (1 atm) and a feed water flow rate of 1 ml min^{-1}.

5.4.2. CDD Along the Electrolyser Channel

Figure 60 shows the CDD measurements across the 8 segments under 'low' (1.45 V), 'medium' (1.50 V) and 'high' (1.80 V) operating potentials at a water flow rate of 1 ml min^{-1}. It can be seen that the current density distribution along the channel is relatively homogeneous at low operating potentials. However, while increasing the operating potential of the cell consistently leads to a local current increase at each segment, there is a significantly larger increase in current along the channel.

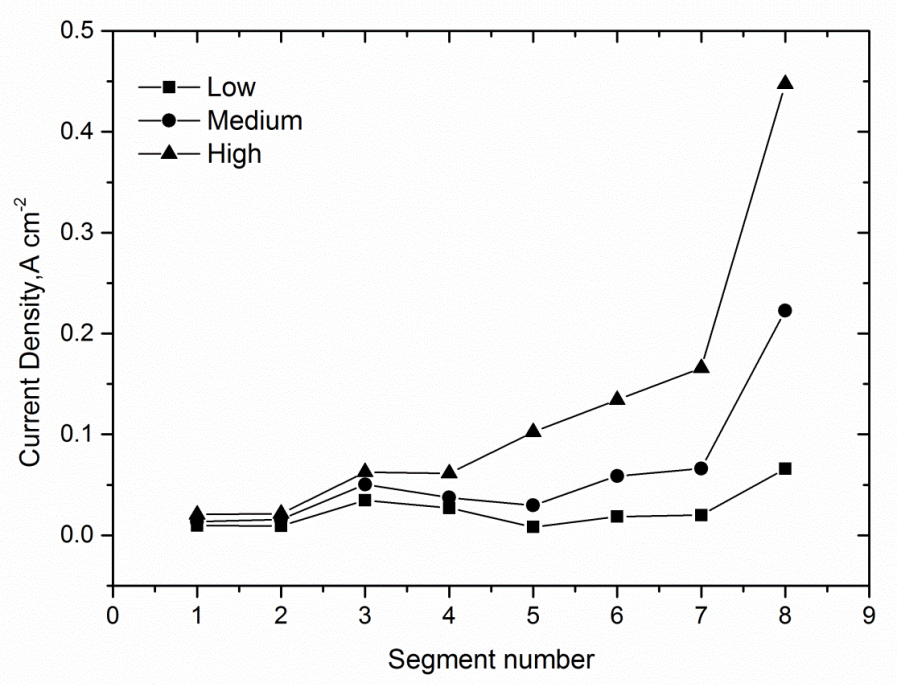

Figure 60: Current density distribution along the flow channel for the 8 segments at Low, Medium and High operating potentials when operating at a water flow rate of 1 ml min^{-1}. See Figure 31 for distribution of channel segments.

Figure 61 (a) and (b) show the current density variation across the 8 segments of the cell when operating at water flow rates of 3 ml min^{-1} and 5 ml min^{-1}, respectively. The trend of CDD is similar to that observed in Figure 60.

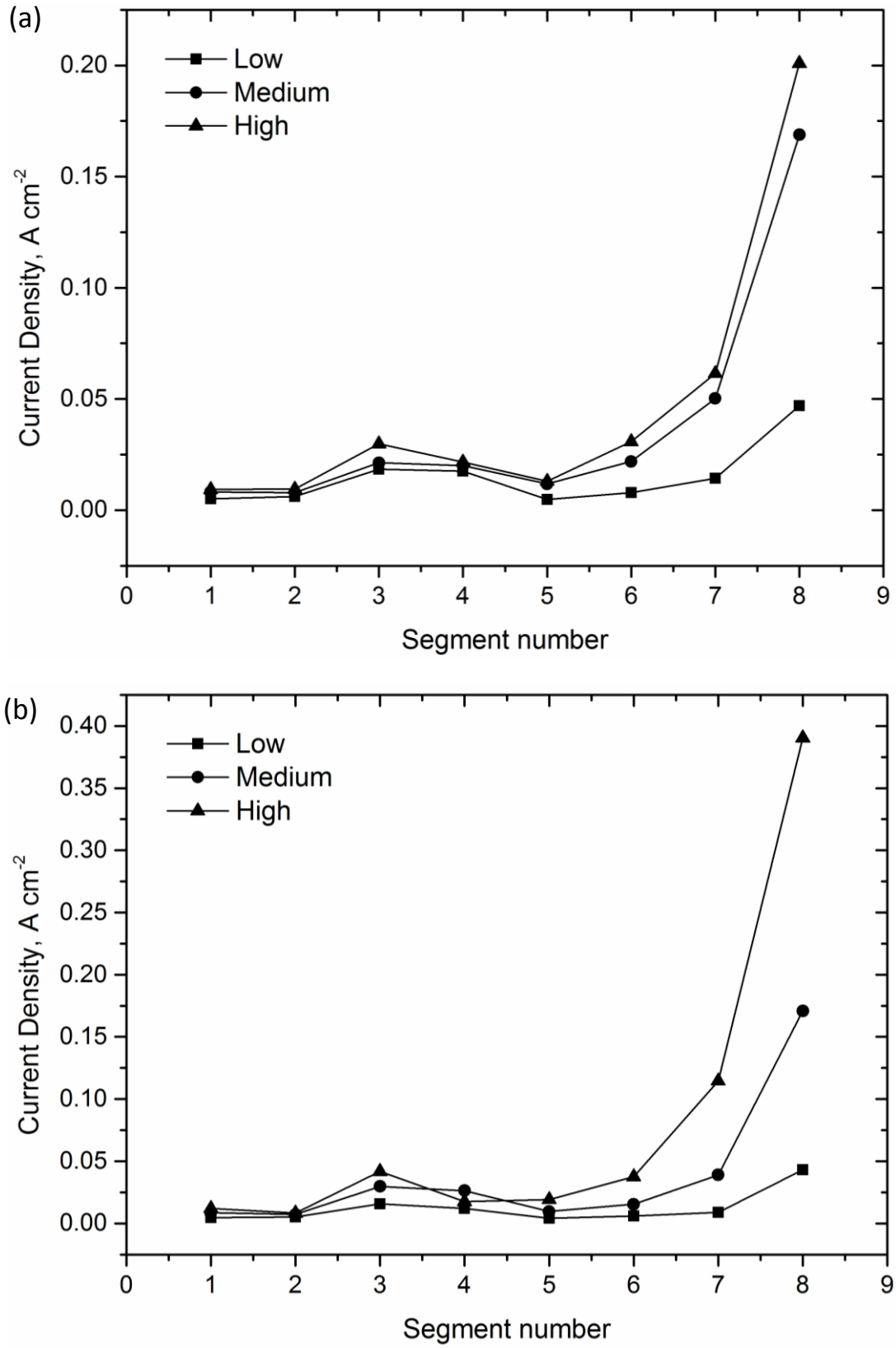

Figure 61: Current density of the segments at Low, Medium and High cell potentials and when operating at a water flow rate of (a) 3 ml min^{-1} and (b) 5 ml min^{-1}.

It can be seen that the increase in water flow rate decreases the current density variation across the segments at low and medium operating potentials. Furthermore, it shows that at a fixed operating potential, the current densities across the segments decrease with increasing water flow rate, this can be explained by the decrease in cell temperature at higher water flow rates that was observed in Section 5.2.2 [150].

5.4.3. Visual Imaging of Bubble Size and Two Phase Flow Patterns

Studies have shown that the flow regime in an electrolyser can have a significant effect on performance [150]. Flow pattern visualisation and transition from bubbly to slug flow in an electrolyser has been studied in Section 5.3.5 [150]. However, there is little understanding of how the evolution of flow affects the local current distribution. By performing combined current density distribution and optical visualisation of bubble characteristics it is possible to reconcile the two.

Image captures obtained by direct visualisation of the electrolyser anode flow channel are shown in Figure 62. It can be seen that the regularity of bubble occurrence and their size increased with increasing total cell current, indicating an increase in oxygen gas generation. It also shows that the bubbles on the top part of the cell (Segments 6-8) are larger and more frequent than in the bottom part of the cell due to both an accumulation of bubbles formed lower down in the channel and a higher rate of oxygen generation towards the top of the channel.

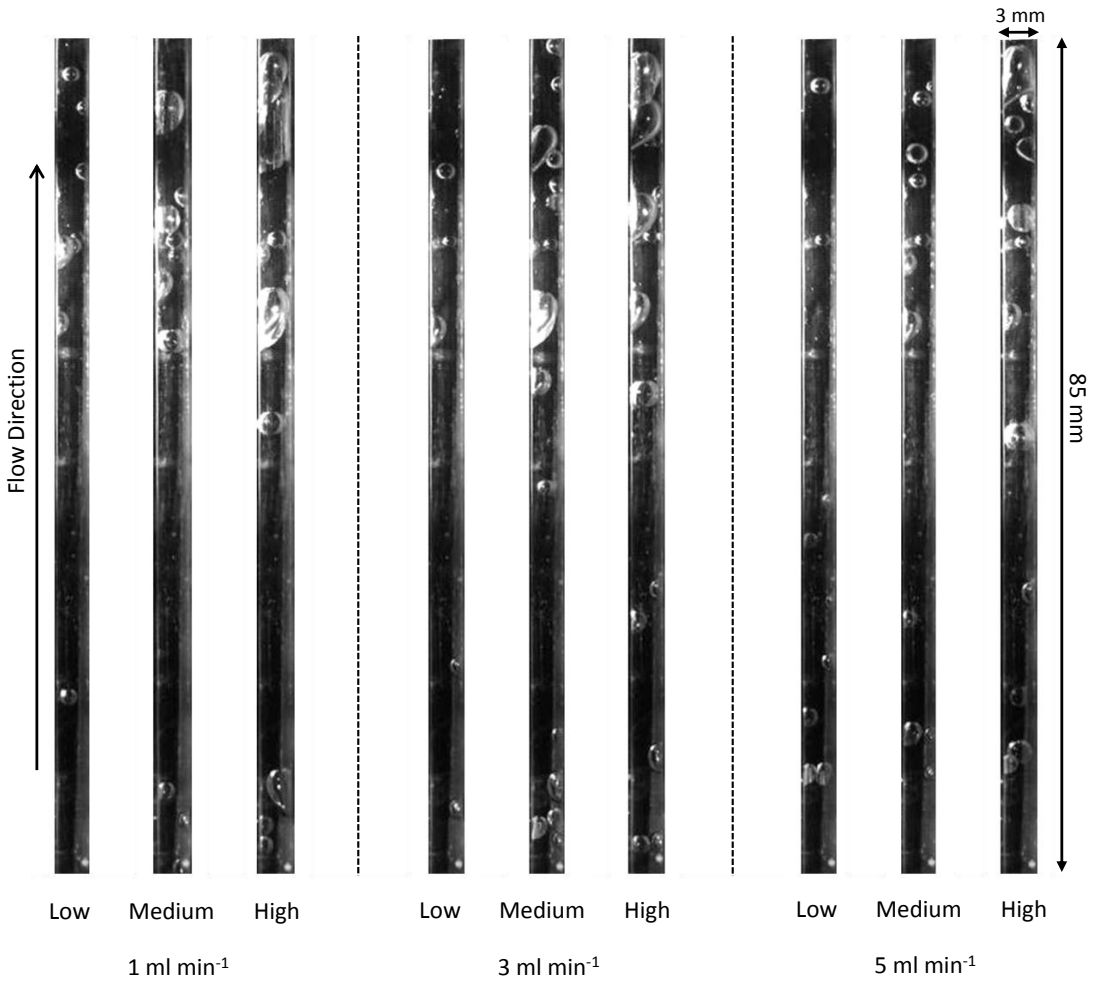

Figure 62: Two-phase flow profiles of the anode of the electrolyser cell when operating under Low, Medium and High potentials and water flow rates of 1 ml min^{-1}, 3 ml min^{-1} and 5 ml min^{-1}.

Furthermore, the visualisation shows a decrease in bubble size with increasing water flow rate at a constant operating potential and can be explained by the natural decrease in void fraction with increasing liquid flow rate. To explore the effect of increasing operating potential and water flow rate on bubble size and shape, images of bubbles under the operating conditions considered were obtained at Segment 7 and analysed. It was observed that larger bubbles had a high tendency to coalesce with smaller bubbles to form clusters. In these cases, the total volumes of the bubble clusters were calculated in order to find the equivalent diameter. Close-up images of the two generic types of bubbles seen in

the flow channel are shown in Figure 63. The mean bubble diameter and length values obtained by averaging 10 samples are given in Table 12.

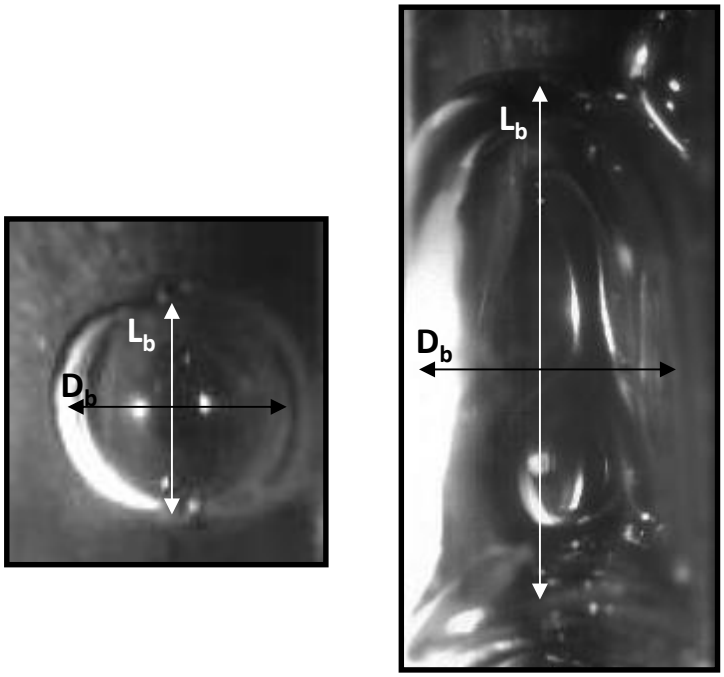

Figure 63: Close-up of two types of bubbles observed in the electrolyser flow channel showing: (a) diameter measurement of spherical-type bubble and (b) length of slug-type (deformed) bubble.

Table 12: Mean diameter and length of bubbles observed at Low, Medium and High operating potentials and water flow rates of 1 ml min^{-1}, 3 ml min^{-1} and 5 ml min^{-1}.

Potential	1 ml min^{-1}		3 ml min^{-1}		5 ml min^{-1}	
	D_b (mm)	$\frac{D_b}{l_b}$	D_b (mm)	$\frac{D_b}{l_b}$	D_b (mm)	$\frac{D_b}{l_b}$
Low	1.51	1.02	1.40	1.01	1.21	1.00
Medium	1.67	1.01	1.64	1.01	1.53	1.01
High	2.03	0.85	1.99	0.87	1.97	0.80

It can be seen that the ratio of bubble diameter to bubble length has a value of ~1 at low and medium potentials for all flow rates. The mean bubble diameter (at Segment 7) increases from Low to Medium operating potentials and approaches a critical value after which it deforms and starts growing vertically, indicating a transition from bubbly to slug flow. For Low and Medium conditions, increasing flow rate leads to a smaller average bubble diameter as would be expected due to the lower void fraction of gas bubbles caused by higher liquid water flow rate.

Previous studies [150, 198] as discussed in Sections 5.2.3 and 5.3.5 have shown that transition from bubbly to slug flow (based on whole cell analysis) enhances the mass transport in an electrolyser and hence results in better performance [150, 195-197]. Figure 62 shows that the gas void fraction in the flow channels increase with operating potential and decreasing water flow rate. Section 5.2.3 discusses the influence of the void fraction on the mass transport coefficient, which states the it has an inverse relationship [186, 198]. This phenomena discussed in the previous section was observed in our experiments as shown in Figure 64.

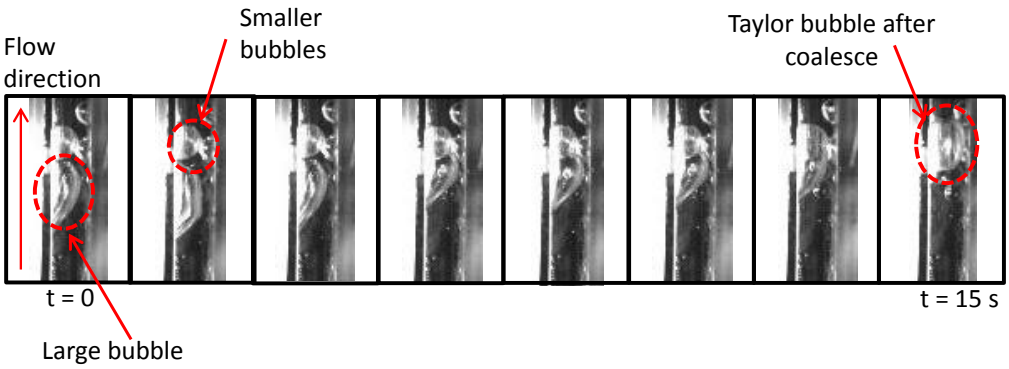

Figure 64: The sweeping effect of a Taylor bubble rising up the electrolyser channel.

A rising bubble in an electrolyser channel displaces water creating a transverse motion of water that sweeps bubble off the electrode surface. Bigger bubbles create a greater turbulence of water (as shown in Figure 44) that has a higher effect on the displacement of smaller bubbles on the electrode surface thus increases the mass transport of the system. Furthermore, as observed in our study (shown in Figure 64), Taylor bubbles (slug flow) have a high tendency to coalescence with smaller bubbles and remove them from the electrode surface while moving up the electrolyser channel. Therefore, it follows that local transition from bubbly to slug flow can be attributed to the increase in mass transport that results in an increase in current density along the channel.

5.4.4. Conclusion

The combination of localised current density mapping and flow visualisation in a PEMWE has been demonstrated for the first time. Pt / Ru ink synthesised to prepare segmented MEA for current mapping measurements showed stable performance.

CDD measurements showed an increase in current density toward the end of the channel where slug flow was observed in the operating conditions considered. The current density variation along the channel reduced with increasing water flow rates. Bubble size measurements made indicated slug flow at high operating potentials. Coalescence between slug bubbles and smaller bubbles was observed. Slug flow enhances mass transport which gives higher performance closer to the outlet of the channel.

6. Overall Conclusion

The literature review carried out on PEMWE technology has shown that it has many advantages over the traditional alkaline electrolysis and plays an important role in the 'hydrogen economy'. Influence of the operating temperature and pressure on the PEMWE cell performance is present in literature. Diagnostic techniques discussed in the literature review are widely applied in PEMFC systems and require further development to be used in PEMWE systems. Currently, there is very little work present in literature that studies the effect of operating water flow rate on a PEMWE performance.

The mathematical model developed showed that the operating potential of a PEMWE is dominated by the anode activation overpotential. The ohmic overpotential had a significant effect on the cell potential at higher current densities whereas the cathode overpotential played an insignificant role due to fast HER kinetics. The sensitivity analysis carried out indicated that the anode charge transfer coefficient, anode exchange current density and the diffusivity of protons had a large impact on the performance of the electrolyser. The model displayed a good fit with experimental data obtained at identical conditions confirming the accuracy of the model. The fitted parameter values were close to values assumed and were within the rage reported in literature.

Polarisation measurements carried out on a lab scale commercial cell agreed well with data provided by Proton OnSite, CT, USA. Polarisation curves obtained at different water flow rates showed a voltage jump at high current densities with increasing water flow rate. Impedance measurements made on the cell at water flow rates considered at different operating potentials showed an increase in mass transport limitations with increasing water flow rate. Theoretical calculations indicated that the flow is in bubbly region throughout the current density region considered. Increase in gas void fraction that leads to bigger gas bubbles reduces mass transport limitations that improve the performance of the cell.

Engineering measurements made on the optical cell showed stable performance of the system. Thermal imaging work done on the cell showed an increase in cell temperature with increasing current density that pointed to performance improvement due to improved membrane resistance. The transparent PEMWE constructed using PCB technology allowed optical access to the cell middle channel that permitted two-phase flow phenomena to be observed. It was seen that the bubbles moving up the flow field channels grew in size with increasing current density indicating increase in gas void fraction and a transition from bubbly to slug flow was also observed at higher current densities. However, the opposite was observed with increasing water flow rate. Transition from bubbly to slug flow enhances mass transport in the electrolyser.

The optical cell developed with a segmented MEA allowed CDD measurements to be carried out along the electrolyser channel that consisted of 8 segments and the optical window permitted the two phase flow patterns present at each operating condition to be observed. The current density increased up the channel (moving towards the exit) and the highest current density was observed at the segment closest to the exit. The difference between the current densities observed across each segment decreased with increasing water flow rate. The size of bubbles increased with increasing operating potential as expected due to greater gas generation at higher potentials. Furthermore, it was observed that the size of the bubbles increased along the channel forming Taylor bubbles toward the exit of the channel that explains the improved performance of the segments closer to the exit.

Two-phase flow observations indicate that the size of gas bubbles increase with increasing current but decrease with increasing water flow rate due to decrease in gas void fraction. Bigger gas bubbles and Taylor bubbles seen in slug flow region, enhance mass transport of the cell, improving its performance. Larger bubbles create a greater turbulence in the liquid water when rising up the channel that sweeps smaller bubbles off the electrode surface, increasing the mass transport of the cell. Furthermore, bigger bubbles (including Taylor bubbles) moving up a

channel have a higher tendency to coalescence with smaller bubbles removing them from the electrode surface, which results in increased mass transport.

Overall project goals are accomplished as the results obtained from *in situ* measurements provide a detailed description of a PEMWE behaviour under different operating conditions and losses associated with the system. Visualisation work carried out displays the influence of water flow rate on the cell performance.

To date, there are no studies present in literature that use direct optical visualisation, current mapping or a combination of the two techniques to study the internal workings of a PEMWE. This study employs these techniques to understand the influence of operating water flow rate on the performance of an electrolyser and to analyse the distribution of current along an electrolysis cell. This thesis makes a valuable contribution to science, as the novel findings in this study develop a relationship between the cell performance and the operating flow regime. Further, CDD along a cell channel is explained using direct optical visualisation which has been previously unpublished.

6.1. Future Work

Although this project has been very successful in achieving the set project goals, there are still many areas of interest in PEMWE technology that need to be addressed in order have a better understanding of the technology.

This study focuses on the performance of a PEMWE operating at ambient conditions. It can be extended further to execute measurements at high operating pressures in order to replicate real PEMWE systems and to understand the effect operating pressure on the performance of the system.

This project looks at the influence of water flow rate on the system performance at different current densities. A wider range of current densities and flow rates should be considered to get a deeper understanding of this effect. Performing these experiments under controlled conditions, assuring constant temperature and pressure will give a better understanding of the effect of water flow rate. Furthermore, it will be interesting to observe if the water flow rate has the same influence as seen in this study, on the cell performance when the temperature of feed water is altered. Water can be circulated on the cathode side to determine if it improves the cell performance and if the flow rate of water circulation has a similar effect as seen on the anode side.

The anode flow field plates considered in this study consist of parallel flow channels. It will be important to study the influence of the flow design and channel dimensions on the performance of the cell and the influence of two phase flow regimes for each flow design. The orientation of the channel could be varied as it will have an effect on the bubble flow in the flow channels to optimize the cell position for better performance.

EIS measurements obtained in this study at lower frequencies displayed a lot of noise associated with the system; therefore, more sensitive measurements of

impedance at these frequencies will give a better understanding of mass transport limitations associated with the system.

Optical visualisation work done in this study focuses on the flow regimes that are present in a PEM electrolyser cell channel. The project can be further improved by carrying out an in depth study of the bubble formation and detachment mechanism from the electrode surface to understand the characteristics of the bubble electrode interface. Furthermore, the effect of materials used in the system on bubble and flow dynamics can be studied by measuring contact angles between the bubble and the surface.

Repeating current mapping experiments carried out in this study with a combination of thermal imaging will give a better understanding of the current distribution across the cell and the influence of temperature on it. Further, CDD measurements on different cell designs will allow to understand the effect of flow field design on current distribution in a PEMWE. Cell orientation could also be changed to observe if it changes the CDD pattern drastically.

The model developed in this study only considers activation and ohmic overpotentials on the performance of an electrolysis cell. This model can be improved further to take mass transport losses into account as it will help to predict the influence of water flow rate on the electrolyser performance. The model can be developed further to predict the system performance based on flow field designs using CFD packages such as Comsol Multiphysics.

7. Nomenclature

α	Charge transfer coefficient
a_{H_2O}	Activity of water
α_v	Void fraction
β	Symmetric coefficient
γ	Surface tension of the interface, N m^{-1}
δ_e	Thickness of the electrode, m
δ_m	Membrane thickness, m
ε	Porosity of the electrode
ζ	The ratio between the amount of circulating water to the amount of water required
η	Overpotential, V
θ	Contact angle
ι	Length of the electrons path, m
λ	Water content
μ	Dynamic viscosity of water, Pa s
ρ	Density, kg m^{-3}
ρ_P	Resistivity of the current collection plate, ohm m
ρ_{bulk}	Bulk resistivity of the electrode, ohm m
ρ_{eff}	Effective resistivity of the electrode, ohm m
$\rho_{m,dry}$	Density of the dry membrane, kg m^{-3}
σ_m	Conductivity of the membrane, S m^{-1}
x	Quality of the two-phase flow
x_{H_2O}	Mole fraction of water

A	Surface area, m^2
A_{ch}	Cross sectional area of a channel, m^2
A_p	Projected area of the droplet, m^2
Bo	Bond number
C_{H^+}	Concentration of H^+ ions, mol m^{-3}

C_1	Ratio of maximum to mean velocity (≈ 1.2)
C_{MC}	Added mass coefficient
C_i	Concentration of component i, mol m^{-3}
$C_{p,i}$	Specific heat capacity of component i, J g^{-1} K^{-1}
D	Hydraulic diameter of the channel, m
D_{H^+}	Protonic diffusion coefficient, m^2 s^{-1}
D_e	Equi-periphery diameter, m
D_{eff}	Effective water diffusion coefficient
D_w	Diffusion coefficient of water
E°	Equilibrium cell voltage, V
E_{TN}	Thermoneutral voltage, V
E_{an}	Anode voltage, V
E_{cat}	Cathode voltage, V
E_{cell}	Cell voltage, V
E_{loss}	Voltage loss, V
F	Faraday constant, 96486 C mol^{-1}
F_B	Buoyancy force, N
G	Mass flux, kg m^{-2}
ΔG	Gibbs free energy change, J
g	Gravitational acceleration,9.81 m s^{-2}
H	Heating value, kJ mol^{-1}
ΔH	Enthalpy of the reaction, J
h_c	Height of the channel, m
h_p	Distance from the outside border of the plate to the channel surface, m
I	Current, A
$I_{Faradaic}$	Faradaic charge, C s^{-1}
$I_{Overall}$	Overall current, C s^{-1}
i	Current density, A cm^{-2}
i_0	Exchange current density, A cm^{-2}
$i_{0,an}^0$	Anode reference exchange current density, A cm^{-2}

$i_{0,cat}^{0}$	Cathode reference exchange current density, A cm^{-2}
j_g	Superficial gas velocity, m s^{-1}
j_l	Superficial liquid velocity, m s^{-1}
k	Reaction rate coefficient, s^{-1}
L	Length of the electrode / plate, m
l_b	Length of bubble, m
mw	Molecular weight, g mol^{-1}
$M_{m,dry}$	Equivalent weight of a dry membrane, kg
$\dot{m}_i$	Mass flow rate of component i, g s^{-1}
$\dot{N}_i$	Molar rate of component i, mol s^{-1}
n_{ch}	Number of channels
n_d	Electro-osmotic drag coefficient
P	Wetted perimeter of the channel, m
P_{H_2}	Partial pressures of hydrogen, Pa
P_{O_2}	Partial pressure of oxygen, Pa
P_{sat}	Saturation pressure, Pa
Q	Heat transferred, J
$\dot{Q}$	Flow rate of heat, W
R	Resistance, ohm
R	Universal gas constant, 8.314 J $mol^{-1}K^{-1}$
Re	Reynolds number
R_0	Radius of the gas nozzle, m
R_b	Radius of the bubble, m
ΔS	Entropy change, J K^{-1}
T	Temperature, K
T_0	Reference temperature, 298.15 K
t	Time, s
u_g	Gas velocity, m s^{-1}
u_{go}	Velocity in the stagnant water column, m s^{-1}
u_l	Velocity of water, m s^{-1}
V_b	Volume of the bubble, m

V_l	Liquid velocity, m s^{-1}
$\dot{V}_{H_2}$	Hydrogen production rate per unit volume, m^3
W	Width of the plate, m
W_{H_2}	Chemical energy generated, J
W_{el}	Electric work, J
w_c	Width of channel, m
w_s	Width of channel support, m
$\frac{ds}{dt}$	Velocity of the bubble center

an	Anode
b	Bubbles
cat	Cathode
CCM	Catalyst coated membrane
CDD	Current density distribution
DAQ	Data acquisition board
DC	Direct current
DI	Deionised
DoE	Department of Energy (U.S.)
EIS	Electrochemical impedance spectroscopy
GDL	Gas diffusion layer
HER	Hydrogen evolution reaction
HHV	Higher heating value, kJ mol^{-1}
HPA	Heteropolyacid
LHV	Lower heating value, kJ mol^{-1}
m	Membrane
MEA	Membrane electrode assembly
MPL	Micro porous layer
n	Number of electrons
OCV	Open circuit voltage
OER	Oxygen evolution reaction

PCB	Printed circuit board
PEM	Proton exchange membrane / polymer electrolyte membrane
PEMFC	PEM fuel cell
PEMWE	Proton exchange membrane water electrolyser
PES	Polyether sulfone
P&ID	piping and instrumentation diagram
PSF	Polysulfone
Rds	Rate Determining Step
^{r}	Reaction order
SOEC	Solid oxide electrolysis cells
SPE	Solid polymer electrolyte
SPEEK	Sulfonated polyether ether ketone
VI	Virtual interface

8. References

[1] McDowall W, Eames M. Towards a sustainable hydrogen economy: A multi-criteria sustainability appraisal of competing hydrogen futures. International Journal of Hydrogen Energy. 2007;32:4611-26.

[2] Zeng K, Zhang D. Recent progress in alkaline water electrolysis for hydrogen production and applications. Progress in Energy and Combustion Science. 2010;36:307-26.

[3] Andrews J, Shabani B. Re-envisioning the role of hydrogen in a sustainable energy economy. International Journal of Hydrogen Energy. 2012;37:1184-203.

[4] Berry GD. Hydrogen Production. In: Editor-in-Chief: Cutler JC, editor. Encyclopedia of Energy. New York: Elsevier; 2004. p. 253-65.

[5] Lattin WC, Utgikar VP. Transition to hydrogen economy in the United States: A 2006 status report. International Journal of Hydrogen Energy. 2007;32:3230-7.

[6] Holladay JD, Hu J, King DL, Wang Y. An overview of hydrogen production technologies. Catalysis Today. 2009;139:244-60.

[7] Barbir F. PEM electrolysis for production of hydrogen from renewable energy sources. Solar Energy. 2005;78:661-9.

[8] Lu PWT, Srinivasan S. Advances in water electrolysis technology with emphasis on use of the solid polymer electrolyte. Journal of Applied Electrochemistry. 1979;9:269-83.

[9] Wang M, Wang Z, Gong X, Guo Z. The intensification technologies to water electrolysis for hydrogen production – A review. Renewable and Sustainable Energy Reviews. 2014;29:573-88.

[10] Manage MN, Hodgson D, Milligan N, Simons SJR, Brett DJL. A techno-economic appraisal of hydrogen generation and the case for solid oxide electrolyser cells. International Journal of Hydrogen Energy. 2011;36:5782-96.

[11] Ni M, Leung MKH, Leung DYC. Technological development of hydrogen production by solid oxide electrolyzer cell (SOEC). International Journal of Hydrogen Energy. 2008;33:2337-54.

[12] Nieminen J, Dincer I, Naterer G. Comparative performance analysis of PEM and solid oxide steam electrolysers. International Journal of Hydrogen Energy. 2010;35:10842-50.

[13] Nehrir H, Wang C. Modeling and Control of Fuel Cells: Distributed Generation Applications: Wiley; 2009.

[14] Ganley JC. High temperature and pressure alkaline electrolysis. International Journal of Hydrogen Energy. 2009;34:3604-11.

[15] Millet P, Dragoe D, Grigoriev S, Fateev V, Etievant C. GenHyPEM: A research program on PEM water electrolysis supported by the European Commission. International Journal of Hydrogen Energy. 2009;34:4974-82.

[16] McElroy JF. Recent advances in SPE® water electrolyzer. Journal of Power Sources. 1994;47:369-75.

[17] Hydrogen energy and fuel cells. A vision for our future. Brussels: European commission; 2003.

[18] Millet P, Ngameni R, Grigoriev SA, Mbemba N, Brisset F, Ranjbari A, et al. PEM water electrolyzers: From electrocatalysis to stack development. International Journal of Hydrogen Energy. 2010;35:5043-52.
[19] Millet P, Andolfatto F, Durand R. Design and performance of a solid polymer electrolyte water electrolyzer. International Journal of Hydrogen Energy. 1996;21:87-93.
[20] Labou D, Slavcheva E, Schnakenberg U, Neophytides S. Performance of laboratory polymer electrolyte membrane hydrogen generator with sputtered iridium oxide anode. Journal of Power Sources. 2008;185:1073-8.
[21] Grigoriev SA, Porembsky VI, Fateev VN. Pure hydrogen production by PEM electrolysis for hydrogen energy. International Journal of Hydrogen Energy. 2006;31:171-5.
[22] Doucet G, Etiévant C, Puyenchet C, Grigoriev S, Millet P. Hydrogen-based PEM auxiliary power unit. International Journal of Hydrogen Energy. 2009;34:4983-9.
[23] Millet P, Alleau T, Durand R. Characterization of membrane-electrode assemblies for solid polymer electrolyte water electrolysis. Journal of Applied Electrochemistry. 1993;23:322-31.
[24] Ayers KE, Anderson EB, Capuano C, Carter B, Dalton L, Hanlon G, et al. Research Advances towards Low Cost, High Efficiency PEM Electrolysis. ECS Transactions. 2010;33:3-15.
[25] Carmo M, Fritz DL, Mergel J, Stolten D. A comprehensive review on PEM water electrolysis. International Journal of Hydrogen Energy. 2013;38:4901-34.
[26] Hamdan M, Norman T. PEM Electrolyzer Incorporating an Advanced Low-Cost Membrane. DOE Hydrogen and Fuel Cells Program. FY 2012 Annual Progress Report ed2012. p. II-31 - II-4.
[27] Ayers KE, Roemer A. High Performance, Low Cost Hydrogen Generation from Renewable Energy. DOE Hydrogen and Fuel Cells Program. FY 2012 annual progress report ed2012. p. II-35 - II-8.
[28] Multi-Year Research, Development and Demonstration Plan. Hydrogen Production. 2011 (interim Update). p. 3.1-14.
[29] Lessing P. Materials for hydrogen generation via water electrolysis. Journal of Materials Science. 2007;42:3477-87.
[30] Wang Y, Chen KS, Mishler J, Cho SC, Adroher XC. A review of polymer electrolyte membrane fuel cells: Technology, applications, and needs on fundamental research. Applied Energy. 2011;88:981-1007.
[31] Lwin MZ, Oo MM. Construction of Water Electrolyzer for Single Slice O2/H2 Polymer Electrolyte Membrane Fuel Cell. World Academy of Science, Engineering and Technology. 2008 24:273-6.
[32] Choi P, Bessarabov DG, Datta R. A simple model for solid polymer electrolyte (SPE) water electrolysis. Solid State Ionics. 2004;175:535-9.
[33] Millet P, Ngameni R, Grigoriev SA, Fateev VN. Scientific and engineering issues related to PEM technology: Water electrolysers, fuel cells and unitized regenerative systems. International Journal of Hydrogen Energy. 2011;36:4156-63.
[34] Wei G, Xu L, Huang C, Wang Y. SPE water electrolysis with SPEEK/PES blend membrane. International Journal of Hydrogen Energy. 2010;35:7778-83.
[35] Jang I-Y, Kweon O-H, Kim K-E, Hwang G-J, Moon S-B, Kang A-S. Application of polysulfone (PSf)– and polyether ether ketone (PEEK)–tungstophosphoric acid

(TPA) composite membranes for water electrolysis. Journal of Membrane Science. 2008;322:154-61.
[36] Woo J-Y, Lee K-M, Jee B-C, Ryu C-H, Yoon C-H, Chung J-H, et al. Electrocatalytic characteristics of Pt–Ru–Co and Pt–Ru–Ni based on covalently cross-linked sulfonated poly(ether ether ketone)/heteropolyacids composite membranes for water electrolysis. Journal of Industrial and Engineering Chemistry. 2010;16:688-97.
[37] Shidong S, Huamin Z, Bo LIU, Ping Z, Yining Z, Baolian YI. An improved catalyst-coated membrane structure for PEM water electrolyzer. Electrochemical and solid-state letters. 2007;10.
[38] Song S, Zhang H, Ma X, Shao Z, Baker RT, Yi B. Electrochemical investigation of electrocatalysts for the oxygen evolution reaction in PEM water electrolyzers. International Journal of Hydrogen Energy. 2008;33:4955-61.
[39] Millet P. Water electrolysis using eme technology: electric potential distribution inside a nafion membrane during electrolysis. Electrochimica Acta. 1994;39:2501-6.
[40] Andolfatto F, Durand R, Michas A, Millet P, Stevens P. Solid polymer electrolyte water electrolysis: electrocatalysis and long-term stability. International Journal of Hydrogen Energy. 1994;19:421-7.
[41] Rasten E, Hagen G, Tunold R. Electrocatalysis in water electrolysis with solid polymer electrolyte. Electrochimica Acta. 2003;48:3945-52.
[42] Trasatti S. Electrocatalysis in the anodic evolution of oxygen and chlorine. Electrochimica Acta. 1984;29:1503-12.
[43] Millet P, Mbemba N, Grigoriev SA, Fateev VN, Aukauloo A, Etiévant C. Electrochemical performances of PEM water electrolysis cells and perspectives. International Journal of Hydrogen Energy. 2011;36:4134-42.
[44] Marshall A, Børresen B, Hagen G, Tsypkin M, Tunold R. Hydrogen production by advanced proton exchange membrane (PEM) water electrolysers—Reduced energy consumption by improved electrocatalysis. Energy. 2007;32:431-6.
[45] Morimitsu M, Otogawa R, Matsunaga M. Effects of cathodizing on the morphology and composition of IrO2-Ta2O5/Ti anodes. Electrochimica Acta. 2000;46:401-6.
[46] Hu JM, Meng HM, Zhang JQ, Cao CN. Degradation mechanism of long service life Ti/IrO2–Ta2O5 oxide anodes in sulphuric acid. Corrosion Science. 2002;44:1655-68.
[47] Marshall AT, Sunde S, Tsypkin M, Tunold R. Performance of a PEM water electrolysis cell using electrocatalysts for the oxygen evolution electrode. International Journal of Hydrogen Energy. 2007;32:2320-4.
[48] Terezo AJ, Bisquert J, Pereira EC, Garcia-Belmonte G. Separation of transport, charge storage and reaction processes of porous electrocatalytic IrO2 and IrO2/Nb2O5 electrodes. Journal of Electroanalytical Chemistry. 2001;508:59-69.
[49] Mayousse E, Maillard F, Fouda-Onana F, Sicardy O, Guillet N. Synthesis and characterization of electrocatalysts for the oxygen evolution in PEM water electrolysis. International Journal of Hydrogen Energy. 2011;36:10474-81.
[50] Grigoriev SA, Millet P, Fateev VN. Evaluation of carbon-supported Pt and Pd nanoparticles for the hydrogen evolution reaction in PEM water electrolysers. Journal of Power Sources. 2008;177:281-5.

[51] Pantani O, Naskar S, Guillot R, Millet P, Anxolabéhère-Mallart E, Aukauloo A. Cobalt Clathrochelate Complexes as Hydrogen-Producing Catalysts. Angewandte Chemie International Edition. 2008;47:9948-50.
[52] Pantani O, Anxolabéhère-Mallart E, Aukauloo A, Millet P. Electroactivity of cobalt and nickel glyoximes with regard to the electro-reduction of protons into molecular hydrogen in acidic media. Electrochemistry Communications. 2007;9:54-8.
[53] Miles MH, Thomason MA. Periodic Variations of Overvoltages for Water Electrolysis in Acid Solutions from Cyclic Voltammetric Studies. Journal of The Electrochemical Society. 1976;123:1459-61.
[54] Grigoriev SA, Millet P, Volobuev SA, Fateev VN. Optimization of porous current collectors for PEM water electrolysers. International Journal of Hydrogen Energy. 2009;34:4968-73.
[55] Pettersson J, Ramsey B, Harrison D. A review of the latest developments in electrodes for unitised regenerative polymer electrolyte fuel cells. Journal of Power Sources. 2006;157:28-34.
[56] O'Hayre R, Braithwaite D, Hermann W, Lee S-J, Fabian T, Cha S-W, et al. Development of portable fuel cell arrays with printed-circuit technology. Journal of Power Sources. 2003;124:459-72.
[57] Daniels FA, Attingre C, Kucernak AR, Brett DJL. Current Collector Design for Closed-Plenum Polymer Electrolyte Membrane Fuel Cells. Journal of Power Sources.
[58] Cleghorn SJC, Derouin CR, Wilson MS, Gottesfeld S. A printed circuit board approach to measuring current distribution in a fuel cell. Journal of Applied Electrochemistry. 1998;28:663-72.
[59] Brett DJL, Atkins S, Brandon NP, Vasileiadis N, Vesovic V, Kucernak AR. Membrane resistance and current distribution measurements under various operating conditions in a polymer electrolyte fuel cell. Journal of Power Sources. 2007;172:2-13.
[60] Brett DJL, Atkins S, Brandon NP, Vesovic V, Vasileiadis N, Kucernak AR. Measurement of the current distribution along a single flow channel of a solid polymer fuel cell. Electrochemistry Communications. 2001;3:628-32.
[61] Nishikawa H, Kurihara R, Sukemori S, Sugawara T, Kobayasi H, Abe S, et al. Measurements of humidity and current distribution in a PEFC. Journal of Power Sources. 2006;155:213-8.
[62] Schmitz A, Wagner S, Hahn R, Uzun H, Hebling C. Stability of planar PEMFC in Printed Circuit Board technology. Journal of Power Sources. 2004;127:197-205.
[63] Oi T, Sakaki Y. Optimum hydrogen generation capacity and current density of the PEM-type water electrolyzer operated only during the off-peak period of electricity demand. Journal of Power Sources. 2004;129:229-37.
[64] Deschampsa A, Etievanta C, Fateevb V, Grigorievb S, Kalinnikovb A, Milletc P, et al. Development of advanced PEM water electrolysers. World Hydrogen Energy Conference. Lyon France2006.
[65] Ma L, Sui S, Zhai Y. Investigations on high performance proton exchange membrane water electrolyzer. International Journal of Hydrogen Energy. 2009;34:678-84.

[66] Grigoriev SA, Porembskiy VI, Korobtsev SV, Fateev VN, Auprêtre F, Millet P. High-pressure PEM water electrolysis and corresponding safety issues. International Journal of Hydrogen Energy. 2011;36:2721-8.
[67] Santarelli M, Medina P, Calì M. Fitting regression model and experimental validation for a high-pressure PEM electrolyzer. International Journal of Hydrogen Energy. 2009;34:2519-30.
[68] Zhang H, Su S, Lin G, Chen J. Efficiency calculation and configuration design of a PEM electrolyzer system for hydrogen production. International Journal of Electrochemical Science. 2012;7:4143-57.
[69] Ito H, Maeda T, Nakano A, Hasegawa Y, Yokoi N, Hwang CM, et al. Effect of flow regime of circulating water on a proton exchange membrane electrolyzer. International Journal of Hydrogen Energy. 2010;35:9550-60.
[70] Balaji R, Senthil N, Vasudevan S, Ravichandran S, Mohan S, Sozhan G, et al. Development and performance evaluation of Proton Exchange Membrane (PEM) based hydrogen generator for portable applications. International Journal of Hydrogen Energy. 2011;36:1399-403.
[71] Smith JM, Van Ness HC, Abbot M. Introduction to chemical engineering thermodynamics. 7th ed. New York: McGraw-Hill Education; 2005.
[72] Pletcher D, Walsh FC. Industrial electrochemistry. second ediion ed. New York: Chapman and Hall; 1990.
[73] Hydrogen and fuel cells: fundamentals, technologies and applications. weinheim: WILEY-VCH; 2010.
[74] Larminie J, Dicks A. Fuel Cell Systems Explained (2nd Edition). John Wiley & Sons.
[75] Laoun B. Thermodynamics aspect of high pressure hydrogen production by water electrolysis. Revue des Energies Renouvelables. 2007;10:3.
[76] Li X. Principles Of Fuel Cells: Taylor & Francis Group; 2005.
[77] Alvensleben DLv. PHYWE: Experimental literature. Laboratory experiments.
[78] Monk PMS. Fundamentals of Electro-Analytical Chemistry 1st ed. England: John Wiley & Sons, Ltd.; 2001.
[79] Frank W. A first course in electrochemical engineering. England: Alfresford Press Ltd.,; 1993.
[80] Laoun B, Belhamel M, Naceur W, Serir L. Electrochemical aided model to study solid polymer electrolyte water electrolysis. Revue des Energies Renouvelables. 2008;11:267-76.
[81] Peng J, Lee SJ. Numerical simulation of proton exchange membrane fuel cells at high operating temperature. Journal of Power Sources. 2006;162:1182-91.
[82] Noren DA, Hoffman MA. Clarifying the Butler–Volmer equation and related approximations for calculating activation losses in solid oxide fuel cell models. Journal of Power Sources. 2005;152:175-81.
[83] Mench MM. Fuel cell engines. New Jersey: John Wiley & Sons, Inc.; 2008.
[84] Wu J, Yuan XZ, Wang H, Blanco M, Martin JJ, Zhang J. Diagnostic tools in PEM fuel cell research: Part I Electrochemical techniques. International Journal of Hydrogen Energy. 2008;33:1735-46.
[85] Yuan X, Sun JC, Blanco M, Wang H, Zhang J, Wilkinson DP. AC impedance diagnosis of a 500 W PEM fuel cell stack: Part I: Stack impedance. Journal of Power Sources. 2006;161:920-8.

[86] Brunetto C, Moschetto A, Tina G. PEM fuel cell testing by electrochemical impedance spectroscopy. Electric Power Systems Research. 2009;79:17-26.
[87] Yuan XZ, Song C, Wang H, Zhang J. Electrochemical Impedance Spectroscopy in PEM Fuel Cells. London: Springer; 2010.
[88] Gomadam PM, Weidner JW. Analysis of electrochemical impedance spectroscopy in proton exchange membrane fuel cells. International Journal of Energy Research. 2005;29:1133-51.
[89] Chen G, Zhang H, Cheng J, Ma Y, Zhong H. A novel membrane electrode assembly for improving the efficiency of the unitized regenerative fuel cell. Electrochemistry Communications. 2008;10:1373-6.
[90] Bultel Y, Wiezell K, Jaouen F, Ozil P, Lindbergh G. Investigation of mass transport in gas diffusion layer at the air cathode of a PEMFC. Electrochimica Acta. 2005;51:474-88.
[91] Ciureanu M, Mikhailenko SD, Kaliaguine S. PEM fuel cells as membrane reactors: kinetic analysis by impedance spectroscopy. Catalysis Today. 2003;82:195-206.
[92] Yuan X, Wang H, Colin Sun J, Zhang J. AC impedance technique in PEM fuel cell diagnosis—A review. International Journal of Hydrogen Energy. 2007;32:4365-80.
[93] Siracusano S, Baglio V, Briguglio N, Brunaccini G, Di Blasi A, Stassi A, et al. An electrochemical study of a PEM stack for water electrolysis. International Journal of Hydrogen Energy. 2012;37:1939-46.
[94] Pérez LC, Brandão L, Sousa JM, Mendes A. Segmented polymer electrolyte membrane fuel cells—A review. Renewable and Sustainable Energy Reviews. 2011;15:169-85.
[95] Stumper J, Campbell SA, Wilkinson DP, Johnson MC, Davis M. In-situ methods for the determination of current distributions in PEM fuel cells. Electrochimica Acta. 1998;43:3773-83.
[96] Liu Z, Mao Z, Wu B, Wang L, Schmidt VM. Current density distribution in PEFC. Journal of Power Sources. 2005;141:205-10.
[97] Sun H, Zhang G, Guo L-J, Liu H. A novel technique for measuring current distributions in PEM fuel cells. Journal of Power Sources. 2006;158:326-32.
[98] Sun H, Zhang G, Guo L, Liu H. A Study of dynamic characteristics of PEM fuel cells by measuring local currents. International Journal of Hydrogen Energy. 2009;34:5529-36.
[99] Mench MM, Wang CY, Ishikawa M. In Situ Current Distribution Measurements in Polymer Electrolyte Fuel Cells. Journal of The Electrochemical Society. 2003;150:A1052-A9.
[100] Hsieh S-S, Huang Y-J. Measurements of current and water distribution for a micro-PEM fuel cell with different flow fields. Journal of Power Sources. 2008;183:193-204.
[101] Rajalakshmi N, Raja M, Dhathathreyan KS. Evaluation of current distribution in a proton exchange membrane fuel cell by segmented cell approach. Journal of Power Sources. 2002;112:331-6.
[102] Mench MM, Wang CY. An In Situ Method for Determination of Current Distribution in PEM Fuel Cells Applied to a Direct Methanol Fuel Cell. Journal of The Electrochemical Society. 2003;150:A79-A85.

[103] Hwnag JJ, Chang WR, Peng RG, Chen PY, Su A. Experimental and numerical studies of local current mapping on a PEM fuel cell. International Journal of Hydrogen Energy. 2008;33:5718-27.
[104] Lin R, Sander H, Gülzow E, Friedrich A. Investigation of Locally Resolved Current Density Distribution of Segmented PEM Fuel Cells to Detect Malfunctions. ECS Transactions. 2010;26:229-36.
[105] Geske M, Heuer M, Heideck G, Styczynski ZA. Current Density Distribution Mapping in PEM Fuel Cells as An Instrument for Operational Measurements. Energies. 2010;3:770-83.
[106] Matsushima H, Nishida T, Konishi Y, Fukunaka Y, Ito Y, Kuribayashi K. Water electrolysis under microgravity: Part 1. Experimental technique. Electrochimica Acta. 2003;48:4119-25.
[107] Bazylak A. Liquid water visualization in PEM fuel cells: A review. International Journal of Hydrogen Energy. 2009;34:3845-57.
[108] Ji M, Wei Z. A Review of Water Management in Polymer Electrolyte Membrane Fuel Cells. Energies. 2009;2:1057-106.
[109] Ous T, Arcoumanis C. Visualisation of water accumulation in the flow channels of PEMFC under various operating conditions. Journal of Power Sources. 2009;187:182-9.
[110] Ous T, Arcoumanis C. Visualisation of water droplets during the operation of PEM fuel cells. Journal of Power Sources. 2007;173:137-48.
[111] Ous T, Arcoumanis C. The formation of water droplets in an air-breathing PEMFC. International Journal of Hydrogen Energy. 2009;34:3476-87.
[112] Theodorakakos A, Ous T, Gavaises M, Nouri JM, Nikolopoulos N, Yanagihara H. Dynamics of water droplets detached from porous surfaces of relevance to PEM fuel cells. Journal of Colloid and Interface Science. 2006;300:673-87.
[113] Zhan Z, Wang C, Fu W, Pan M. Visualization of water transport in a transparent PEMFC. International Journal of Hydrogen Energy. 2012;37:1094-105.
[114] Spernjak D, Prasad AK, Advani SG. Experimental investigation of liquid water formation and transport in a transparent single-serpentine PEM fuel cell. Journal of Power Sources. 2007;170:334-44.
[115] Dillet J, Lottin O, Maranzana G, Didierjean S, Conteau D, Bonnet C. Direct observation of the two-phase flow in the air channel of a proton exchange membrane fuel cell and of the effects of a clogging/unclogging sequence on the current density distribution. Journal of Power Sources. 2010;195:2795-9.
[116] Tüber K, Pócza D, Hebling C. Visualization of water buildup in the cathode of a transparent PEM fuel cell. Journal of Power Sources. 2003;124:403-14.
[117] Ma HP, Zhang HM, Hu J, Cai YH, Yi BL. Diagnostic tool to detect liquid water removal in the cathode channels of proton exchange membrane fuel cells. Journal of Power Sources. 2006;162:469-73.
[118] Su A, Weng F-B, Hsu C-Y, Chen Y-M. Studies on flooding in PEM fuel cell cathode channels. International Journal of Hydrogen Energy. 2006;31:1031-9.
[119] Liu X, Guo H, Ye F, Ma CF. Water flooding and pressure drop characteristics in flow channels of proton exchange membrane fuel cells. Electrochimica Acta. 2007;52:3607-14.
[120] Hussaini IS, Wang C-Y. Visualization and quantification of cathode channel flooding in PEM fuel cells. Journal of Power Sources. 2009;187:444-51.

[121] Nie J, Chen Y. Numerical modeling of three-dimensional two-phase gas–liquid flow in the flow field plate of a PEM electrolysis cell. International Journal of Hydrogen Energy. 2010;35:3183-97.
[122] Atiyeh HK, Karan K, Peppley B, Phoenix A, Halliop E, Pharoah J. Experimental investigation of the role of a microporous layer on the water transport and performance of a PEM fuel cell. Journal of Power Sources. 2007;170:111-21.
[123] Brett DJL, Aguiar P, Clague R, Marquis AJ, Schöttl S, Simpson R, et al. Application of infrared thermal imaging to the study of pellet solid oxide fuel cells. Journal of Power Sources. 2007;166:112-9.
[124] Hakenjos A, Hebling C. Spatially resolved measurement of PEM fuel cells. Journal of Power Sources. 2005;145:307-11.
[125] Matian M, Marquis AJ, Brandon NP. Application of thermal imaging to validate a heat transfer model for polymer electrolyte fuel cells. International Journal of Hydrogen Energy. 2010;35:12308-16.
[126] Gao F, Blunier B, Miraoui A, El-Moudni A. Cell layer level generalized dynamic modeling of a PEMFC stack using VHDL-AMS language. International Journal of Hydrogen Energy. 2009;34:5498-521.
[127] Wu J, Zi Yuan X, Wang H, Blanco M, Martin JJ, Zhang J. Diagnostic tools in PEM fuel cell research: Part II: Physical/chemical methods. International Journal of Hydrogen Energy. 2008;33:1747-57.
[128] Bird RB, E. SW, N. LE. Transport Phenoena. second edition ed. New York: John Wiley & Sons 2007.
[129] Marangio F, Santarelli M, Calì M. Theoretical model and experimental analysis of a high pressure PEM water electrolyser for hydrogen production. International Journal of Hydrogen Energy. 2009;34:1143-58.
[130] Tschinder T, Schaffer T, Fraser S, Hacker V. Electro-osmotic drag of methanol in proton exchange membranes. Journal of Applied Electrochemistry. 2007;37:711-6.
[131] Parthasarathy A, Davé B, Srinivasan S, Appleby AJ, Martin CR. The Platinum Microelectrode/Nafion Interface: An Electrochemical Impedance Spectroscopic Analysis of Oxygen Reduction Kinetics and Nafion Characteristics. Journal of The Electrochemical Society. 1992;139:1634-41.
[132] Whalley PB. Two-phase flow and heat transfer: Oxford University Press; 1996.
[133] Thome JR. Engineering data book III: Wolverine Tube, Inc.; 2004.
[134] Kashid MN, Renken A, Kiwi-Minsker L. Gas–liquid and liquid–liquid mass transfer in microstructured reactors. Chemical Engineering Science. 2011;66:3876-97.
[135] Taitel Y, Bornea D, Dukler AE. Modelling flow pattern transitions for steady upward gas-liquid flow in vertical tubes. AIChE Journal. 1980;26:345-54.
[136] Shao N, Gavriilidis A, Angeli P. Flow regimes for adiabatic gas–liquid flow in microchannels. Chemical Engineering Science. 2009;64:2749-61.
[137] Kreutzer MT, Kapteijn F, Moulijn JA, Heiszwolf JJ. Multiphase monolith reactors: Chemical reaction engineering of segmented flow in microchannels. Chemical Engineering Science. 2005;60:5895-916.

[138] Ito H, Maeda T, Nakano A, Hwang CM, Ishida M, Kato A, et al. Experimental study on porous current collectors of PEM electrolyzers. International Journal of Hydrogen Energy. 2012;37:7418-28.
[139] Sadatomi M, Sato Y, Saruwatari S. Two-phase flow in vertical noncircular channels. International Journal of Multiphase Flow. 1982;8:641-55.
[140] Bi QC, Zhao TS. Taylor bubbles in miniaturized circular and noncircular channels. International Journal of Multiphase Flow. 2001;27:561-70.
[141] Bhunia A, Pais SC, Kamotani Y, Kim I-H. Bubble formation in a coflow configuration in normal and reduced gravity. AIChE Journal. 1998;44:1499-509.
[142] Chen S-l, Lin C-t, Pan C, Chieng C-c, Tseng F-g. Growth and detachment of chemical reaction-generated micro-bubbles on micro-textured catalyst. Microfluid Nanofluid. 2009;7:807-18.
[143] Sarkar MSKA, Evans GM, Donne SW. Bubble size measurement in electroflotation. Minerals Engineering. 2010;23:1058-65.
[144] Zhang FY, Yang XG, Wang CY. Liquid Water Removal from a Polymer Electrolyte Fuel Cell. Journal of The Electrochemical Society. 2006;153:A225-A32.
[145] Multilayer bonding. Ayrshire2006.
[146] Hoppe EW, Seifert A, Aalseth CE, Bachelor PP, Day AR, Edwards DJ, et al. Cleaning and passivation of copper surfaces to remove surface radioactivity and prevent oxide formation. Nuclear Instruments and Methods in Physics Research Section A: Accelerators, Spectrometers, Detectors and Associated Equipment. 2007;579:486-9.
[147] Nimate nickel sulphamate. Birmingham: Balco; 2007.
[148] Orosene 999. Rhode Island: Technic Inc.
[149] Xie J, More KL, Zawodzinski TA, Smith WH. Porosimetry of MEAs Made by "Thin Film Decal" Method and Its Effect on Performance of PEFCs. Journal of The Electrochemical Society. 2004;151:A1841-A6.
[150] Dedigama I, Angeli P, Ayers K, Robinson JB, Shearing PR, Tsaoulidis D, et al. In situ diagnostic techniques for characterisation of polymer electrolyte membrane water electrolysers – Flow visualisation and electrochemical impedance spectroscopy. International Journal of Hydrogen Energy. 2014;39:4468-82.
[151] Ni M, Leung MKH, Leung DYC. Electrochemistry modelling of Proton Exchange Membrane (PEM) water electrolysis for hydrogen production. WHEC. Lyon France2006.
[152] Görgün H. Dynamic modelling of a proton exchange membrane (PEM) electrolyzer. International Journal of Hydrogen Energy. 2006;31:29-38.
[153] Lebbal ME, Lecœuche S. Identification and monitoring of a PEM electrolyser based on dynamical modelling. International Journal of Hydrogen Energy. 2009;34:5992-9.
[154] Biaku CY, Dale NV, Mann MD, Salehfar H, Peters AJ, Han T. A semiempirical study of the temperature dependence of the anode charge transfer coefficient of a 6 kW PEM electrolyzer. International Journal of Hydrogen Energy. 2008;33:4247-54.
[155] García-Valverde R, Espinosa N, Urbina A. Simple PEM water electrolyser model and experimental validation. International Journal of Hydrogen Energy. 2012;37:1927-38.

[156] Atlam O, Kolhe M. Equivalent electrical model for a proton exchange membrane (PEM) electrolyser. Energy Conversion and Management. 2011;52:2952-7.
[157] Medina P, Santarelli M. Analysis of water transport in a high pressure PEM electrolyzer. International Journal of Hydrogen Energy. 2010;35:5173-86.
[158] Berning T, Lu DM, Djilali N. Three-dimensional computational analysis of transport phenomena in a PEM fuel cell. Journal of Power Sources. 2002;106:284-94.
[159] Grigoriev S, Kalinnikov A, Millet P, Porembsky V, Fateev V. Mathematical modeling of high-pressure PEM water electrolysis. Journal of Applied Electrochemistry. 2010;40:921-32.
[160] Bernardi DM, Verbrugge MW. Mathematical model of a gas diffusion electrode bonded to a polymer electrolyte. AIChE Journal. 1991;37:1151-63.
[161] Marr C, Li X. An engineering model of proton exchange membrane fuel cell performance. ARI - An International Journal for Physical and Engineering Sciences. 1998;50:190-200.
[162] Springer TE, Zawodzinski TA, Gottesfeld S. Polymer electrolyte fuel cell model. Journal of Electrochemical Society. 1991;138:2334-42.
[163] Amphlett JC, Baumert RM, Mann RF, Peppley BA, Roberge PR, Harris TJ. Performance Modeling of the Ballard Mark IV Solid Polymer Electrolyte Fuel Cell: I . Mechanistic Model Development. Journal of The Electrochemical Society. 1995;142:1-8.
[164] Shimpalee S, Van Zee JW. Numerical studies on rib & channel dimension of flow-field on PEMFC performance. International Journal of Hydrogen Energy. 2007;32:842-56.
[165] Zawodzinski TA, Derouin C, Radzinski S, Sherman RJ, Smith VT, Springer TE, et al. Water Uptake by and Transport Through Nafion® 117 Membranes. Journal of The Electrochemical Society. 1993;140:1041-7.
[166] Li X, Qu S, Yu H, Hou M, Shao Z, Yi B. Membrane water-flow rate in electrolyzer cells with a solid polymer electrolyte (SPE). Journal of Power Sources. 2009;190:534-7.
[167] Onda K, Murakami T, Hikosaka T, Kobayashi M, Notu R, Ito K. Performance Analysis of Polymer-Electrolyte Water Electrolysis Cell at a Small-Unit Test Cell and Performance Prediction of Large Stacked Cell. Journal of The Electrochemical Society. 2002;149:A1069-A78.
[168] Ge S, Yi B, Ming P. Experimental Determination of Electro-Osmotic Drag Coefficient in Nafion Membrane for Fuel Cells. Journal of The Electrochemical Society. 2006;153:A1443-A50.
[169] LeRoy RL, Bowen CT, LeRoy DJ. The Thermodynamics of Aqueous Water Electrolysis. Journal of The Electrochemical Society. 1980;127:1954-62.
[170] Santarelli MG, Torchio MF, Cochis P. Parameters estimation of a PEM fuel cell polarization curve and analysis of their behavior with temperature. Journal of Power Sources. 2006;159:824-35.
[171] Santarelli MG, Torchio MF. Experimental analysis of the effects of the operating variables on the performance of a single PEMFC. Energy Conversion and Management. 2007;48:40-51.

[172] Song C, Tang Y, Zhang JL, Zhang J, Wang H, Shen J, et al. PEM fuel cell reaction kinetics in the temperature range of 23–120 °C. Electrochimica Acta. 2007;52:2552-61.
[173] Parthasarathy A, Srinivasan S, Appleby AJ, Martin CR. Temperature Dependence of the Electrode Kinetics of Oxygen Reduction at the Platinum/Nafion® Interface-A Microelectrode Investigation. Journal of The Electrochemical Society. 1992;139:2530-7.
[174] Beattie PD, Basura VI, Holdcroft S. Temperature and pressure dependence of O2 reduction at Pt|Nafion® 117 and Pt|BAM® 407 interfaces. Journal of Electroanalytical Chemistry. 1999;468:180-92.
[175] Damjanovic A, Dey A, Bockris JOM. Electrode Kinetics of Oxygen Evolution and Dissolution on Rh, Ir, and Pt-Rh Alloy Electrodes. Journal of The Electrochemical Society. 1966;113:739-46.
[176] Ito H, Maeda T, Nakano A, Takenaka H. Properties of Nafion membranes under PEM water electrolysis conditions. International Journal of Hydrogen Energy. 2011;36:10527-40.
[177] Radev I, Georgiev G, Sinigersky V, Slavcheva E. Proton conductivity measurements of PEM performed in EasyTest Cell. International Journal of Hydrogen Energy. 2008;33:4849-55.
[178] Powell RW, Tye RP. Thermal conductivities and electrical resistivities of the platinum metals. Platinum Metals Review. 1962;6:138-43.
[179] Milck JT. Electrical resistivity data and bibliography on titanium and titanium alloys. Springfield: Airforce Materials Laboratory; 1970.
[180] Goetz A, Holser A. The Electric Resistance and Anisotropy of Artificial Graphite Between 290° K. and 12° K. Transactions of The Electrochemical Society. 1942;82:391-6.
[181] del Real AJ, Arce A, Bordons C. Development and experimental validation of a PEM fuel cell dynamic model. Journal of Power Sources. 2007;173:310-24.
[182] Badwal SPS, Giddey S, Ciacchi FT. Hydrogen and oxygen generation with polymer electrolyte membrane (PEM)-based electrolytic technology. Ionics. 2006;12:7-14.
[183] Grigor'ev SA, Khaliullin MM, Kuleshov NV, Fateev VN. Electrolysis of Water in a System with a Solid Polymer Electrolyte at Elevated Pressure. Russian Journal of Electrochemistry. 2001;37:819-22.
[184] Selamet ÖF, Becerikli F, Mat MD, Kaplan Y. Development and testing of a highly efficient proton exchange membrane (PEM) electrolyzer stack. International Journal of Hydrogen Energy. 2011;36:11480-7.
[185] Siracusano S, Di Blasi A, Baglio V, Brunaccini G, Briguglio N, Stassi A, et al. Optimization of components and assembling in a PEM electrolyzer stack. International Journal of Hydrogen Energy. 2011;36:3333-9.
[186] Sigrist L, Dossenbach O, Ibl N. Mass transport in electrolytic cells with gas sparging. International Journal of Heat and Mass Transfer. 1979;22:1393-9.
[187] Cui ZF, Chang S, Fane AG. The use of gas bubbling to enhance membrane processes. Journal of Membrane Science. 2003;221:1-35.
[188] Hibiki T, Mishima K. Flow regime transition criteria for upward two-phase flow in vertical narrow rectangular channels. Nuclear Engineering and Design. 2001;203:117-31.

[189] Triplett KA, Ghiaasiaan SM, Abdel-Khalik SI, LeMouel A, McCord BN. Gas–liquid two-phase flow in microchannels: Part II: void fraction and pressure drop. International Journal of Multiphase Flow. 1999;25:395-410.
[190] Vollmer VM, Möllmann KP. Infrared Thermal Imaging. Fundamentals, Research and Applications. Germany: WILEY-VCH Verlag; 2011.
[191] Siracusano S, Baglio V, Di Blasi A, Briguglio N, Stassi A, Ornelas R, et al. Electrochemical characterization of single cell and short stack PEM electrolyzers based on a nanosized IrO2 anode electrocatalyst. International Journal of Hydrogen Energy. 2010;35:5558-68.
[192] Guo H, Wu F, Ye F, Zhao J, Wan S, Lü C, et al. Two-phase flow in anode flow field of a small direct methanol fuel cell in different gravities. Sci China Ser E-Technol Sci. 2009;52:1576-82.
[193] Bewer T, Beckmann T, Dohle H, Mergel J, Stolten D. Novel method for investigation of two-phase flow in liquid feed direct methanol fuel cells using an aqueous H2O2 solution. Journal of Power Sources. 2004;125:1-9.
[194] Mishima K, Hibiki T. Some characteristics of air-water two-phase flow in small diameter vertical tubes. International Journal of Multiphase Flow. 1996;22:703-12.
[195] Wang H, Dewald HD, Jepson WP. Mass-Transfer Enhancement in Large-Diameter Pipeline under Water/Gas Stationary Slug Flow. Journal of The Electrochemical Society. 2004;151:B114-B23.
[196] Zheng D, Che D, Liu Y. Experimental investigation on gas–liquid two-phase slug flow enhanced carbon dioxide corrosion in vertical upward pipeline. Corrosion Science. 2008;50:3005-20.
[197] Yan K, Che D. Hydrodynamic and mass transfer characteristics of slug flow in a vertical pipe with and without dispersed small bubbles. International Journal of Multiphase Flow. 2011;37:299-325.
[198] Dedigama Ishanka, Mason Thomas J, Millichamp Jason, Ayers Kathy, Shearing Paul R , Brett Dan. An Electrochemical Impedance Spectroscopy Study of a Polymer Electrolyte Membrane Water Electrolyser. International Journal of Hydrogen Energy. Submitted.
[199] Wilkinson P. Understanding gold plating. Gold Bull. 1986;19:75-81.

9. Appendix

The Gold Deposition Process

The cathode of the electroplating bath attracts positive ions to a region near its surface, which is known as the Helmholtz double layer. The negative ions ($Au(CN)_2^-$), that approach this layer become polarized in the electric field of the cathode thus diffuses into the layer breaking up into ligand ions and the metal in the form of a positively charged cation (Equation (106)) which then deposits as the metal atom on the cathode. This process is more clearly expressed in Figure 65 [199].

$$Au(CN)_2^- \Leftrightarrow Au^+ + 2CN^- \quad (106)$$

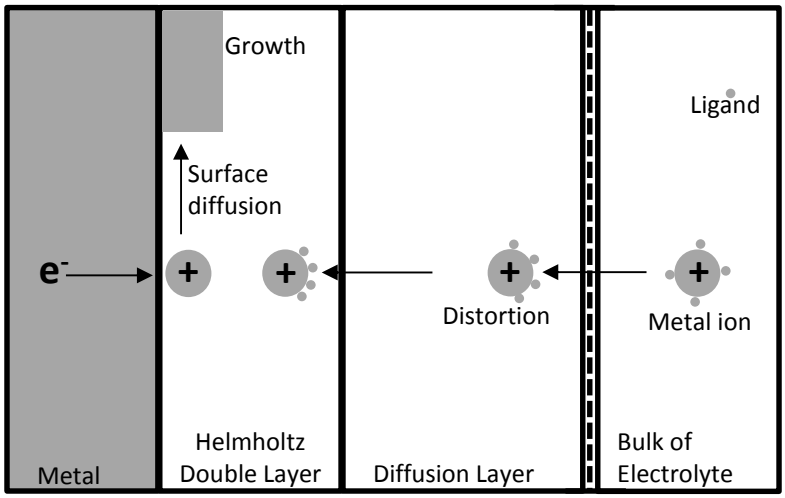

Figure 65: A schematic of the gold deposition process [199].

Software Control

Rig Control

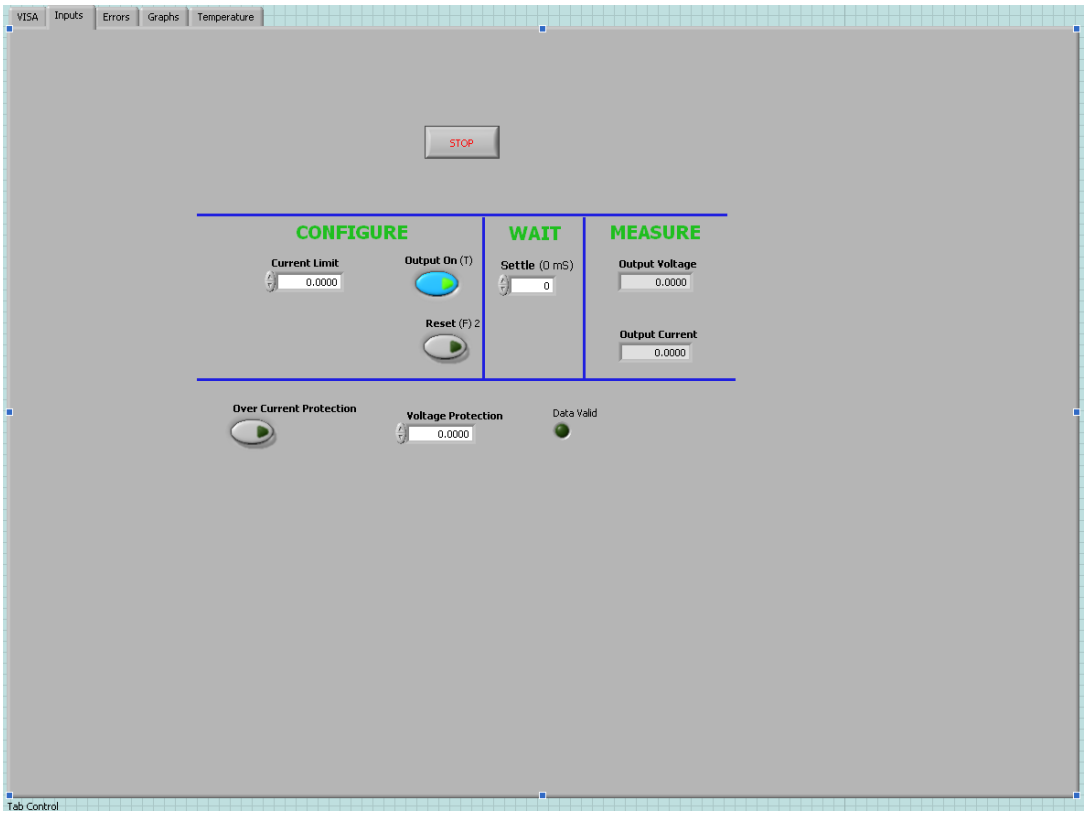

Figure 66: Front panel of LabVIEW software for rig set up.

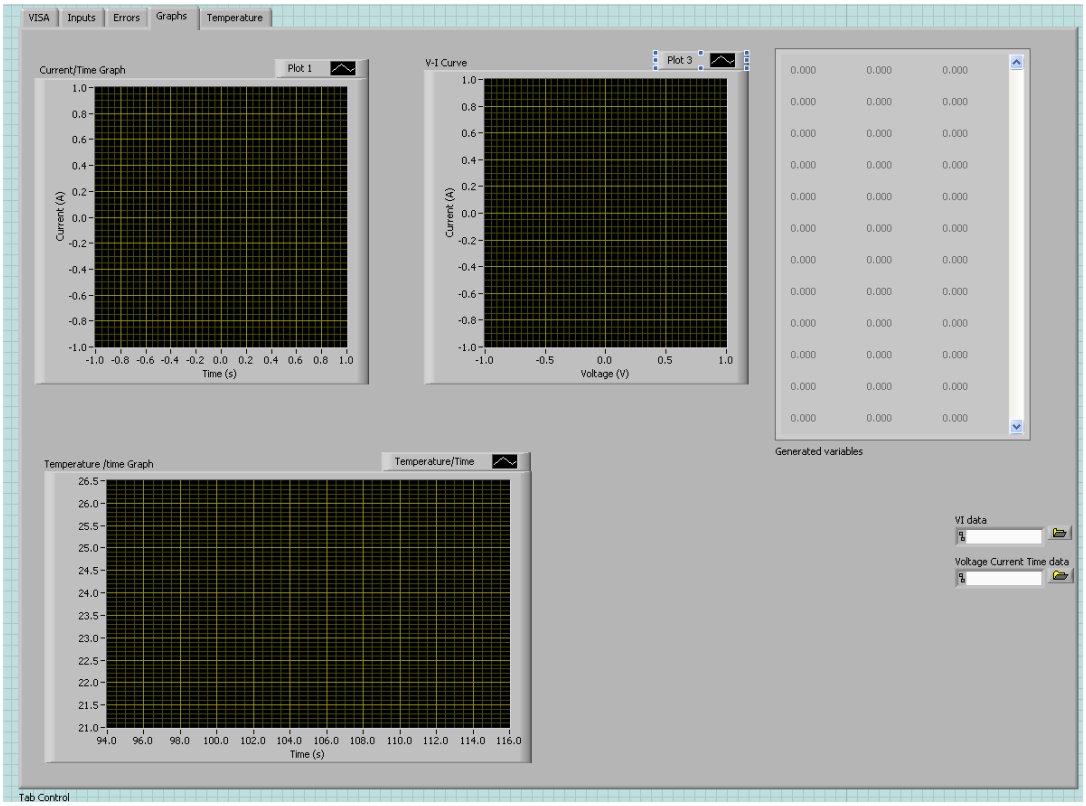

Figure 67: Output Panel LabVIEW software for rig set up.

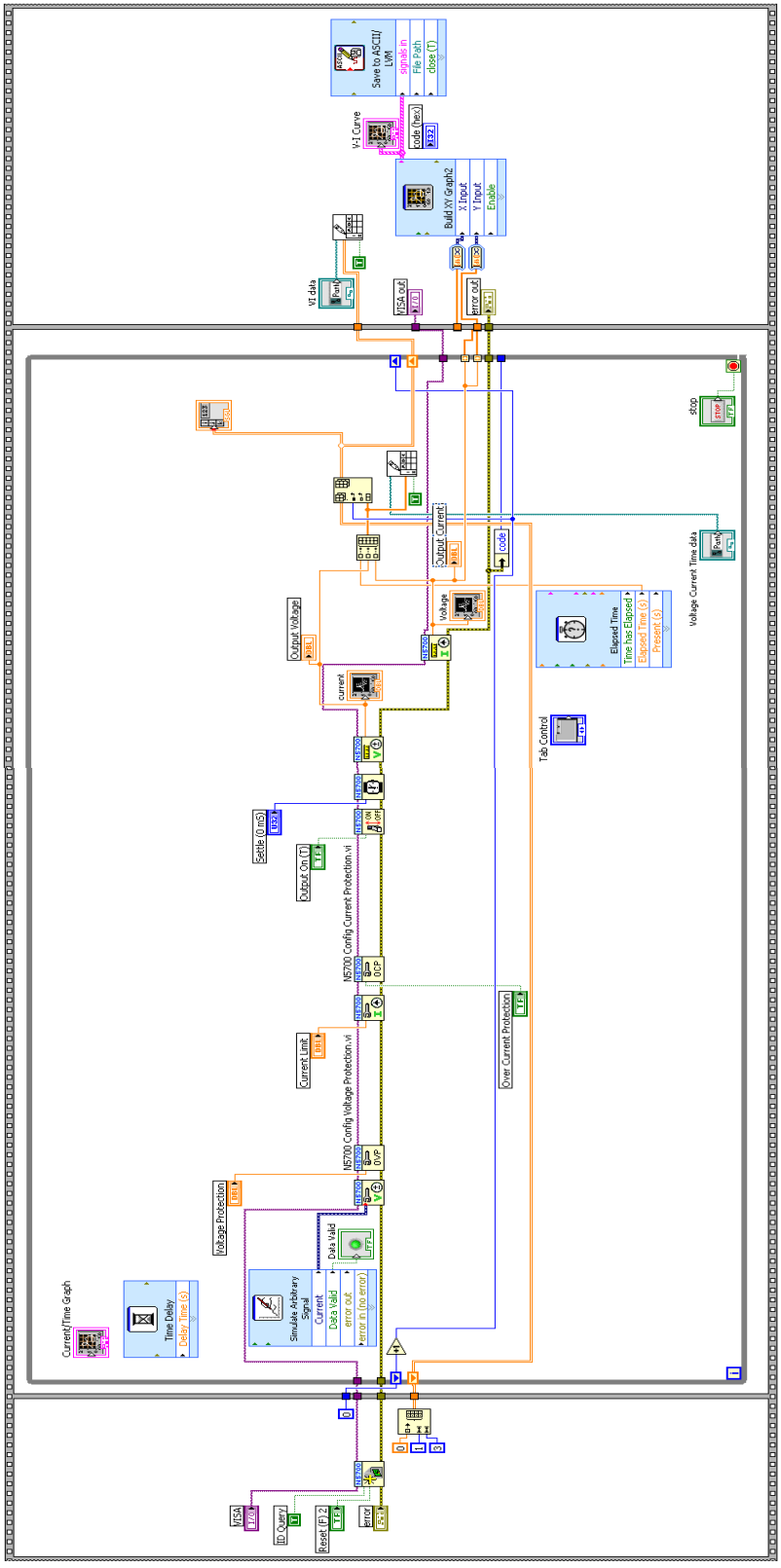

Figure 68: Block diagram of LabVIEW VIs for rig set up.

DAQ control

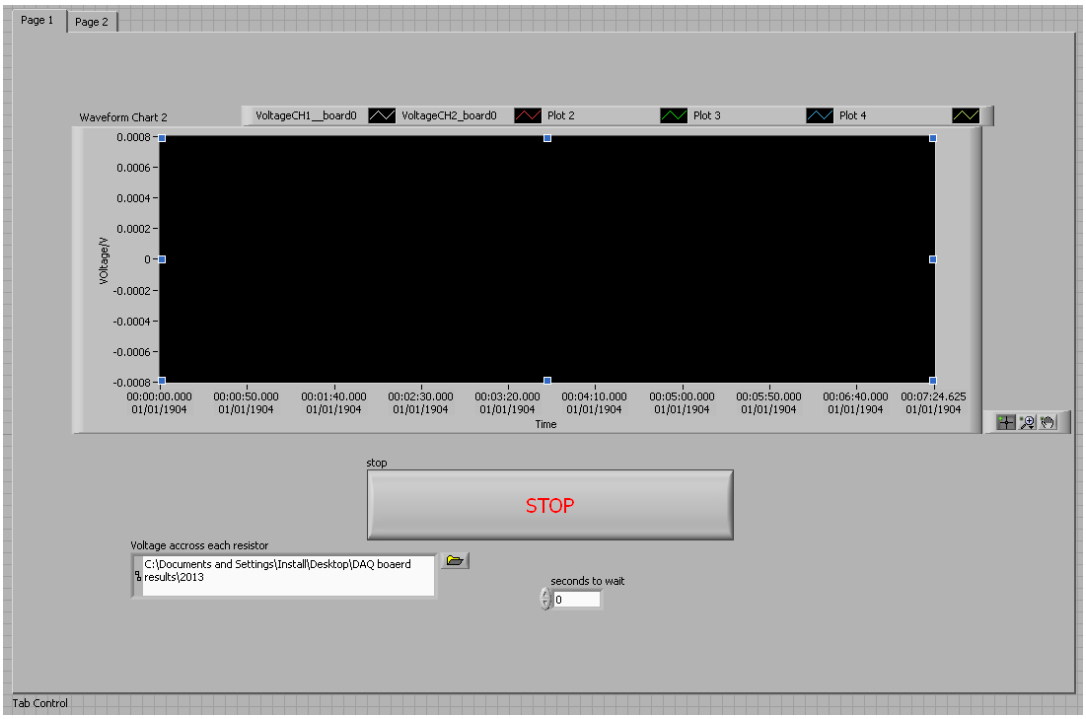

Figure 69: Output panel of LabVIEW software for DAQ card

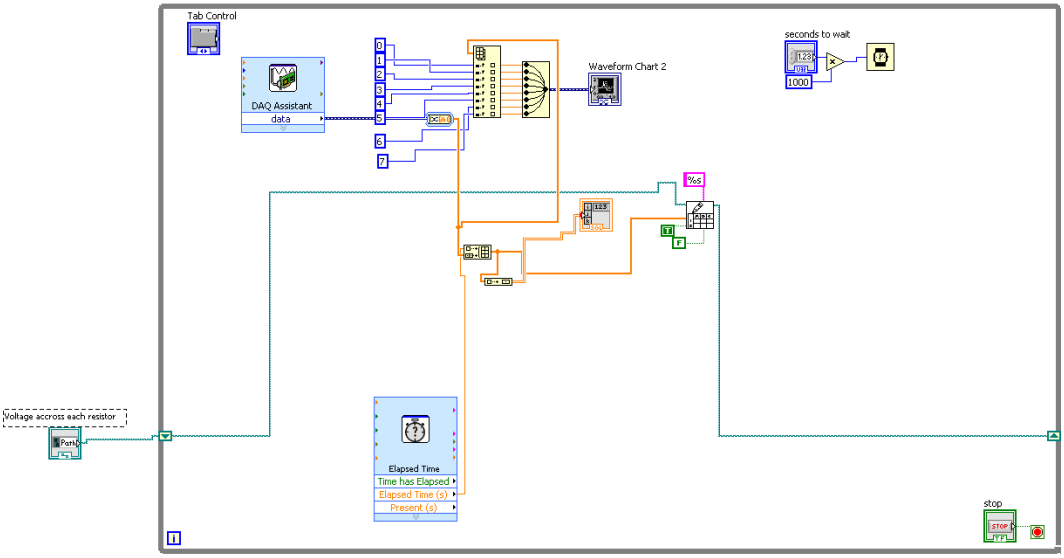

Figure 70: Block diagram of LabVIEW VIs for DAQ card.